PROPERTIES OF THE NANOPORE MEMBRANE AS A SOLID SUPPORT FOR ION CHANNEL RECORDINGS AND APPLICATION TOWARDS IDENTIFYING SINGLE NUCLEOTIDE MODIFICATIONS

by

Anna E. P. Schibel

A dissertation submitted to the faculty of
The University of Utah
in partial fulfillment of the requirements for the degree of

Doctor of Philosophy

Department of Chemistry

University of Utah

May 2011

The University of Utah Graduate School

STATEMENT OF DISSERTATION APPROVAL

The dissertation of **Anna E. P. Schibel**

has been approved by the following supervisory committee members:

Henry S. White	, Chair	**03/01/2011** Date Approved
Edward M. Eyring	, Member	**03/01/2011** Date Approved
David P. Goldenberg	, Member	**03/01/2011** Date Approved
Joel M. Harris	, Member	**03/01/2011** Date Approved
Jennifer S. Shumaker-Parry	, Member	**03/01/2011** Date Approved

and by **Henry S. White**, Chair of the Department of **Chemistry**

and by Charles A. Wight, Dean of The Graduate School.

ABSTRACT

The nanopore membrane is a single conical-shaped pore in a solid glass or fused quartz membrane at the end of a capillary; it can be used to support a planar lipid bilayer for ion channel recordings with a reconstituted biological nanopore. The work presented here explores the nature of the nanopore membrane and its influence on the suspended bilayer. The nanopore membrane is then used for ion channel recordings with the protein ion channel α-hemolysin (α-HL) to detect single oxidative damage sites within a DNA sequence.

Chemical modifications to the surface of the glass nanopore membrane with hydrophobic silanes (trimethylchlorosilane, n-butyldimethylchlorosilane, and n-octadecyldimethylchlorosilane) are explored to understand their influence on the pore wettability and the bilayer structure (seal resistance, voltage stability, and lifetime). Further, fused quartz was used to fabricate fused quartz nanopore membranes (QNMs) and these were compared with the traditional soda lime glass membranes as bilayer supports. The leakage current across the membrane was compared for fused quartz and soda lime glass capillaries.

The structure of the suspended bilayer is investigated as a function of applied pressure across the orifice of a QNM using fluorescence microscopy. Ion channel reconstitution within lipid bilayers suspended across nanopore membranes is a pressure-dependent process; a positive pressure must be

applied to the inside of the nanopore relative to the exterior for protein channel insertion to occur.

Lastly, the nanopore membrane was used to perform ion channel recordings to detect the presence of a single oxidative damage site within a DNA sequence. The kinetics of the DNA duplex unzipping process within the α-HL nanopore were monitored to determine the presence of a single DNA lesion, 8-oxo-7,8-dihydroguanine (OG). The presence of OG influences the duplex stability which is reflected in the unzipping event duration. Additionally, the detection of a single oxidative damage site is examined using DNA immobilization experiments to determine the presence of the damage site based on the ion channel current. A single OG site within a DNA strand is adducted with a larger molecule and held within the α-HL protein ion channel. The resultant current blockage level and noise level are shown to be unique to the adducted molecule.

To my mother and father

TABLE OF CONTENTS

LIST OF ABBREVIATIONS

A: adenine

α-HL: α-hemolysin

BMCS: n-butyldimethylchlorosilane

Btn: biotin

Bz: benzylamine

C-18: n-octadecyldimethyl-chlorosilane

C: cytosine

CMCS: 3-cyanopropyl-dimethylchlorosilane

DPhPC: 1,2-diphytanoyl-*sn*-glycero-3-phosphocholine

G:guanine

Gh: guanidinohydantoin

GlcN: D-(+)-glucosamine

GNM: glass nanopore membrane

GPRP: Gly-Pro-Arg-Pro amide

I: inosine

Lys: Ac-Lys-OMe

OG: 8-oxo-7,8-dihydroguanine

QNM: fused quartz nanopore membrane

s_7βCD: heptakis (2,3-di-O-acetyl-6-O-sulfo)-β-cyclodextrin heptasodium salt

ssDNA: single-stranded DNA

Sp:spiroiminodihydantoin

Spd: spermidine

Spm: spermine

Strep: streptavidin

T:thymine

$TBAPF_6$: tetra-*n*-butylammonium hexafluorophosphate

T_m: melting temperature

TMCS: trimethylchlorosilane

ACKNOWLEDGEMENTS

First, I would like to thankfully acknowledge my advisor Prof. Henry S. White, who has been instrumental in guiding me through my graduate research. His example has helped me not only to develop a thorough experimental methodology, but also to approach and analyze information in a critical manner. I appreciate his active interest and enthusiasm in science; I attribute my success in future scientific endeavors to his mentorship.

I would like to thank Dr. Eric Ervin, Dr. Ryan White, and Dr. Ryuji Kawano for introducing me to the laboratory and teaching me how to fabricate glass nanopore membranes, perform ion channel recordings, as well as providing perceptive and discerning discussions. I would like to thank Prof. Joel Harris and Dr. Emily Heider for sharing their fluorescence microscopy expertise and scientific contribution in Chapter 4. I also thank Prof. Cynthia Burrows, Dr. Aaron Fleming and Na An for making Chapter 5 and Chapter 6 possible with their knowledge, efforts, discussions, and ideas concerning DNA and DNA damage detection.

I would like to thank my family for always being supportive; my mother and father for their unconditional encouragement and optimism. Finally, I would like to thank my husband Jared for his love, support, understanding, and technical expertise.

PUBLICATION LIST

CHAPTER 2

Anna E. P. Schibel, Jin Liu, and Henry S. White “Chemical Modification of the Glass Nanopore Membrane Surface.” in preparation.

CHAPTER 3

Anna E. P. Schibel, Thomas Edwards, Ryuji Kawano, Wenjie Lan, and Henry S. White “Quartz Nanopore Membranes for Suspended Bilayer Ion Channel Recordings.” *Anal. Chem.* **2010**, *82*, 7259-7266.

CHAPTER 4

Anna E. P. Schibel, Emily C. Heider, Joel M. Harris, Henry S. White “Fluorescence Microscopy of the Pressure-Dependent Structure of Lipid Bilayers Suspended Across Conical Nanopores.” in preparation.

CHAPTER 5

Anna E. P. Schibel, Aaron M. Fleming, Jin Liu, Na An, Chas Blakemore, Qian Jin, Henry S. White and Cynthia J. Burrows “Sequence-specific Single-molecule Analysis of 8-Oxo-7,8-dihydroguanine Lesions in DNA based on Unzipping Kinetics of Complementary Probes in Ion Channel Recordings.” in preparation.

CHAPTER 6

Anna E. P. Schibel, Na An, Qian Jin, Aaron M. Fleming, Cynthia J. Burrows, and Henry S. White “Nanopore Detection of 8-Oxo-7,8-dihydro-2’-deoxyguanosine in Immobilized Single-stranded DNA via Adduct Formation to the DNA Damage Site” *J. Am. Chem. Soc*. **2010**, *132*, 17992-17995.

CHAPTER 1

INTRODUCTION

Ion channel recordings have gained a significant amount of attention in recent years as an analytical tool for the detection and characterization of particles, metal ions, and polymers, with strong focus applied toward the detection and sequencing of DNA.[1-16] However, much of the effort on using ion channel recordings for DNA sequence analysis has been limited by the stability of the lipid bilayer/ion channel system and the speed at which DNA translocation occurs through an ion channel or solid state pore. Often these measurements are performed with Delrin® cups or Teflon® membranes as the solid support for the planar bilayer, possessing orifices with radii on the order of tens to hundreds of microns. The large orifice size makes it difficult to maintain the bilayer over extended periods of time due to its susceptibility to damage by applied voltage, pressure changes, and mechanical vibrations. The glass nanopore membrane (GNM) is an alternative to these solid supports; it is composed of a glass membrane at the end of a capillary containing a single conical shaped orifice across which an artificial lipid bilayer can be suspended for protein channel reconstitution. The smaller orifice dimensions (radii of 10-1000 nm) lend an

inherent stability to the bilayer, improving the lifetime (up to weeks), and minimizing the system capacitance through the reduction in bilayer area.[17-19]

The work described herein is focused on two aspects of the nanopore membrane for ion channel recordings. First, the surface and material properties of glass and fused quartz nanopore membranes and the suspended lipid bilayer are investigated with respect to optimizing this system for ion channel recordings. Second, two strategies are described for using the GNM with α-hemolysin (α-HL) ion channel proteins to detect the presence of single oxidative damage sites within a DNA sequence.

Analytical ion channel recording experiments are performed by forming an artificial planar bilayer over the orifice of a hydrophobic solid support by depositing lipid solution (lipid molecules dispersed in an organic solvent) across the orifice and allowing the solution to thin to a bilayer.[20-27] Once a bilayer is formed, a biological protein nanopore may be reconstituted or inserted into the bilayer, creating a passage through which ions and molecules may traverse. When a voltage is applied across the ion channel, the fluxes of electrolyte ions are controlled by the occupancy of the pore, which can be determined by monitoring the current to observe molecule capture or translocation. As molecules enter the pore, the current flow decreases, and based on the geometry and character of the molecule, a unique current signature is produced. The selectivity of ion channels to different molecules and the ability to detect single molecules has led to recent widespread interest in ion channels as chemical sensors.[7-9]

Within this principle lies the potential to perform DNA sequencing via ion channel recording measurements. As a DNA strand translocates through a protein channel, each base (adenine (A), thymine (T), cytosine (C), and guanine (G)) will produce a characteristic current signal. Much of the effort invested towards DNA sequencing and base identification has yielded limited progress as the current differences between bases are not readily resolvable during translocation. However, in addition to the four native bases, a biological sample will possess biomarkers and damage sites, and any sequencing efforts will need to be able to recognize these modifications separately from A, T, C, and G. Aside from sequencing efforts, the ability to detect a damage site within a DNA sequence would have significant implications from a diagnostic and therapeutic standpoint. The research presented in this thesis has resulted in two new strategies for identifying the oxidative damage site 8-oxo-7,8-dihydroguanine (OG) in DNA.

While much molecular structural and analytical information can be obtained from the resultant ion channel recording current signal, there are also many inherent limitations to the technique. These limitations include the fragile nature of the artificial bilayer and system capacitance. These issues are addressed in Chapters 2, 3, and 4. Chapter 2 examines the influence of the surface modification on the wettability of the GNM orifice, the bilayer resistance and stability, as well as the bilayer lifetime. Chapter 3 addresses the use of fused quartz for the solid support material and compares the performance of quartz and traditional soda lime glass nanopores. Chapter 4 examines the

structure of the suspended lipid bilayer as a function of pressure via fluorescence microscopy.

Chapter 5 discusses the ability to locate a single oxidative damage site by monitoring the kinetics of a DNA duplex unzipping to translocate through the α-HL channel. Unzipping occurs because the diameter of the duplex is larger than the smallest region of the α-HL channel. The rate of unzipping depends on the stability of the duplex,[28-31] and the presence of a single oxidative damage site will change the overall stability in a unique manner based on the identity of the base pair formed, e.g., G:C vs OG:C or G:A vs. OG:A. Specifically, a short probe sequence is designed to form a duplex with a region in a 65mer DNA sequence containing either a G or an OG, and the unzipping time is indicative of whether a G or OG is present.

Chapter 6 explores the possibility of differentiating the current blockage signal generated by a DNA strand that has been immobilized within the α-HL channel to identify a DNA damage site relative to the current signal from the native bases A, T, C, and G. When the residence time of the DNA molecule is increased within the α-HL channel, the current resolution is increased, making it possible to distinguish between bases and modified bases.[32-38] Because A, T, C, G, and OG are of similar size, the differences in current blockage level will be small; the influence of generating a larger molecular adduct to the damage site is explored as a means to amplifying the difference in the current blockage level of OG relative to the native bases.

1.1 References

(1) Terstappen, G.C. *Drug Discovery Today: Technologies* **2005**, *2,* 133-140.

(2) Dabraoski, M.A.; Dekermendjian, K.; Lund, P.-E.; Krupp, J.J.; Sinclair, J.; Larsson, O. *CNS & Neurological Disorders-Drug Targets* **2008**, *7*, 122-128.

(3) Haddock, P. *American Pharmaceutical Review* **2006**, *9*, 119-122.

(4) Landry, Y.; Gies, J.-P. *Fundamental & Clinical Pharmacology* **2008**, *22*, 1-18.

(5) Jean-Yves, Le G.; Olivier, S.; Pierre, B.; Ahmed, A.; Christophe, V. *Recent Patents on Anti-Cancer Drug Discovery* **2007**, *2*, 189-202.

(6) Shim, J.W.; Gu, L.Q. *Anal. Chem.* **2007**, *79*, 2207-2213.

(7) Gu, L.-Q.; Braha, O.; Conlan, S.; Cheley, S.; Baley, H. *Nature* **1999**, *398*, 686-690.

(8) Bayley, H.; Braha, O.; Gu, L.-Q. *Adv. Mater.* **2000**, *12*, 139-142.

(9) Braha, O.; Gu, L.-Q.; Zhou, L.; Xiaofeng, L.; Cheley, S.; Bayley, H. *Nat. Biotechnol.* **2000**, *18*, 1005-1007.

(10) Deamer, D.; Branton, D. *Acc. Chem. Res*. **2002**, *35*, 817-825.

(11) Vercoutere, W. A.; Winters-Hilt, S.; DeGuzman, V. S.; Deamer, D.; Ridino, S. E.; Rodgers, J. T.; Olsen, H. E.; Marziali, A.; Akeson, M. *Nucleic Acids Res.* **2003**, *31*, 1311-1318.

(12) DeGuzman, V. S.; Lee, C. C.; Deamer, D. W.; Vercoutere, A. *Nucleic Acids Res.* **2006**, *34*, 6425-6437.

(13) Kasianowicz, J. J.; Brandin, E.; Branton, D.; Deamer, D. W. *Proc. Natl. Acad. Sci.* **1996**, *93*, 13770-13773.

(14) Akeson, M.; Branton, D.; Kasianowicz, J. J.; Brandin, E.; Deamer, D. W. *Biophys. J.* **1999**, *77*, 3227-3233.

(15) Meller, A.; Nivon, L.; Brandin, E.; Golovchenko, J.; Branton, D. *Proc. Natl. Acad. Sci.* **2000**, *97*, 1079-1084.

(16) Schibel, A. E. P.; An, N.; Jin, Q.; Fleming, A. M.; Burrows, C. J.; White, H. S. *J. Am. Chem. Soc.* **2010**, *132*, 17992-17995.

(17) Zhang, B.; Zhang, Y.; White, H.S. *Anal. Chem.* **2004**, 76, 6229-6238.

(18) Zhang, B.; Galusha, J.; Shiozawa, P.G.; Gangli, W.; Bergren, A.J.; Jones, R.M.; White, R.J.; Ervin, E.N.; Cauley, C.C.; White, H.S. *Anal. Chem.* **2007**, 79, 4778-4787.

(19) White, R.J.; Ervin, E.N.; Yang, T.; Chen, X.; Daniel, S.; Cremer, P.S.; White, H.S. *J. Am. Chem. Soc.* **2007**, 129, 11766-11775.

(20) Alverez, O. How to Set Up a Bilayer System. In *Ion Channel Reconstitution*; Miller, C. Ed.; Penum Publishing Co.: New York, 1986; pp 115-130.

(21) Mueller, P.; Rudin, D.O.; Tien, H.T.; Wescott, W.C. *Circulation* **1962**, 26, 1167-1171.

(22) Mueller, P.; Rudin, D.O.; Tien, H.T.; Wescott, W.C. *Nature* **1962**, 194, 979-980.

(23) Mueller, P.; Rudin, D. O.; Tien, H. T.; Wescott, W. C. *J. Phys. Chem.* **1963**, *67*, 534-535.

(24) Tien, H. T.; Diana, A. L. *Chem. Phys. Lipids* **1968**, *2*, 55-101.

(25) White, S. H. *Biophys. J.* **1970**, 10, 1127-1148.

(26) White, S. H. *Biophys. J.* **1972**, *12*, 432-445.

(27) White, S. H. The Physical Nature of Planar Bilayer Membranes. In *Ion Channel Reconstitution*; Miller, C. Ed.; Penum Publishing Co.: New York, 1986, pp 3-35.

(28) Mathé, J.; Visram, H.; Viasnoff, V.; Rabin, Y.; Meller, A. Biophys. J. 2004, 87, 3205-3212.

(29) McNally, B.; Wanunu, M.; Meller, A. Nano Lett. 2008, 8, 3418-3422.

(30) Sutherland, T. C.; Dinsmore, M. J.; Kraatz, H.-B.; Lee, J. S. Biochem. Cell Biol. 2004, 82, 407-412.

(31) Howorka, S.; Cheley, S.; Bayley, H. *Nat. Biotechnol.* **2001**, *19*, 636-639.

(32) Henrickson, S. E.; Misakian, M.; Robertson, B.; Kasianowicz, J. J. *Phys. Rev. Lett.* **2000**, *85*, 3057-3060.

(33) Nakane, J.; Wiggin, M.; Marziali, A. *Biophys. J.* **2004**, *87*, 615-621.

(34) Purnell, R. F.; Mehta, K. K.; Schmidt, J. J. *Nano Lett.* **2008**, *8*, 3029-3034.

(35) Stoddart, D.; Heron, A. J.; Mikhailova, E.; Maglia, G.; Bayley, H. *Proc. Natl. Acad. Sci.* **2009**, *106*, 7702-7707.

(36) Purnell, R. F.; Schmidt, J. J. *ACS Nano* **2009**, *9*, 2533-2538.

(37) Stoddart, D.; Maglia, G.; Mikhailova, E.; Heron, A. J.; Bayley, H. *Angew. Chem. Int. Ed.* **2009**, *48*, 1-5.

(38) Wallace, E. V. B.; Stoddart, D.; Heron, A. J.; Mikhailova, E.; Maglia, G.; Donohoe, T. J.; Bayley, H. *Chem. Commun.* **2010**, *46*, 8195-8197.

CHAPTER 2

CHEMICAL MODIFICATION OF THE GLASS NANOPORE MEMBRANE SURFACE

2.1 Introduction

Ion channel recordings have a variety of applications for pharmaceutical development, medical diagnosis, analyte detection and characterization, and recently DNA sequencing and single-base damage detection.[1-16] As a result of these widespread applications, new devices and system adaptations are being explored to improve the quality, reproducibility, and robustness of the measurement. The glass nanopore membrane (GNM) is a sealed glass capillary with a conically shaped pore embedded within the glass membrane, schematically depicted in Figure 2.1. The GNM was introduced as a bilayer support device as the orifice could be fabricated with dimensions as small as 10 nm.[17,18] This ability to fabricate small orifices, relative to traditional bilayer supports (r >50 μm), was found to be well suited for ion channel recordings as the small orifice improved the stability of the bilayer, improved bilayer lifetimes, and minimized the bilayer capacitance with reduced bilayer area (~1 μm^2 for r = 500 nm).[16-24]

Figure 2.1. (A) Schematic of the nanodisk electrode, (B) glass nanopore membrane, and (C) suspended bilayer structure.

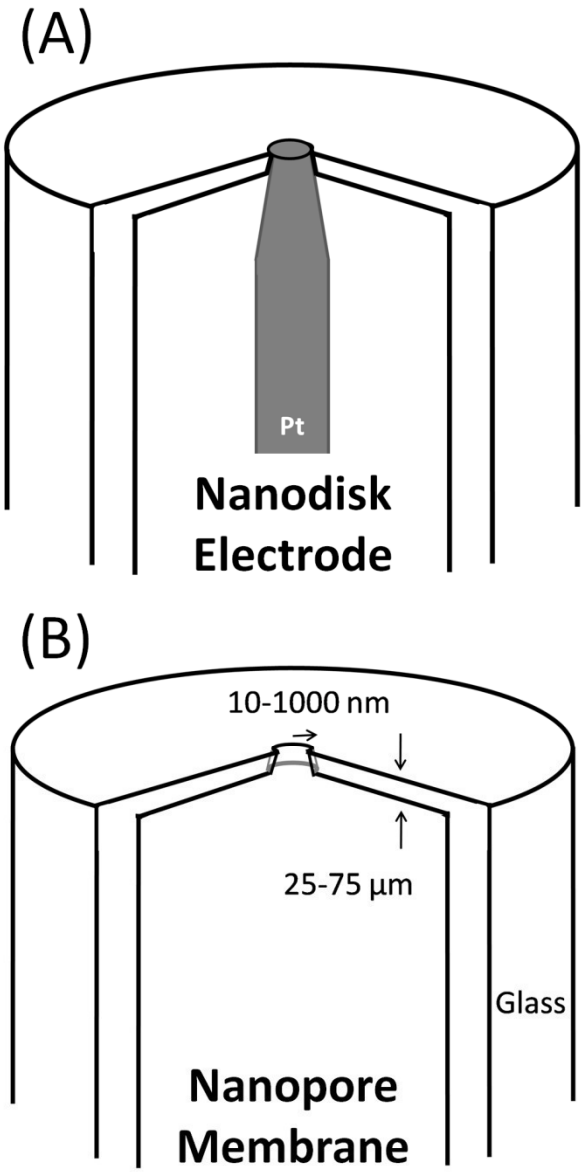
(A)
Pt
Nanodisk
Electrode
(B)
10-1000 nm
25-75 µm
Glass
Nanopore
Membrane
(C)

The GNM is chemically modified with 3-cyanopropyldimethylchlorosilane (CMCS) to generate a surface with sufficient hydrophobicity to support a suspended bilayer, while maintaining the wettability towards aqueous solutions. The hydrophobic tails of the lipid molecules orient toward the silanized glass substrate forming a monolayer on the glass surface and zip together over the orifice to form a bilayer (Figure 2.1C). With this system the bilayer is contained over the pore and limits the shunting current between the bilayer and support;[19,25-27] Figure 2.1C displays a schematic of the bilayer structure for a GNM with a CMCS surface modification.

This work examines how the properties of the bilayer depend on the hydrophobicity of the silane used for surface modification. Specifically, trimethylchlorosilane (TMCS), n-butyldimethylchlorosilane (BMCS), and n-octadecyldimethylchlorosilane (C-18) were used to modify the GNM surface prior to bilayer formation. The different surface modifications were first characterized via contact angle measurements, demonstrating that these silanes form nearly complete monolayers on glass within 1-2 hrs. The smallest GNM wetting radius was determined for CMCS and BMCS, using GNMs of known orifice radius dimensions. While the traditional CMCS modification did not inhibit pore wetting for the smallest orifices ($r < 10$ nm), the more hydrophobic BMCS did not allow wetting of pores with r less than ~100 nm. The reaction kinetics for surface silanization of the conically shaped GNM pore were determined indirectly through bilayer resistance measurements, and found to be similar to those for the planar glass slides; bilayer resistance did not change after 1-2 hrs of silanization, with

the hydrophobic silanes resulting in slightly higher resistive bilayers. Finally, measurements were performed to determine the bilayer voltage stability and bilayer lifetimes among CMCS, TMCS, BMCS, and C-18 modified GNMs. Although no significant differences in voltage stability and lifetime exist between the CMCS and the hydrophobic silane modifications, the BMCS functionalization resulted in bilayers with significantly greater stability against pressure fluctuations. Increased bilayer resistance also indicates an improved bilayer-substrate seal is achieved using more hydrophobic surface modifications.

2.2 Experimental Section

2.2.1 Chemicals and Materials

All aqueous solutions were made with ultrapure water, having a resistivity of 18 MΩ·cm, from a Barnstead E-pure water purifier. The following were used as received: KCl (Mallinckrodt), K_2HPO_4 (Mallinckrodt), KH_2PO_4 (Mallinckrodt), EDTA (Mallinckrodt), trizma base (Sigma-Aldrich), decane (Fisher Scientific), and toluene (Fisher Scientific). A buffered electrolyte solution of 1.0 M KCl, 30 mM Tris, and 10 mM EDTA was prepared and adjusted to pH 8, and used for all electrical measurements. The phospholipid 1,2-diphytanoyl-*sn*-glycero-3-phosphocholine (DPhPC) was obtained dispersed in chloroform from Avanti Polar Lipids, and was stored at -20 °C. 3-cyanopropyldimethylchlorosilane ($Cl(CH_3)_2Si(CH_2)_3CN$), trimethylchlorosilane ($ClSi(CH_3)$), n-butyldimethyl-chlorosilane ($Cl(CH_3)_2Si(CH_2)_3CH_3$), and n-octadecyldimethylchlorosilane ($Cl(CH_3)_2Si(CH_3)_{17}CH_3$) were purchased from Gelest, Inc. and used as received.

Fisher Scientific HPLC grade acetonitrile was stored with a 3Å molecular sieve. Ferrocene (Alfa Aesar) and tetra-*n*-butylammonium hexafluorophosphate ($TBAPF_6$, Sigma-Aldrich) were used as received to prepare a 5 mM ferrocene and 0.2 M $TBAPF_6$ acetonitrile solution for nanodisk electrode size characterization. Soda lime glass slides were obtained from Corning and cleaned in 0.1M HNO_3 (EMD Chemicals Inc.) prior to use. The protein ion channel α-hemolysin (α-HL) was purchased from Sigma-Aldrich as a monomer, excreted by *Staphylococcus aureus*, in the form of a lyophilized powder. When received, the α-HL was dissolved in ultrapure water at a concentration of 0.6 mg protein per mL and stored at -80 ˚C (when not in use). When in use, α-HL was diluted to the desired concentration using the buffered electrolyte solution and stored at 4 °C. Heptakis (2,3-di-O-acetyl-6-O-sulfo)-β-cyclodextrin heptasodium salt (s_7βCD) was purchased from Sigma-Aldrich and used at a concentration of 50 μM in the buffered electrolyte solution. Ag/AgCl electrodes were prepared by soaking clean silver wire (0.25 mm and 0.5 mm, Alfa Aesar) in Chlorox bleach for approximately 15 min and rinsing thoroughly with ultrapure water.

2.2.2 Glass Nanopore Membrane Fabrication

The fabrication of the GNM has been previously detailed,[17,18] and is briefly described here. A Pt wire (25 µm diameter) was electrochemically sharpened and sealed into the glass membrane of a sealed soda lime glass capillary, 25-75 µm deep, with an H_2 flame. The excess glass was removed with polishing until the Pt disk was exposed (Figure 2.1A). The exposure of the Pt disk was

monitored with an in-house feedback circuit. After exposure, the Pt was electrochemically etched back from the pore opening and the Pt wire was manually pulled from the glass membrane, resulting in a glass nanopore membrane (GNM). The radius of the nanodisk electrode and radius of the GNM pore were characterized by electrochemical and conductance measurements with a resulting error of ~10%;[19,25] this size characterization process is described in more detail below.

After fabrication, the GNM was chemically modified to increase the hydrophobicity of the glass surface.[19,25] The GNM was soaked in 0.1 M HNO_3 for approximately 10 min, after which it was rinsed thoroughly with ultrapure water, ethanol, and acetonitrile. A 2% (V:V) silane in acetonitrile solution was used for surface modifications employing CMCS, TMCS, and BMCS. For the C-18 silane, a 0.122 M solution of C-18 in toluene was used. Additionally, GNMs modified with CMCS were also modified in a 2% (V:V) solution using both toluene and a 1:1 acetonitrile/toluene mixed solvent. Silane solutions were used to initially rinse the GNM. The GNM was then filled with the same silane solution, and left to soak for periods of up to 3 days. All silanization reactions were performed at room temperature. After silanization, the GNM was rinsed with acetonitrile, ethanol, and ultrapure water. Each GNM was stored in ethanol, and rinsed before use with ultrapure water.

2.2.3 Electrical Measurements

Electronic measurements were recorded using a PC interfaced with a Dagan Corporation CHEM-CLMAP Voltammeter/Amperometer Voltage Clamp Amplifier and a Pine Instrument Company RDE4 Analog Bipotentiostat. A LabVIEW 8.2 (National Instruments) program, written in house, was used to record current-voltage (*i*-*V*) and current-time (*i*-*t*) traces. One Ag/AgCl (0.25 mm diameter) electrode was placed inside the GNM via a Dagan Corporation pipette holder and a second Ag/AgCl electrode (0.5 mm diameter) was placed outside of the GNM in the external cell solution; a voltage was applied between the electrodes from the inside of the GNM with respect to the outside solution.

The DPhPC lipid was dried with a nitrogen stream and re-dispersed in 1 mL decane to produce a 10mg DPhPC per mL decane lipid solution. A second lipid solution was formed by dispersing the dried lipid in 2 mL of solvent (1:1 decane/hexane) resulting in a 5mg DPhPC per mL lipid solution. Lipid solutions were stored at -20 °C when not in use.

Two methods of forming bilayers were studied: painting the bilayer and a "tip-dip" procedure. In both methods, the GNM was filled with buffered electrolyte and the orifice was submerged in a cell of the electrolyte. A painted bilayer refers to a bilayer formed by gently sweeping a pipette tip (#02-707-81, Fisherbrand) filled with lipid solution across the orifice of the submerged GNM.[28-30] The tip-dip bilayer is formed by passing the GNM pore through a lipid/aqueous interface twice; the GNM starts beneath the solution surface, lipid solution is added on top of the buffered electrolyte surface, the GNM is then brought out of

solution (depositing a monolayer), then re-submerged (forming a bilayer).[31,32] Bilayer formation, for both painting and tip-dip, was continuously monitored via the GNM orifice resistance. An open GNM displays a resistance of ~10 MΩ, while one modified with a suspended bilayer has a resistance of ~100 GΩ.[19] Once a bilayer was formed, pressure was used to thin the bilayer for α-HL channel reconstitution.[19,33] The Dagan pipette holder described above is used to seal the back end of the GNM, allowing for pressure (0-360 mmHg) to be applied to the inside of the GNM with respect to the external solution. The pipette holder is connected to a pressure line and syringe, and the applied pressure is monitored using a sphygmomanometer pressure gauge.

2.2.4 Contact Angle Measurements

Soda lime glass microscope slides were first cleaned in 0.1 M HNO_3 for ~10 min. After soaking, the slides were rinsed with ultrapure water, ethanol, and acetonitrile, followed by rinsing with the silane solutions as described above. The slides were soaked in the silane solution for a specified interval of time, for periods ranging up to 3 days. After silanization, the slides were rinsed with acetonitrile, ethanol, and ultrapure water, and then dried with a nitrogen stream. Contact angles of 2 μL drops of ultrapure water placed on the microscope slide surface were measured by photographing the drop within five seconds of placing the drops on the surface. A minimum of three drops were measured for each reaction time. Photographs were taken with a Panasonic FZ18 camera and contact angle images were analyzed in Adobe Photoshop CS3. Advancing and

receding angle measurements were not performed. All steps and measurements were performed at room temperature.

2.2.5 Smallest Wetting Radius

GNMs were fabricated as described above, and size characterization was performed as previously described.[18,19,25] Upon formation of the Pt nanodisk electrode (Figure 2.1A), the radius of the disk was electrochemically determined by monitoring the limiting steady-state current for the oxidation of 5 mM ferrocene at room temperature using a scan rate of 50 mV/s. The relationship between the limiting current, i_d, and the orifice radius, r, is given by eq. (2.1),[18,34]

$$i_d = 4nFDC^* r \tag{2.1}$$

where n is the number of electrons transferred per molecule, F is Faraday's constant, D is the diffusion coefficient for ferrocene in acetonitrile (2.5 x 10^{-5} cm^2s^{-1}), and C^* is the bulk concentration of ferrocene (5 mM). After removing the Pt, the radius of the unmodified glass nanopore membrane (Figure 2.1B) was determined by measuring the resistance of the orifice in a 1 M KCl solution, by scanning the applied voltage between -100 and +100 mV at 50 mV/s. The orifice radius r_1 is related to the pore resistance R_P by eq. (2.2),[25]

$$R_P = \frac{1}{\kappa r_1}\left(\frac{1}{\pi \tan\theta} + \frac{1}{4}\right) \tag{2.2}$$

where κ is the solution conductivity and θ is the cone angle of the nanopore. Taking θ to be ~10° and κ_{bulk} = 0.1119 $\Omega^{-1}cm^{-1}$ at 25 °C allows simplification of eq. (2.2) to eq. (2.3).[25,35]

$$r_1 = \frac{19}{R_P} \tag{2.3}$$

Finally, the GNM was silanized as described above and the nanopore orifice radius was measured in 1 M KCl using eq. (2.3).

2.2.6 Bilayer Resistance Measurements

The GNM was filled with the buffered electrolyte solution containing 0.75 μM α-HL. Once a bilayer was formed across the orifice of the GNM, an *i-V* trace was obtained by scanning the voltage from -100 to +100 mV at 50 $mV \cdot s^{-1}$. A continuous trace was recorded for the bilayer until α-HL reconstitution was observed, while applying ≥20 mmHg to the nanopore interior with respect to the external solution. From the measured *i-V* trace prior to α-HL reconstitution, the resistance of the bilayer was calculated through Ohm's Law. Bilayers that did not exhibit α-HL insertion were not considered functional bilayers and were excluded from analysis. Bilayer resistance measurements were performed for GNMs functionalized with CMCS, TMCS, BMCS, and C-18, having radii ranging from 500 nm to 1.5 μm. Bilayer resistance measurements were also performed for pores at different silanization reaction times, ranging from 0 to 360 min, and after

3 days. All resistance measurements were performed at room temperature and a minimum of five bilayer resistances were measured for each GNM.

2.2.7 Bilayer Voltage Stability Measurements

As above, the GNM was filled with the buffered electrolyte solution containing 0.75 μM α-HL. Upon bilayer formation, a pressure of approximately 20 mmHg was applied to the inside of the GNM with respect to the external solution. A *i-V* trace was obtained for applying an increasing voltage from 0 to 2 V at 50 mV/s. Upon bilayer rupture, a sudden increase in current indicates an open pore; the voltage at which this open pore current occurred is considered to be the bilayer rupture voltage. The typical rupture voltage for a GNM treated with CMCS is ~800 mV.[19] This experiment was performed for GNM with sizes ranging from 300 nm to 1.5 μm. A minimum of five rupture voltages were obtained for each pore size and each surface modification. Experiments were conducted at room temperature.

2.2.8 Bilayer Lifetime Measurements

The influence of surface hydrophobicity on the suspended bilayer lifetime, for CMCS, BMCS, and C-18 surface modifications, was monitored for bilayers exhibiting both protein insertion and s_7βCD detection. In these experiments, bilayers were formed using only the painting method with 10 mg DPhPC per mL decane. α-HL protein channel insertion was achieved with applied pressure ≥20 mmHg (internal vs. external solution). Once a functional α-HL channel was

reconstituted into the bilayer, an *i-t* trace was recorded to measure the bilayer lifetime. The bilayer lifetime was measured until spontaneous rupture. The bilayer was intentionally ruptured by applying 2 V if the lifetime exceeded 12 hrs.

2.3 Results and Discussion

2.3.1 Contact Angles

Contact angle measurements were used to monitor the formation of the silane monolayers. Figures 2.2A-2E show example contact angle images for unmodified glass, CMCS, TMCS, BMDS, and C-18 functionalizations. The water contact angles after 3-day silanization periods were as follows: 56 ± 1° for CMCS (reacted from acetonitrile), 86 ± 3° for TMCS (from acetonitrile), 93 ± 1° for BMCS (from acetonitrile), 95 ± 2° for C-18 (from toluene), 64 ± 3° for CMCS (from toluene), and 60 ± 4° for CMCS (from 1:1 acetonitrile/toluene). Untreated soda lime glass is hydrophilic and has a contact angle of ~16°. These results show that the silanization reaction proceeds well under moderate reaction conditions as hydrophobic surface modifications generally produce contact angles ranging from 80° to 110°.[36-39]

The kinetics of surface silanization were examined as a function of the reaction time (Figure 2.2F). Under the reaction conditions used here, the silanization reaction is essentially complete within a few hours. The more linear silanes (CMCS, BMCS, and C-18) reacted at a faster rate than the more

Figure 2.2. Contact angle images for (A) unmodified soda lime glass, (B) CMCS, (C) TMCS, (D) BMCS, and (E) C-18, modified soda lime glass (2 μL drop of ultra pure water). (F) Plot of the water contact angle as a function of silanization reaction time for reactions performed in either acetonitrile, toluene, or a mixture, for CMCS in acetonitrile (black), TMCS in acetonitrile (green), BMCS in acetonitrile (blue), C-18 in toluene (purple), CMCS in toluene (orange), and CMCS in 1:1 acetonitrile/toluene (pink).

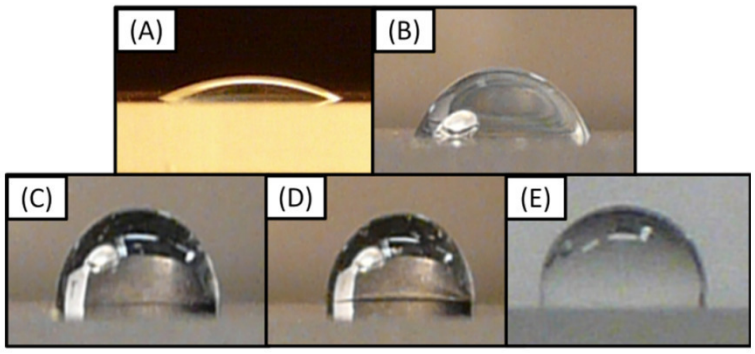
(A)
(B)
(C)
(D)
(E)

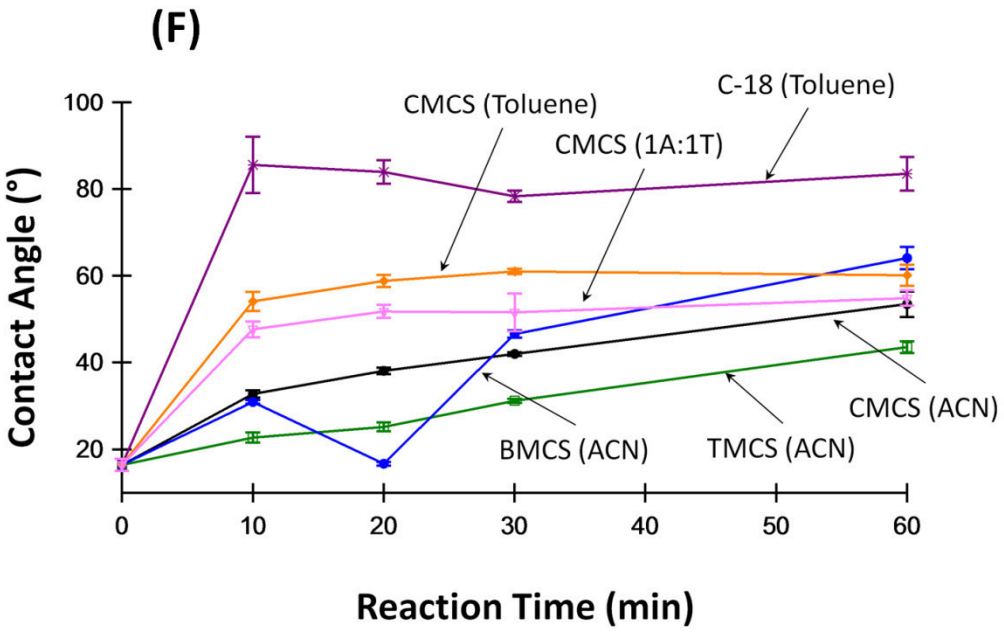
(F)
Contact Angle (°)
100
80
60
40
20
0
10
20
30
40
50
60
Reaction Time (min)
CMCS (Toluene)
C-18 (Toluene)
CMCS (1A:1T)
CMCS (ACN)
BMCS (ACN)
TMCS (ACN)

branched TMCS, which is expected as the branched methyl groups likely inhibit the formation of a dense monolayer.[38] CMCS in toluene reacted faster than CMCS in acetonitrile. The contact angle measurements demonstrate that only a few hours are needed to deposit a fully formed silane monolayer.

2.3.2 Smallest Wetting Radius

Initially, the CMCS surface functionalization was used as it provides an intermediate hydrophobicity and does not prevent wetting of the GNM pore, while allowing the formation of a suspended bilayer.[19] The smallest wetting GNM radius was determined for the more hydrophobic BMCS modification. GNMs were fabricated while monitoring the orifice size throughout the fabrication process as described above, for the nanodisk electrode, unmodified GNM orifice, and functionalized GNM orifice.

Figure 2.3 shows a comparison of the wetting characteristics of CMCS and BMCS-modified GNMs. A nanodisk electrode with an electroactive ~7 nm radius Pt disk was used for the CMCS surface modification. Once the Pt was removed, the GNM orifice radius was measured to be ~7 nm by a conductance measurement. After surface modification with CMCS, the orifice radius was reduced to be ~3 nm. These results demonstrate that the CMCS modification, with its intermediate hydrophobicity, does not prevent the wetting of GNM pores for the very smallest orifices (<10 nm), which is essential as all GNM based measurements depend on the ability to conduct ion current through the nanopore. In contrast, the BMCS modification is a hydrophobic surface

Figure 2.3. (A), (B), (C) Size characterization results for the fabrication of a 7-nm radius GNM using the CMCS modification, and (D), (E), and (F) characterization *i-V* traces for the fabrication of a 55-nm radius GNM for the BMCS modification. (A) and (D) show electrochemical *i-V* traces corresponding to the oxidation of 5 mM ferrocene in acetonitrile. (B) and (E) show conductivity *i-V* traces for a 7 nm nanopore membrane and a 55 nm nanopore membrane, respectively, in 1 M KCl. (C) shows a conductivity *i-V* trace for a CMCS modified nanopore membrane while (F) shows a conductivity *i-V* trace for a BMCS modified nanopore membrane.

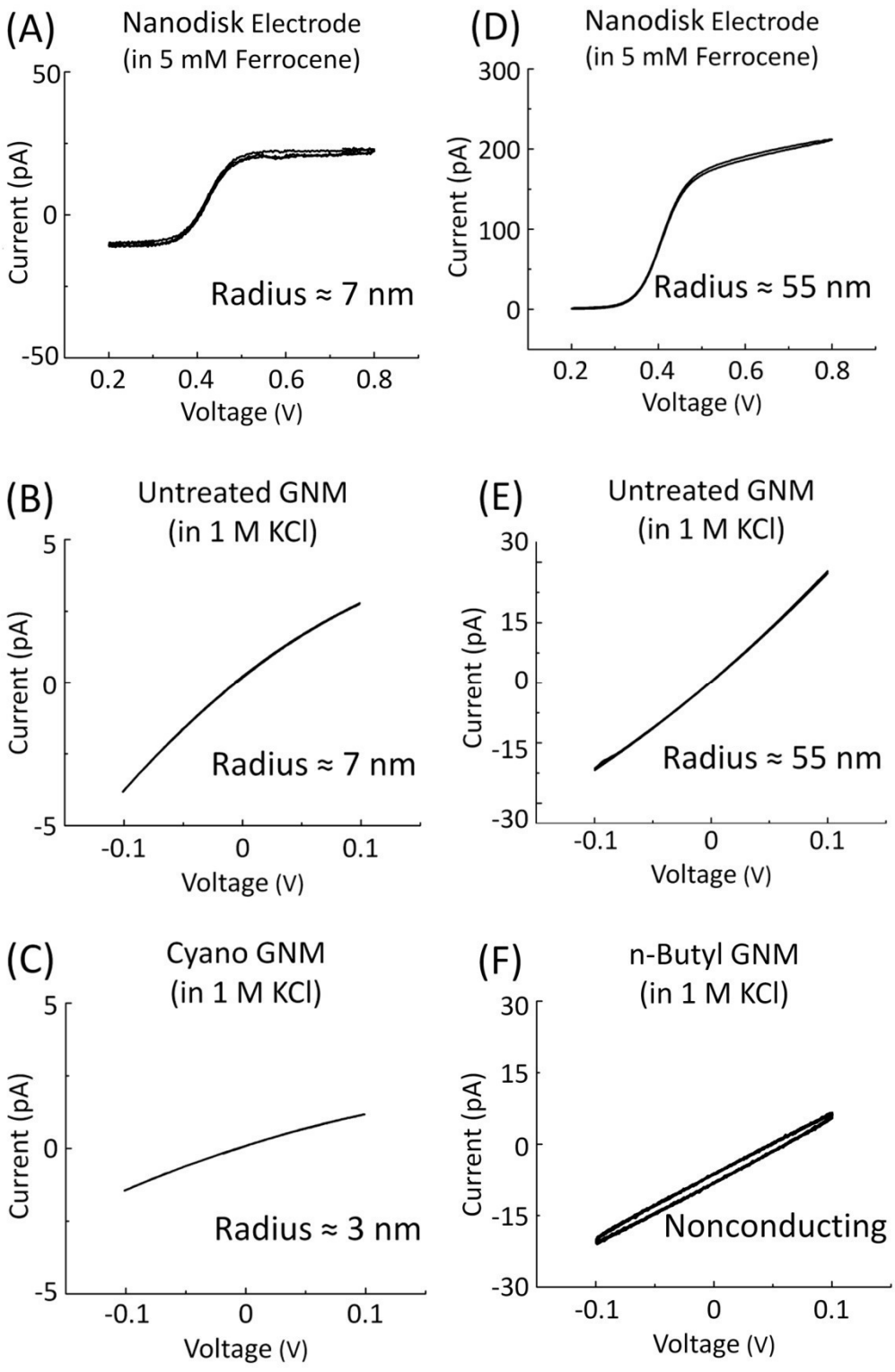
(A)
Nanodisk Electrode
(in 5 mM Ferrocene)
Current (pA)
Voltage (V)
Radius ≈ 7 nm
(D)
Nanodisk Electrode
(in 5 mM Ferrocene)
Current (pA)
Voltage (V)
Radius ≈ 55 nm
(B)
Untreated GNM
(in 1 M KCl)
Current (pA)
Voltage (V)
Radius ≈ 7 nm
(E)
Untreated GNM
(in 1 M KCl)
Current (pA)
Voltage (V)
Radius ≈ 55 nm
(C)
Cyano GNM
(in 1 M KCl)
Current (pA)
Voltage (V)
Radius ≈ 3 nm
(F)
n-Butyl GNM
(in 1 M KCl)
Current (pA)
Voltage (V)
Nonconducting

modification, as demonstrated with the contact angle measurements described above. A nanodisk electrode of ~55 nm radius was employed. When the Pt wire was removed, the orifice radius remained ~55 nm. However, when the GNM was functionalized with the BMCS silane, the pore would not wet as demonstrated with the reduced conductance in 1 M KCl; the BMCS functionalized pore showed a resistance of 4 GΩ corresponding to a non-physical ~0.04 nm radius based on eq. (2.3). In general, BMCS functionalized pores could not be reproducibly wetted for r < 100 nm. Although hydrophobic silanes inhibit the wetting of small GNMs, they do not place a limit on the GNM orifice size for ion channel recordings, as these measurements are typically performed with orifices greater than 100 nm.

2.3.3 Bilayer Resistance Measurements

We previously demonstrated that when an unmodified GNM is used as a bilayer support, the hydrophilic nature of the glass causes the lipid solution to form a spanning bilayer over the GNM surface, with the polar lipid head groups oriented towards the glass surface. An aqueous layer is present between the lipid molecules and the support surface resulting in a bilayer-substrate seal of ~7 GΩ.[25] Chemical modification of the GNM with CMCS generates a surface of intermediate hydrophobicity, resulting in the formation of lipid monolayer with the lipid tails oriented toward the surface. This lipid orientation produces a bilayer suspended over the orifice with a bilayer-substrate seal of ~100 GΩ using GNMs, and > 1TΩ on fused quartz nanopore mebmranes.[19] Based on these

results, it seems plausible that more hydrophobic surfaces will yield a stronger association between the lipid molecules and the support.

The resistance of the bilayer-substrate seal was measured for CMCS, TMCS, BMCS, and C-18 functionalized GNMs following bilayer formation via the painting method. GNMs with radii of ~500 nm were silanized for 3 days. The final bilayer-substrate resistances were as follows: 54 ± 16 GΩ for CMCS (reacted from acetonitrile), 148 ± 14 GΩ for TMCS (from acetonitrile), 165 ± 32 GΩ for BMCS (from acetonitrile), 101 ± 46 GΩ for C-18 (from toluene), 104 ± 45 GΩ for CMCS (from toluene), and 217 ± 40 GΩ for CMCS (from 1:1 acetonitrile/toluene). Generally, the bilayer resistance for the hydrophobic silanes was greater compared with CMCS, with the exception of the C-18 modification. Silanization reactions using toluene as a solvent produced less resistant bilayers relative to modification using acetonitrile as the solvent. We note that the C-18 modification yielded GNMs that had inconsistent wetting and functional bilayer formation. To examine whether this was due to the surface hydrophobicity or the use of the alternate reaction solvent toluene (C-18 does not dissolve in acetonitrile), the CMCS reaction was performed using toluene and 1:1 mixtures of acetonitrile/toluene. The CMCS modification in toluene and in 1:1 acetonitrile/toluene exhibited similar wetting and bilayer formation issues as for C-18. This indicated that there was an issue using toluene as the solvent and use of nonpolar solvents was discontinued after these preliminary measurements.

The influence of reaction kinetics for surface silanization of conical GNM pores was examined over shorter reaction periods. Figure 2.4A shows the bilayer resistance as a function of the silanization reaction time. The time period required to form a resistive bilayer seal at the GNM correlated well with the development of the contact angles measured on planar microscope slides, and indicates that silanization only needs to be carried out over a few hours to form a bilayer with a giga-ohm seal resistance. Additionally, the results demonstrate that the measured bilayer resistance also correlates with the surface hydrophobicity. The resistance measurements were extended to GNMs with radii of 500 nm and 1500 nm after 3 days of silanization; the results shown in Figure 2.4B indicate that more hydrophobic silane modifications yield suspended bilayers with larger seal resistances.

As a final study of the bilayer resistance as a function of surface hydrophobicity, the bilayer resistance was measured for bilayer formed via tip-dip and lipid solutions with different solvents. Figure 2.5 compares the bilayer seal resistance for CMCS, TMCS, and BMCS modified GNM suspended bilayers formed by the painting and tip-dip methods, using either 10 mg DPhPC per mL decane or 5 mg DPhPC per mL (1:1 decane/hexane). In general, bilayers formed by the tip-dip method and/or using the less concentrated lipid solution displayed lower seal resistances in comparison to bilayers formed through painting and using 10 mg DPhPC per mL decane. Among these bilayers, those supported on the more hydrophobic surface (treated with TMCS and BMCS) had higher seal resistances than those formed on the CMCS treated surface.

Figure 2.4. (A) Measured DPhPC bilayer resistance as a function of GNM silanization reaction time for CMCS (solid line), TMCS (dashed line), and BMCS (dotted line) modified GNMs. All pores have radii of ~1.5 μm. (B) Measured bilayer resistance for a DPhPC bilayer suspended over ~500 nm and ~1.5 μm radius pores CMCS (back), TMCS (dark grey), and BMCS (light gray) treated GNM.

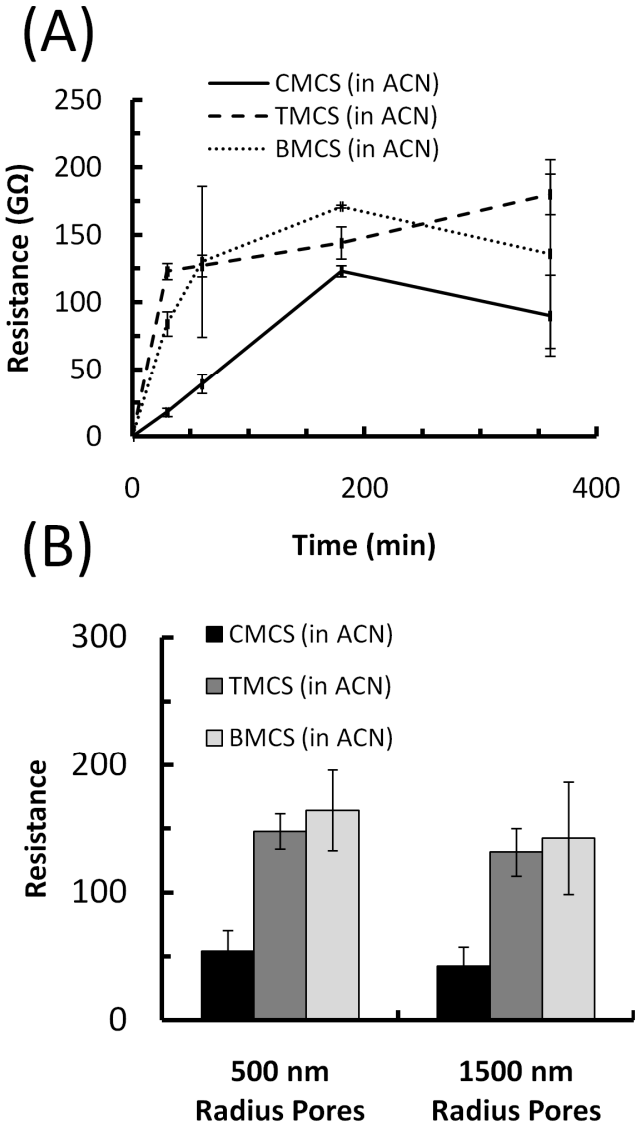
(A)
CMCS (in ACN)
TMCS (in ACN)
BMCS (in ACN)
Resistance (GΩ)
250
200
150
100
50
0
0
200
400
Time (min)
(B)
CMCS (in ACN)
TMCS (in ACN)
BMCS (in ACN)
Resistance
300
200
100
0
500 nm Radius Pores
1500 nm Radius Pores

Figure 2.5. Measured DPhPC bilayer resistance for both painting and tip-dip methods of preparing bilayers in combination with lipid solutions containing 10 mg DPhPC per mL decane or 5 mg DPhPC per mL (1:1 decane/hexane), abbreviated 1D:1H, for CMCS (back), TMCS (dark grey), and BMCS (light gray) modified GNMs. Measurements were taken for pores with ~1.5μm radius dimensions.

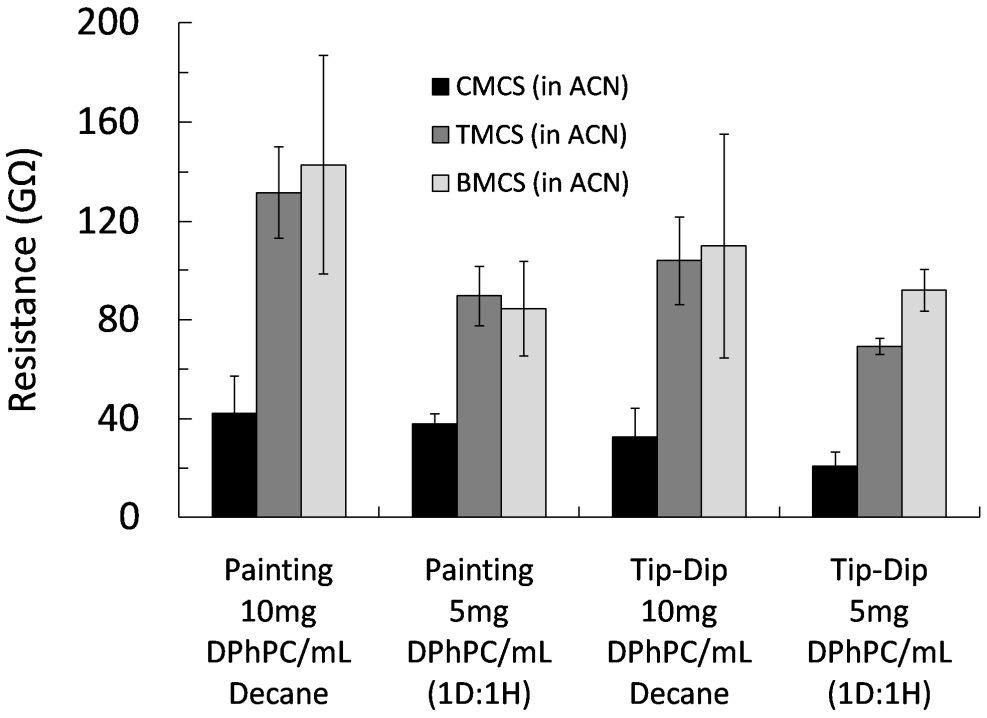
200
160
120
80
40
0
Resistance (GΩ)
CMCS (in ACN)
TMCS (in ACN)
BMCS (in ACN)
Painting 10mg DPhPC/mL Decane
Painting 5mg DPhPC/mL (1D:1H)
Tip-Dip 10mg DPhPC/mL Decane
Tip-Dip 5mg DPhPC/mL (1D:1H)

2.3.4 Bilayer Voltage Stability Measurements

The rupture voltage of bilayers formed on modified GNMs was compared as a measure of the bilayer stability. Figure 2.6 summarizes rupture voltage values for ~300-, ~500-, and ~1500-nm radius GNMs modified for 3 days using CMCS, TMCS, and BMCS. The average rupture voltages were as follows for ~500 nm orifice GNMs: 565 ± 254 mV for CMCS (reacted in acetonitrile), 888 ± 182 mV for TMCS (from acetonitrile), 848 ± 325 mV for BMCS (from acetonitrile), 517 ± 280 mV for C-18 (from toluene), 545 ± 190 mV for CMCS (from toluene), and 692 ± 327 mV for CMCS (from 1:1 acetonitrile/toluene). No significant improvement of rupture voltage was found using the more hydrophobic silanes.

2.3.5 Bilayer Lifetime Measurements

An advantage of the GNM is the ability to reproducibly form long-lived bilayers.[19] Bilayer lifetimes were measured here for CMCS, BMCS, and C-18 functionalized GNMs to determine and compare the frequency for which bilayers can be formed. The operative pressure range for α-HL reconstitution was also investigated. Of 45 bilayers prepared on CMCS functionalized GNMs (radii ranging from 500-1000 nm), 27 had lifetimes ≥12 hrs and 20% had lifetimes of 1-12 hrs. Additionally, bilayers formed on CMCS modified GNMs had a functional pressure range of 20-180 mmHg. The BMCS functionalized GNMs, with radii ranging from 700-1000 nm, resulted in 14% of bilayers (21 bilayers total) having lifetimes exceeding 12 hrs and 20% with lifetimes of 1-12 hrs, and required a larger pressure (40-230 mmHg) relative to the CMCS modified GNMs to achieve

Figure 2.6. Rupture voltage for painted (with 10 mg DPhPC per mL decane) bilayers as a function of GNM pore size for CMCS (black), TMCS (dark grey), and BMCS (light grey) treated GNMs.

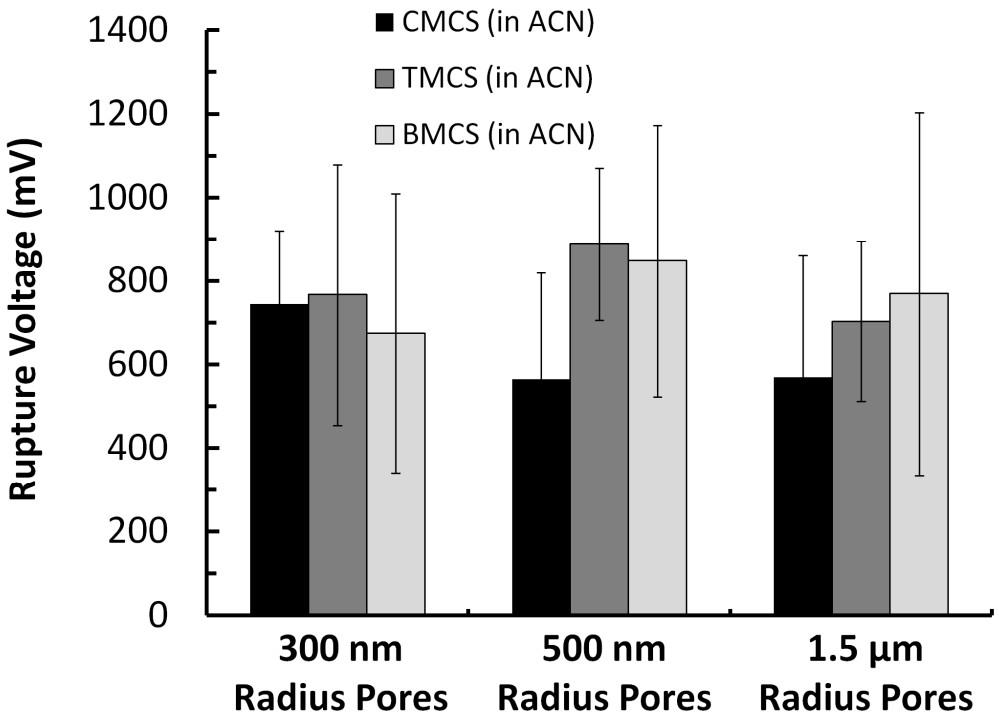
CMCS (in ACN)
TMCS (in ACN)
BMCS (in ACN)
Rupture Voltage (mV)
1400
1200
1000
800
600
400
200
0
300 nm Radius Pores
500 nm Radius Pores
1.5 µm Radius Pores

α-HL reconstitution. The C-18 modified GNMs produce long-lived bilayers for ~ 25% of the bilayers formed (8 bilayers total), 13% with lifetimes of 1-12 hrs, and had protein insertion occur for a narrower applied pressure range (20-90 mmHg) for pores with radii ranging from 600-1000 nm. The lower pressure range and the lack of bilayers with intermediate lifetime length is consistent with the bilayer resistance measurements where it was determined that the C-18 functionalization resulted in a higher rate of bilayer failure. Overall, the lifetime measurements are similar between the different silanes, consistent with the bilayer resistance and rupture voltage measurements.

2.4 Conclusions

The more hydrophobic silanes TMCS and BMCS were found to be useful modifications for GNM supported bilayers. Increased surface hydrophobicity appears to improve the seal between the bilayer and the substrate, as seen from the measured increase in bilayer resistance. However, the overall bilayer stability does not improve significantly with the increased hydrophobicity as measured by the rupture voltage and lifetime measurements. Interestingly, while hydrophobic modifications inhibit the wetting ability of the pore for orifices with radii < 100 nm, the CMCS modification will continue to allow the pore to wet for r < 10nm. The CMCS modification may have applications for solid-state nanopore measurements where very small orifices with intermediate hydrophobic character are required.

2.5 References

(1) Terstappen, G. C. *Drug Discov. Today* **2005**, *2,* 133-140.

(2) Dabraoski, M. A.; Dekermendjian, K.; Lund, P.-E.; Krupp, J. J.; Sinclair, J.; Larsson, O. *CNS Neurol. Disord.: Drug Targets* **2008**, *7*, 122-128.

(3) Haddock, P. *American Pharmaceutical Review* **2006**, *9*, 119-122.

(4) Landry, Y.; Gies, J.-P. *Fundam. Clin. Pharmacol.* **2008**, *22*, 1-18.

(5) Jean-Yves, Le G.; Olivier, S.; Pierre, B.; Ahmed, A.; Christophe, V. *Recent Pat. Anti-Cancer Drug Discovery* **2007**, *2*, 189-202.

(6) Shim, J. W.; Gu, L. Q. *Anal. Chem.* **2007**, *79*, 2207-2213.

(7) Gu, L.-Q.; Braha, O.; Conlan, S.; Cheley, S.; Baley, H. *Nature* **1999**, *398*, 686-690.

(8) Bayley, H.; Braha, O.; Gu, L.-Q. *Adv. Mater.* **2000**, *12*, 139-142.

(9) Braha, O.; Gu, L.-Q.; Zhou, L.; Xiaofeng, L.; Cheley, S.; Bayley, H. *Nat. Biotechnol.* **2000**, *18*, 1005-1007.

(10) Deamer, D.; Branton, D. *Acc. Chem. Res*. **2002**, *35*, 817-825.

(11) Vercoutere, W. A.; Winters-Hilt, S.; DeGuzman, V. S.; Deamer, D.; Ridino, S. E.; Rodgers, J. T.; Olsen, H. E.; Marziali, A.; Akeson, M. *Nucleic Acids Res.* **2003**, *31*, 1311-1318.

(12) DeGuzman, V. S.; Lee, C. C.; Deamer, D. W.; Vercoutere, A. *Nucleic Acids Res.* **2006**, *34*, 6425-6437.

(13) Kasianowicz, J. J.; Brandin, E.; Branton, D.; Deamer, D. W. *Proc. Natl. Acad. Sci.* **1996**, *93*, 13770-13773.

(14) Akeson, M.; Branton, D.; Kasianowicz, J. J.; Brandin, E.; Deamer, D. W. *Biophys. J.* **1999**, *77*, 3227-3233.

(15) Meller, A.; Nivon, L.; Brandin, E.; Golovchenko, J.; Branton, D. *Proc. Natl. Acad. Sci.* **2000**, *97*, 1079-1084.

(16) Schibel, A. E. P.; An, N.; Jin, Q.; Fleming, A. M.; Burrows, C. J.; White, H. S. *J. Am. Chem. Soc.* **2010**, *132*, 17992-17995.

(17) Zhang, B.; Zhang, Y.; White, H.S. *Anal. Chem.* **2004**, 76, 6229-6238.

(18) Zhang, B.; Galusha, J.; Shiozawa, P.G.; Gangli, W.; Bergren, A.J.; Jones, R.M.; White, R.J.; Ervin, E.N.; Cauley, C.C.; White, H.S. *Anal. Chem.* **2007**, 79, 4778-4787.

(19) White, R.J.; Ervin, E.N.; Yang, T.; Chen, X.; Daniel, S.; Cremer, P.S.; White, H.S. *J. Am. Chem. Soc.* **2007**, 129, 11766-11775.

(20) Kawano, R.; Schibel, A. E. P.; Cauley, C.; White, H. S. *Langmuir* **2008**, *25*, 2850-2855.

(21) Ervin, E. N.; Kawano, R.; White, R. J.; White, H. S. *Anal. Chem.* **2008**, *80*, 2069-2076.

(22) Ervin, E. N.; Kawano, R.; White, R. J.; White, H. S. *Anal. Chem.* **2008**, *81*, 533-537.

(23) Lathrop, D. K.; Ervin, E. N.; Barrall, G. A.; Keehan, M. G.; Kawano, R.; Krupka, M. A.; White, H. S.; Hibbs, A. H. *J. Am. Chem. Soc.* **2010**, *132*, 1878-1885.

(24) Chen, Q.; Liu, J.; Schibel, A. E. P.; White, H. S.; Wu, C. *Macromolecules* **2010**, *43*, 10594-10599.

(25) White, R.J.; Zhang, B.; Daniel, S.; Tang, J.M.; Ervin, E.N.; Cremer, P.S.; White, H.S. *Langmuir* **2006**, 22, 10777-10783.

(26) White, S. H. The Physical Nature of Planar Bilayer Membranes. In *Ion Channel Reconstitution*; Miller, C. Ed.; Penum Publishing Co.: New York, 1986, pp 3-35.

(27) White, S.H. *Biophysical Journal* **1972**, 12, 432-445.

(28) Alverez, O. How to Set Up a Bilayer System. In *Ion Channel Reconstitution*; Miller, C. Ed.; Plenum Publishing Co.: New York, 1986; pp 115-130.

(29) Mueller, P.; Rudin, D.O.; Tien, H.T.; Wescott, W.C. *Circulation* **1962**, 26, 1167-1171.

(30) Mueller, P.; Rudin, D.O.; Tien, H.T.; Wescott, W.C. *Nature* **1962**, 194, 979-980.

(31) Suarez-Isla, B.A.; Wan, K.; Lindstrom, J.; Montal, M. *Biochemistry* **1983**, 22, 2319-2323.

(32) Ehrlich, B. *Methods in Enzymology* **1992**, 207, 463-470.

(33) Schibel, A. E. P.; Heider, E. C.; Harris, J. M.; White, H. S., *Fluorescence Microscopy of the Pressure-Dependent Structure of Lipid Bilayers Suspended Across Conical Nanopores,* in preparation.

(34) Saito, Y. *Rev. Polarogr.* **1968**, *15*, 177.

(35) (a) Kroner, R. C. *J.AOAC,* **1973**, 56, 295; (b) Pratt, K. W.; Koch, W.F.; Wu, Y.C.; Berezansky *Pure Appl. Chem.,* **2001***, 73,* 1783.

(36) Wei, M.; Bowman, R. S.; Wilson, J. L.; Morrow, N. R. *J.Colloid. Interface Sci.* **1993**, *157*, 154-159.

(37) Miyama, M.; Yang, Y.; Yasuda, T.; Okuno, T.; Yasuda, H. *Langmuir*, **1997**, *13*, 5494-5503.

(38) Fadeev, A. Y.; McCarthy, T. J. *Langmuir* **1999**, *15*, 3759-3766.

(39) Horr, T. J.; Ralston, J.; Smart, R. S. C. *Colloids Surf., A* **1995**, *97*, 183-196.

CHAPTER 3

QUARTZ NANOPORE MEMBRANES FOR SUSPENDED BILAYER ION CHANNEL RECORDINGS

3.1 Introduction

This paper describes the fabrication of fused quartz nanopore membranes (QNM) for ion-channel recordings. Ion channel recordings using synthetic lipid bilayers are of growing interest in the development of stochastic biosensors and biopolymer characterization, in addition to their long-standing use in electrophysiology studies.[1-6] In these measurements, a lipid bilayer is suspended across a 10 to 100 μm-diameter opening in a polymer membrane, e.g. Teflon, and an ion channel (or multiple channels) is inserted or reconstituted in the bilayer. Ion channel recordings using lipid bilayers suspended across the orifice of a single conical-shaped nanopore prepared in an ~50 μm-thick membrane of soda-lime glass have been reported,[7-10] including recent studies of the temperature-dependent diffusion of DNA within α-hemolysin ion channels.[11] The small dimensions of the nanopore orifice in these glass nanopore membranes (GNM) result in a bilayer that is less susceptible to mechanical vibration, has

Reproduced with permission from Anna E. P. Schibel, Thomas Edwards, Ryuji Kawano, Wenjie Lan, and Henry S. White "Quartz Nanopore Membranes for Suspended Bilayer Ion Channel Recordings." *Anal. Chem.* **2010**, *82*, 7259-7266.

significantly increased voltage stability (breakdown at 0.8 V), and improved lifetime (days to weeks). In addition, the area of the bilayer suspended across the GNM orifice is ~100,000x smaller than the bilayer in traditional setups,[7] virtually eliminating the bilayer capacitance in limiting the rate of data acquisition.[12] The small bilayer area provides the advantage of limiting the number of protein insertions in the bilayer, simplifying the signal analysis in many applications.

Ion channel recording devices have been previously fabricated from fused quartz, with an emphasis on reducing the system capacitance, in addition to taking advantage of the favorable optical properties to combine ion channel recordings with spectroscopic measurements. Some devices that have been made from fused quartz include cells,[13] planar chips,[14,15] patch pipettes,[16,17] and nanochannels,[18] all of which were developed to improve the insulation between the internal and external solutions and to increase signal to noise. Fused quartz cells containing a 0.72 mm radius orifice exhibited bilayer-substrate seals of ~15 GΩ.[13,19] Planar glass chips, with pore radii ranging from sub-μm to μm dimensions, also resulted in giga-ohm bilayer-support seal resistances (~5 GΩ).[14,15] Fused quartz patch pipettes displayed bilayer-substrate seal resistances up to ~125 GΩ for orifices of micrometer dimensions. These fused quartz devices are limited by low bilayer-substrate seal resistances and require intensive fabrication processes associated with working with fused quartz.[20]

Herein, we describe a bench-top fabrication procedure for QNMs with radii as small as 6 nm. We demonstrate that nanopore membranes prepared from fused quartz capillaries are suitable for ion channel recordings, as demonstrated

by the detection of single-stranded DNA (ssDNA)[21-29] using α-hemolysin (α–HL)[30-32] embedded in a bilayer suspended across the QNM orifice. These structures, shown in Figure 3.1, have the further advantage of remarkably low electrical leakage currents, while maintaining the other favorable properties of GNMs. The measured lipid bilayer seal resistances are immeasurably large (>1 TΩ), providing significantly lower background currents than previously achieved. The "seal resistance" of lipid bilayers is a key metric in ion channel recordings, and is associated with leakage currents. Possible sources of leakage current include ion transfer across the lipid bilayer, ion fluxes along the interface of the bilayer/support structure, and ionic conduction in the solid support structure. In this work, we compare the performance of glass and fused quartz nanopore membranes (QNMs), and demonstrate that the leakage current using GNMs is solely due to Na^+ conduction in the glass, resulting from a potential difference across the glass membrane, and similar to that occurring with glass pH electrodes. This ion flux limits the seal resistance in these devices to ~100 GΩ, a value comparable to seal resistances of large area bilayers suspended across orifices in conventional polymeric materials.

3.2 Experimental Section

3.2.1 Chemicals and Materials

All aqueous solutions were prepared with >18 MΩ·cm water from a Barnstead E-pure water purifier. NaOH, $CaCl_2$, KCl, K_2HPO_4, KH_2PO_4, and EDTA (Mallinckrodt), NaCN, decane (Fisher Scientific), and trizma base (Sigma-

Figure 3.1. (A) Photograph of a QNM located at the sealed face of the capillary (left end). A Ag/AgCl electrode is inserted in the capillary. (B) Schematic of the GNM or QNM (not to scale). (C) Schematic drawing of a DPhPC bilayer suspended across the orifice of a QNM modified with 3-cyanopropyldimethyl-chlorosilane (not to scale).

(A)

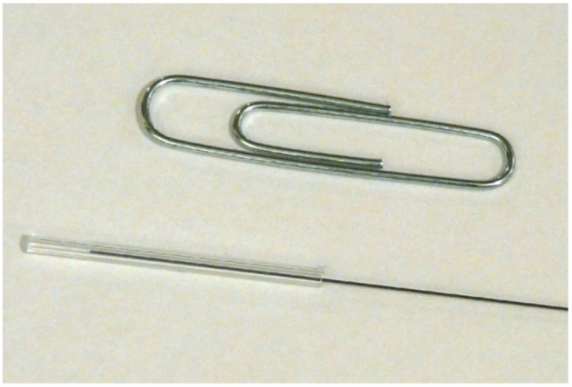

(B)

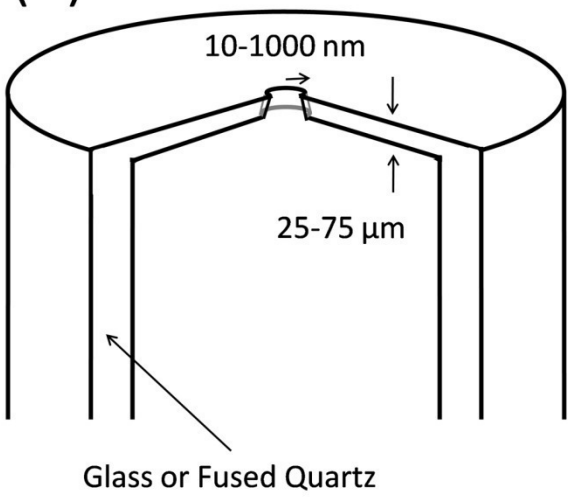

(C)

Aldrich) were used as received. Buffered electrolyte solutions of either 1.0 M KCl, 30 mM Tris, and 10 mM EDTA (adjusted to pH 8) and 1.0 M KCl, 25mM PBS, and 1.0 mM EDTA (pH 7.0) were prepared from ultrapure water. The phospholipid, 1,2-diphytanoyl-*sn*-glycero-3-phosphocholine (DPhPC, Avanti Polar Lipids) was dispersed in chloroform and stored at -20 °C. 3-cyanopropyldimethylchlorosilane ($Cl(CH_3)_2Si(CH_2)_3CN$, Gelest, Inc.) was used as received. HPLC grade acetonitrile (CH_3CN, Fisher Scientific) was stored over 3 Å molecular sieves. Soda lime glass (Corning, 2948-3x1) and fused quartz (Alfa Aesar, 42295) slides were cleaned in 0.1 M HNO_3 (EMD) prior to use. Soda lime glass capillaries were obtained from Dagan, Corp. (1.65 mm O.D., 0.75 mm I.D., Cat. # SB16). Fused quartz capillaries were received from Sutter Instruments (1.65 mm O.D. and 1.15 mm I.D., cat. no. Q165-115-10). Tungsten rods were obtained from FHC, Inc. and 0.025 mm W wire was purchased from Alfa Asear (#10405). The 400, 800, and 1200 grit paper disks, PSA backed microcloth, and Micropolish II 0.05 μm alumina particles were all from Buehler.

α–HL (Sigma-Aldrich) was obtained as the monomer polypeptide, isolated from *Staphylococcus aureus,* in the form of a lyophilized powder and dissolved at a concentration of 0.6 mg protein/mL ultrapure water. When not in use, the α–HL solution was stored at -80 ˚C. During use, samples were diluted to the desired concentration using a buffered electrolyte solution and stored at 4 ˚C. Single-stranded poly-dA 20-mer and poly-dA 50-mer DNA sequences were obtained as a powder from Sigma-Aldrich and stored at -20 °C.

3.2.2 Surface Modification and Contact Angle Measurements

Soda lime glass and fused quartz microscope slides were cleaned in 0.1 M HNO_3 for approximately 10 min, after which slides were rinsed thoroughly with ultrapure water, followed by ethanol, CH_3CN, and a 2% (v:v) CH_3CN solution of 3-cyanopropyldimethylchlorosilane. Slides were immersed overnight in the 3-cyanopropyldimethylchlorosilane solution. After silanization, the slides were rinsed with CH_3CN, ethanol, and water. Contact angles were measured by depositing a 2 µL drop of ultrapure water on the unmodified and modified surfaces and taking a photo of the drop within 5 s of placing the drop (to minimize evaporation), using a tripod-mounted Panasonic FZ18 camera at room temperature. Contact angle images were analyzed in Adobe Photoshop CS3.

3.2.3 Nanopore Membrane Fabrication

The fabrication of GNMs was previously published,[33] and is very briefly described here. A ~1 cm-length of a 25-µm diameter Pt wire is electrochemically sharpened in a 6 M NaCN and 0.1 M NaOH solution. The wire is connected to a stiff tungsten (W) rod, and then sealed using a H_2 flame to the softened end of a soda lime glass capillary. Once cooled, the excess glass is polished away to expose a Pt disk; an electrical continuity circuit is used to determine when the Pt is exposed during polishing and indicate when the desired Pt disk radius has been achieved. Once the desired disk radius has been attained, the sealed Pt wire is electrochemically removed by first etching the exposed Pt in a 20% (w:v) $CaCl_2$ solution, followed by manually pulling the wire from the glass membrane.

The orifice radius of the resulting conically shaped pore is determined by measuring the ohmic resistance of the pore in a 1 M KCl solution, as described below.

QNM fabrication follows the above procedure with adaptations to accommodate the properties of fused quartz. A 1 cm-long segment of W wire (0.025 mm diameter) was attached to a W rod via silver conducting paste and heated in an oven at approximately 150° C for 30 min. The W wire was then electrochemically sharpened in 1.5 M NaOH solution with an applied voltage of 10 V_{PP} at 60 Hz using an Agilent 33220A 20 MHz Function, Arbitrary Waveform Generator. The end of a fused quartz capillary was initially sealed with an H_2/O_2 flame. The sharpened W wire (~10^o half-cone angle) was inserted into the capillary and positioned close to, but not touching, the sealed end of the capillary. The position of the W wire was visually confirmed with a microscope. The capillary was heated a second time in the H_2/O_2 flame to seal the sharpened W wire in the fused quartz at a depth of 25-75 μm. During the second heating, a vacuum was applied to the end of the capillary. The bulk of the fused quartz membrane was polished away on 400, 800, and 1200 grit Buehler microcut paper disks. Final polishing was on a Buehler PSA backed microcloth with Buehler Micropolish II 0.05μm alumina particles and a 1 M KCl solution. Exposure of the W disk was monitored with the continuity circuit as described above. Once the disk was exposed, the W wire within the pore was etched in 1.5 M NaOH solution using an applied voltage of 10 V_{PP} at 60 Hz. Etching was performed until the W wire could be manually removed by gentle pulling. The

radius of the resulting conical shaped pore was then confirmed as described below.

The surfaces of the GNM and QNM membranes are chemically modified with a 3-cyanopropyldimethylchlorosilane monolayer to produce a surface of intermediate hydrophobicity. When depositing lipid on the surface for bilayer formation, this surface modification results in lipid monolayer formation on the glass and quartz surface and a lipid bilayer suspended across the small orifice of the membrane. Before silanization, both the GNM and QNM were cleaned inside and out by filling and soaking the capillaries in 0.1 M HNO_3 for approximately 10 min. The pores were then thoroughly rinsed with ultrapure water, ethanol, CH_3CN, and finally 2% (v:v) 3-cyanopropyldimethylchlorosilane in CH_3CN. The pores were then filled with the 2% silane solution and left for 24 hrs at room temperature, after which the pores were rinsed with CH_3CN, ethanol, and ultrapure water. Silanized GNMs and QNMs were stored in absolute ethanol. Before use, nanopore membranes were rinsed multiple times with ultrapure water.

3.2.4 Sealed Membrane Fabrication

Glass and quartz membranes *without nanopores* were prepared in order to determine the electrical properties of the membrane in the absence of a nanopore. The soda lime and fused quartz capillaries were sealed at one end using a H_2 or H_2/O_2 flame. The excess glass was removed through polishing as described above to produce 25-75 μm thick glass or quartz membranes at the

end of the capillary, as confirmed by optical microscopy. The sealed capillary was cleaned in 0.1 M HNO_3 for 10 min. The capillaries were then silanized with 3-cyanopropyldimethylchlorosilane and stored as described above.

3.2.5 Electrical Measurements

Current-time (*i-t*) and current-voltage (*i-V*) measurements were performed using a PC interfaced with a Dagan Corporation CHEM-CLMAP (Voltammeter and Amperometer Voltage Clamp Amplifier) and a Pine Instrument Company RDE4 Analog Bipotentiostat. An in-house written LabVIEW 8.2 (National Instruments) program was used to record *i-V* and *i-t* traces. Currents were measured between a Ag/AgCl electrode placed inside the GNM/QNM or sealed capillary, and a second Ag/AgCl electrode in the external solution. The Ag/AgCl electrodes were prepared by soaking clean 0.25 and 0.5 mm diameter silver wire (Alfa Aesar) in bleach for approximately 30 min and then rinsing thoroughly with water.

3.2.6 Bilayer Formation

Suspended bilayers across the GNM or QNM orifice were created by the painting technique.[34] Chloroform was evaporated from the 10 mg DPhPC lipid solution with a nitrogen stream, and 1 mL decane was added to re-disperse the lipid. The GNM/QNM was filled with buffered electrolyte, submerged in a cell containing the same solution, and a voltage was applied across the orifice. A clean plastic pipette (Fisherbrand #02-707-81) filled with 10 mg DPhPC per mL

decane was gently swabbed across the orifice of the GNM/QNM until a bilayer was formed. The pore conductance was monitored during bilayer formation; for a ~500 nm radius orifice, the pore conductance decreases from ~10 MΩ to ~100 GΩ for GNMs and to >1TΩ for QNMs. Successful reconstitution of properly functioning α–HL is used to determine if a true bilayer is formed. When α–HL inserts into a properly formed bilayer there is a discrete increase in the conductance corresponding to the literature value of ~ 1 nS.[35]

As detailed previously, a positive pressure across the membrane is required to reconstitute transmembrane proteins into a bilayer suspended across a conical-shaped pore.[7] The pressure across the bilayer membrane was controlled by inserting the open end of the GNM or QNM into a pipette holder (DAGAN) that was connected to a 10-mL gas-tight syringe (Hamilton). The pressure was monitored continuously using a sphygmomanometer (pressure sensing range of -100 to 300 mmHg). All transmembrane pressures reported herein are referenced to the exterior (ambient) solution pressure.

3.2.7 Single-Stranded DNA Translocation

Solutions of poly-dA 20-mer and poly-dA 50-mer were diluted to a concentration of approximately 10 μM in a 1 M KCl, 25 mM PBS, and 1 M EDTA (pH 7) buffer. The ssDNA and α–HL (approximate 30 nM) were placed in the external solution and the internal volume filled with buffered electrolyte. The QNM/GNM was secured via a Dagan Corporation Pipette Holder. At room temperature, a voltage of +100 mV was applied across the orifice, a bilayer was

formed, and pressure was applied to the inside of the capillary. Following protein reconstitution, ssDNA translocation events were recorded at a sampling rate of 150 kHz using a 10 kHz filter. Data were analyzed with an in-house MATLAB program to determine mean translocation times.

3.3 Results and Discussion

3.3.1 Surface Modification and Contact Angle Measurements

We previously reported that deposition of a monolayer of 3-cyanopropyldimethylchlorosilane on the GNM surface confers sufficient hydrophobic character to the glass to allow deposition of a lipid *monolayer* with the hydrophobic tails oriented toward the glass surface; lipid bilayer formation spontaneously occurs on unmodified glass.[7] At the same time, the 3-cyanopropyldimethylchlorosilane monolayer is sufficiently hydrophilic to allow an aqueous solution to fill the nanopore. The fusing of the two lipid monolayers from the internal and external surfaces creates a bilayer *suspended* over the nanopore orifice, Figure 3.1C. Analogous to bilayers painted across holes in Teflon and other hydrophobic polymer membranes, we speculate that an annulus region containing the lipid painting solution (decane and lipid) exists adjacent to the nanopore circumference.[36]

The suspended bilayer structure has two advantages over lipid bilayers that are simply *supported* over orifices in unmodified glass or quartz surfaces.[37] First, the fusing of the two monolayers reduces the leakage current in ion channel recordings. In supported bilayers, the thin water layer (~1 nm thick) that

exists between the polar head groups of the lipids and the glass surface can act as an effective current shunt, greatly lowering the apparent bilayer seal resistance.[37] Second, because the protein ion channels are functional only in a lipid bilayer (and not the lipid monolayer), the ion channel signal arises only from proteins inserted or reconstituted within the area defined by the GNM or QNM orifice.

The schematic of the nanopore membrane presented in Figure 3.1 is meant to represent the system components and not the actual bilayer structure. Specifically, fluorescence microscopy has been used to study the effect of the pressure on the flatness of the suspended bilayer. Preliminary evidence suggests that the bilayer structure bulges slightly out from the orifice when pressure is applied for ion channel insertion; details are reported Chapter 4.

The contact angles of water on soda lime glass and quartz increased from ~16° and ~35°, respectively, to ~55° and ~57° after silanization with 3-cyanopropyldimethylchlorosilane, in agreement with a previously reported contact angle value on silanized glass.[7] The equivalent contact angles on glass and quartz following silanization suggest that silane monolayer formation is similar on both substrates. Previous fluorescence microscopy and vibrational sum frequency spectroscopy demonstrate that a lipid monolayer forms on the 3-cyanopropyldimethylchlorosilane modified glass surface with the lipid tails oriented towards the glass.[7] Although analogous microscopy and spectroscopic studies of lipid monolayers have not been repeated on the modified quartz surface, the equivalent contact angles, as well as the similar behaviors of the

GNM and QNM in ion channel measurements, support orientation of the lipid tails towards the quartz surface.

3.3.2 Bilayer Resistance Measurements

Figure 3.2 shows *i-V* curves for a DPhPC bilayer suspended over the orifice of a GNM and QNM (both ~1000-nm-radius) immersed in a 1M KCl, 30 mM Tris, 10 mM EDTA solution. The GNM/QNM was filled with 0.75 μM α–HL, 1.0 M KCl, 30 mM Tris, and 10 mM EDTA (pH 8) and placed in a cell containing the same buffered electrolyte. At room temperature, a voltage sweep was applied between the internal and external Ag/AgCl electrodes. A lipid solution was painted across the orifice and then a pressure of 50-120 mmHg was applied to the internal solution for ion channel reconstitution. Following bilayer formation, the *i-V* curves were recorded over the voltage range -100 to +100 mV at a scan rate of 50 mV/s.

As shown in Figure 3.2, the GNM/DPhPC bilayer structure displayed leakage currents significantly larger than that of the QNM/DPhPC bilayer. We speculated that the lower resistance of the GNM/DPhPC bilayer structure is due to Na^+ transport through the soda lime glass, rather than leakage through the bilayer or the bilayer/substrate seal. To test this hypothesis, we recorded the *i-V* response of GNMs and QNMs immersed to different depths in the aqueous electrolytes. The linear *i-V* response, superimposed on the capacitive charging current, of the GNM/DPhPC bilayer yielded resistances of ~300 and ~120 GΩ for 1 mm and 5 mm submersion depths, respectively. In contrast, the QNM/DPhPC

Figure 3.2. *i-V* curves for a DPhPC bilayer suspended over the orifice of a GNM (~1000-nm-radius) immersed in a 1M KCl, 30 mM Tris, 10 mM EDTA solution to a depth of (A) ~5 mm and (B) ~1mm. *i-V* curves for a suspended bilayer on a QNM (~1000-nm-radius) submerged to (C) ~5 mm, and (D) ~1mm. Scan rate = 50 mV/s.

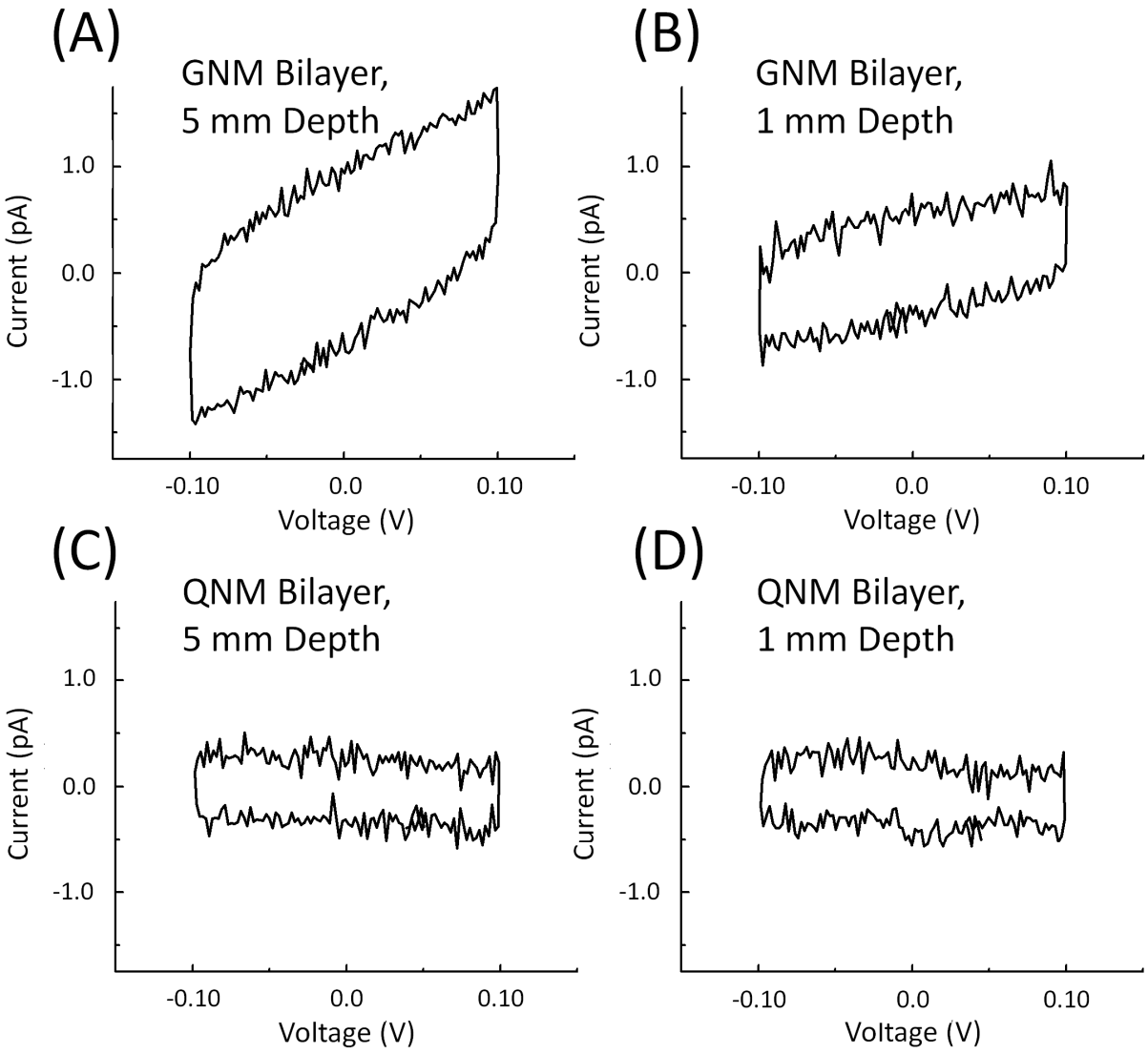
(A)
GNM Bilayer,
5 mm Depth
Current (pA)
1.0
0.0
-1.0
-0.10
0.0
0.10
Voltage (V)
(B)
GNM Bilayer,
1 mm Depth
Current (pA)
1.0
0.0
-1.0
-0.10
0.0
0.10
Voltage (V)
(C)
QNM Bilayer,
5 mm Depth
Current (pA)
1.0
0.0
-1.0
-0.10
0.0
0.10
Voltage (V)
(D)
QNM Bilayer,
1 mm Depth
Current (pA)
1.0
0.0
-1.0
-0.10
0.0
0.10
Voltage (V)

bilayer had measured bilayer resistances greater than or equal to 1 TΩ at both submersion depths.

3.3.3 Solid Support Resistance Measurements

The finding that the ohmic leakage current for the GNM/DPhPC bilayer is dependent upon the depth of immersion suggests that this current is not associated with leakage at the glass/bilayer interface. To further test this conclusion, *sealed* GNM and QNMs, Figure 3.3, were prepared and silanized (i.e., membranes without a nanopore but otherwise identical to the above structures) and their *i*-*V* responses were measured in the 1M KCl, 30 mM Tris, 10 mM EDTA solution. Figure 3.4 shows *i*-*V* responses of the sealed GNM and QNM at immersion depths of 1 and 5 mm. Similar to the GNM and QNM structures with suspended bilayers, the sealed soda lime glass capillary showed a resistance of approximately 290 GΩ at 1 mm submersion and 110 GΩ at 5 mm submersion, while the fused quartz sealed capillary had a resistance greater than or equal to 1 TΩ, independent of immersion depth. (The *i*-*V* response of the sealed QNMs are essentially identical to the open-circuit response, demonstrating the high impedance of the quartz membrane.)

The above results unequivocally demonstrate that electrical conduction within the solid support determines the *apparent* leakage current in the ion channel measurements using GNMs. Specifically, the low resistivity of soda lime glass is responsible for the lower measured resistance of the GNM system. Given that the soda lime glass used in this and previous studies contains 16%

Figure 3.3. Schematic of a sealed soda lime glass or fused quartz capillary functionalized with 3-cyanopropyldimethylchlorosilane, and the apparatus used to determine the resistance of the capillary walls and glass or fused quartz membrane (not to scale).

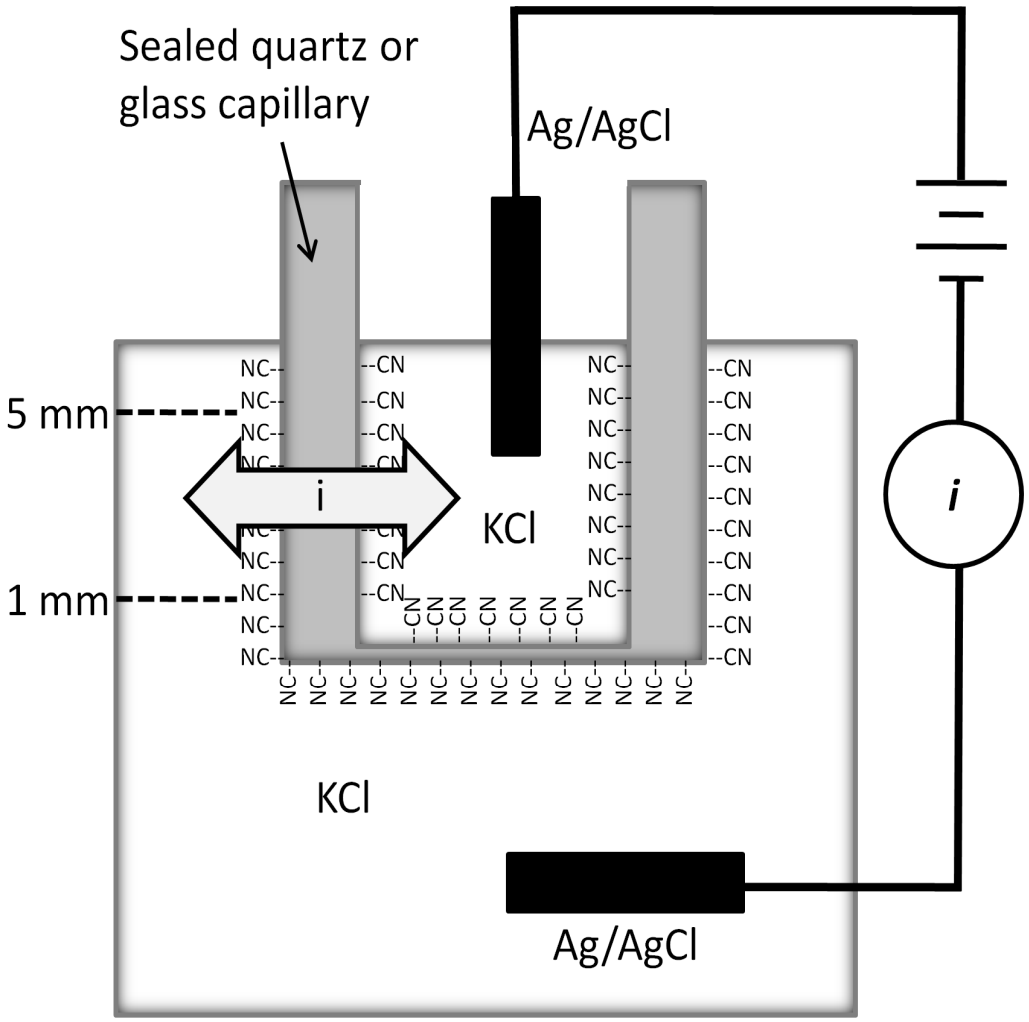
Sealed quartz or
glass capillary
Ag/AgCl
5 mm
1 mm
i
KCl
KCl
Ag/AgCl
i

Figure 3.4. *i-V* curves for a sealed soda lime glass capillary immersed in a 1M KCl, 30 mM Tris, 10 mM EDTA solution to a depth of (A) ~5 mm and (B) ~1 mm. *i-V* curves for a sealed fused quartz capillary submerged to (C) ~1 mm and (D) ~5 mm. Scan rate = 50 mV/s.

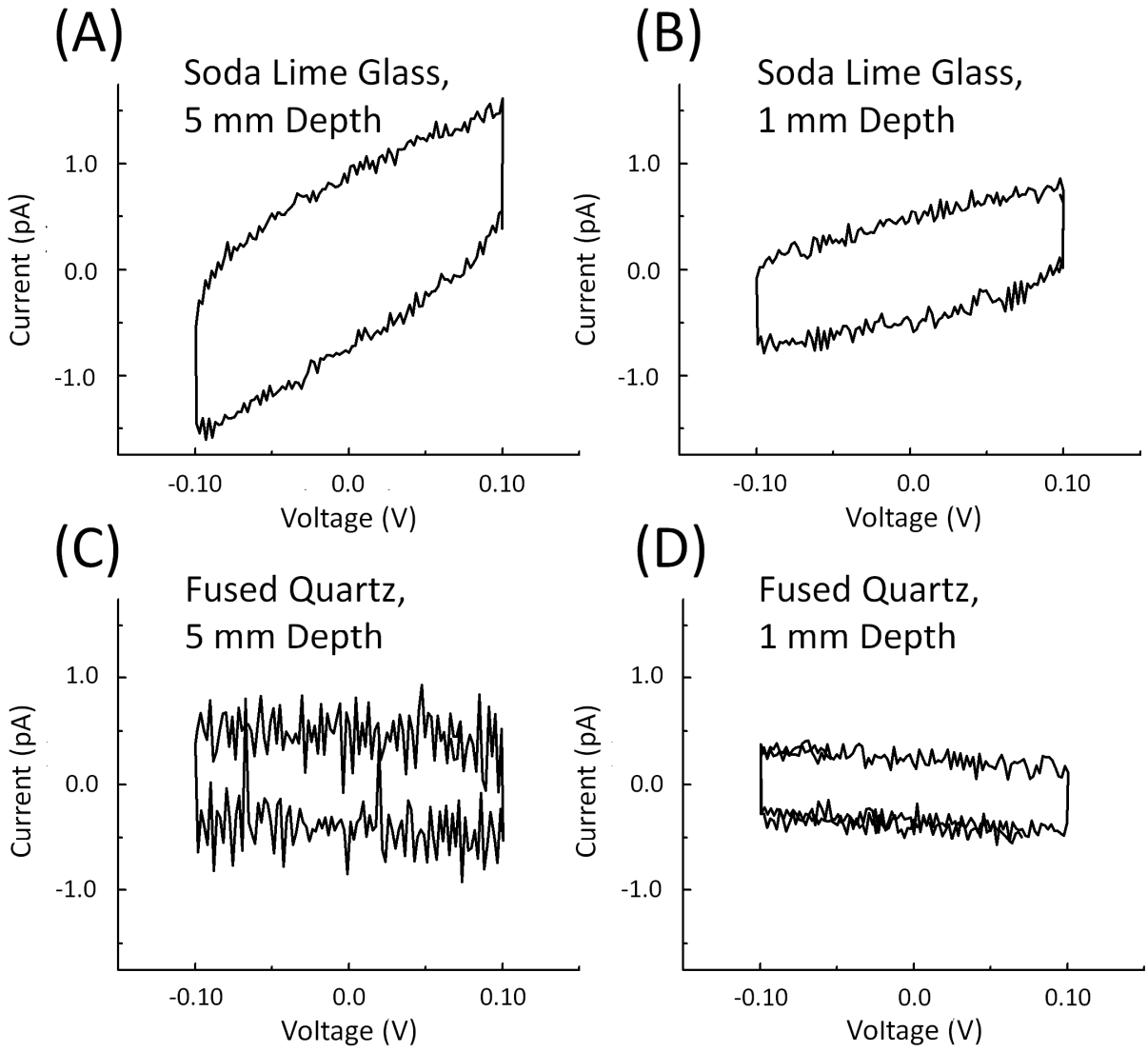
(A)
Soda Lime Glass,
5 mm Depth
(B)
Soda Lime Glass,
1 mm Depth
(C)
Fused Quartz,
5 mm Depth
(D)
Fused Quartz,
1 mm Depth
Current (pA)
1.0
0.0
-1.0
-0.10
0.0
0.10
Voltage (V)

Na_2O, we speculate that this conduction is due to Na^+ hopping in the glass lattice. More interesting, assuming that the area of the bilayer is equal to that of the orifice, the *i-V* measurements employing the QNM demonstrate that the electrical resistance of a ~3 μm^2 DPhPC bilayer is greater than 1 TΩ (a similar value must also exist for the bilayer employing the GNM, as the immersion-depth support resistance is of the order of a few hundred GΩ). We note that the measured seal resistance of the QNM/DPhPC bilayer presented here is significantly larger compared to largest literature values (<200 GΩ) for ion channel measurements in lipid bilayers supported on quartz.[13,14,16,17] We attribute this improvement to the *suspended* bilayer structure on the 3-cyanopropyldimethylchlorosilane modified QNM, as opposed to supported bilayers in previously reported quartz devices.

3.3.4 Bilayer Rupture Voltage Measurements

Voltage induced rupture of the bilayer was found to be ~800 mV at the QNM, similar to that reported for the GNM. The similar values of rupture voltage suggest that the suspended bilayer structure is essentially independent of whether the membrane is made of glass or fused quartz.

3.3.5 Single-Stranded DNA Translocation

Translocation of ssDNA through α–HL reconstituted in the QNM/DPhPC bilayer, schematically shown in Figure 3.5, was performed to demonstrate the

Figure 3.5. Schematic drawing of the translocation of DNA through an α–HL channel reconstituted in a DPhPC bilayer suspended across the orifice of a QNM (not to scale). PyMOL was used to generate the α-HL structure from PDB ID:7αHL.

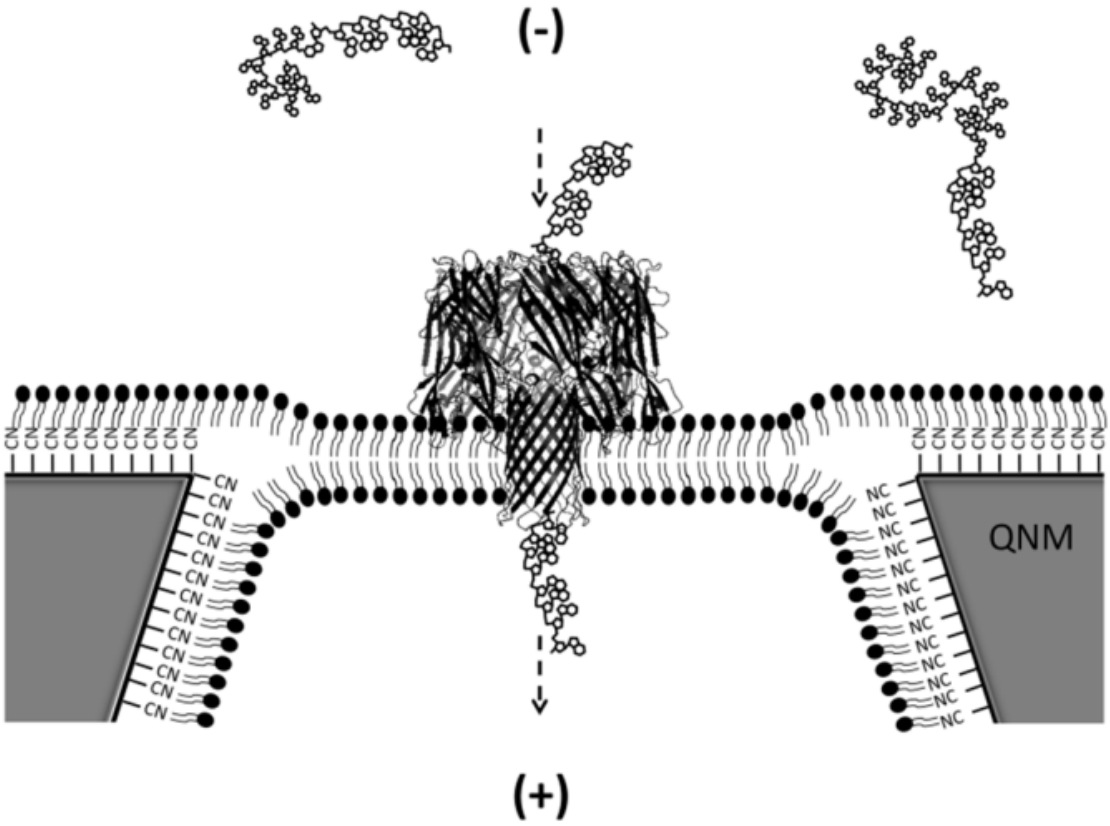
(-)
CN
NC
QNM
(+)

applicability of the QNM for ion channel recordings. A silanized QNM was placed in a solution containing 10 μM ss-DNA (either poly-dA 20-mer or poly-dA 50-mer), 1 M KCl, 25 mM PBS, and 1 M EDTA (pH 7), and, as described above, a DPhPC bilayer was painted while applying a pressure of 60-120 mmHg. The internal solution of the QNM contained only the buffered electrolyte. Figure 3.6 displays 10-s segments of *i-t* traces showing the translocation of poly-dA 20-mer and poly-dA 50-mer using a voltage of 100 mV to electrophoretically drive the oligomers through the ion channel. Observed translocation rates at 100 mV were ~5 and 6 μs/base for the poly-dA 20-mer and poly-dA 50-mer, respectively, in agreement with previously reported values.[28,] Similarly, full current blockades correspond to ~15% of the open channel value, in agreement with translocation of DNA through α–HL. These results demonstrate that QNMs behave nearly identically to GNM in ion channel measurements.

3.3.6 Small Orifice QNMs

While QNMs with pore radii larger than 400 nm are most useful for creating suspended lipid bilayers, it is also possible to fabricate QNMs with much smaller orifices. These smaller nanopore structures are potentially useful in other applications, e,g., detection of nanoparticles. Figure 3.7 shows *i-V* curves for 6, 60, 220, and 370-nm radius QNMs recorded in a 1 M KCl solution. The resistance of a truncated conical-shaped pore comprises the internal resistance of the pore (R_{in}) and the external resistance that spreads radially outward from the pore opening (R_{ex}). For pores with half-cone angles θ less that 20°, and *pore*

Figure 3 6. *i-t* traces corresponding to the translocation of (A) poly-dA 20-mer and (B) poly-dA 50-mer through the α–HL channel. The solution contained 1 M KCl, 25 mM PBS, and 1 M EDTA. The DNA was present on the cis side of the membrane at a concentration of 10 μM. The open channel current is ~110 pA. The upward deflection in current corresponds to the translocation of a single DNA molecule. The inserts show expanded *i-t* traces for single DNA translocation events. Applied voltage = -100 mV, *cis vs. trans*.

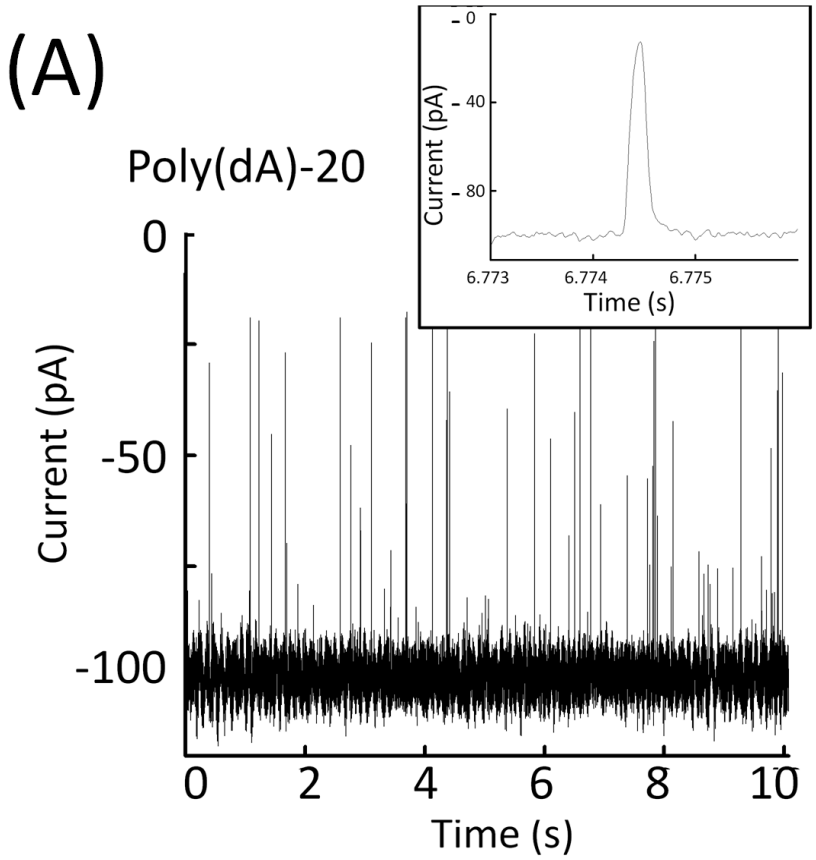
(A)
Poly(dA)-20
Current (pA)
0
-50
-100
0
2
4
6
8
10
Time (s)
Current (pA)
0
40
80
6.773
6.774
6.775
Time (s)

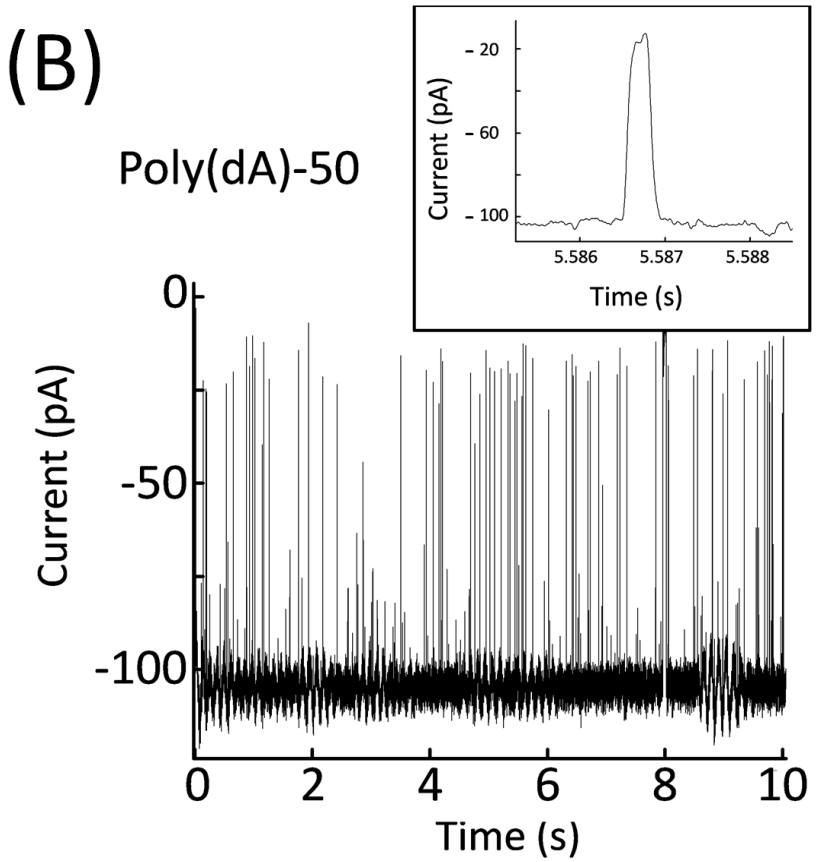
(B)
Poly(dA)-50
Current (pA)
0
-50
-100
0
2
4
6
8
10
Time (s)
Current (pA)
20
60
100
5.586
5.587
5.588
Time (s)

Figure 3.7. *i-V* curves of 6, 60, 220, and 370-nm radius QNMs recorded in a 1 M KCl solution.

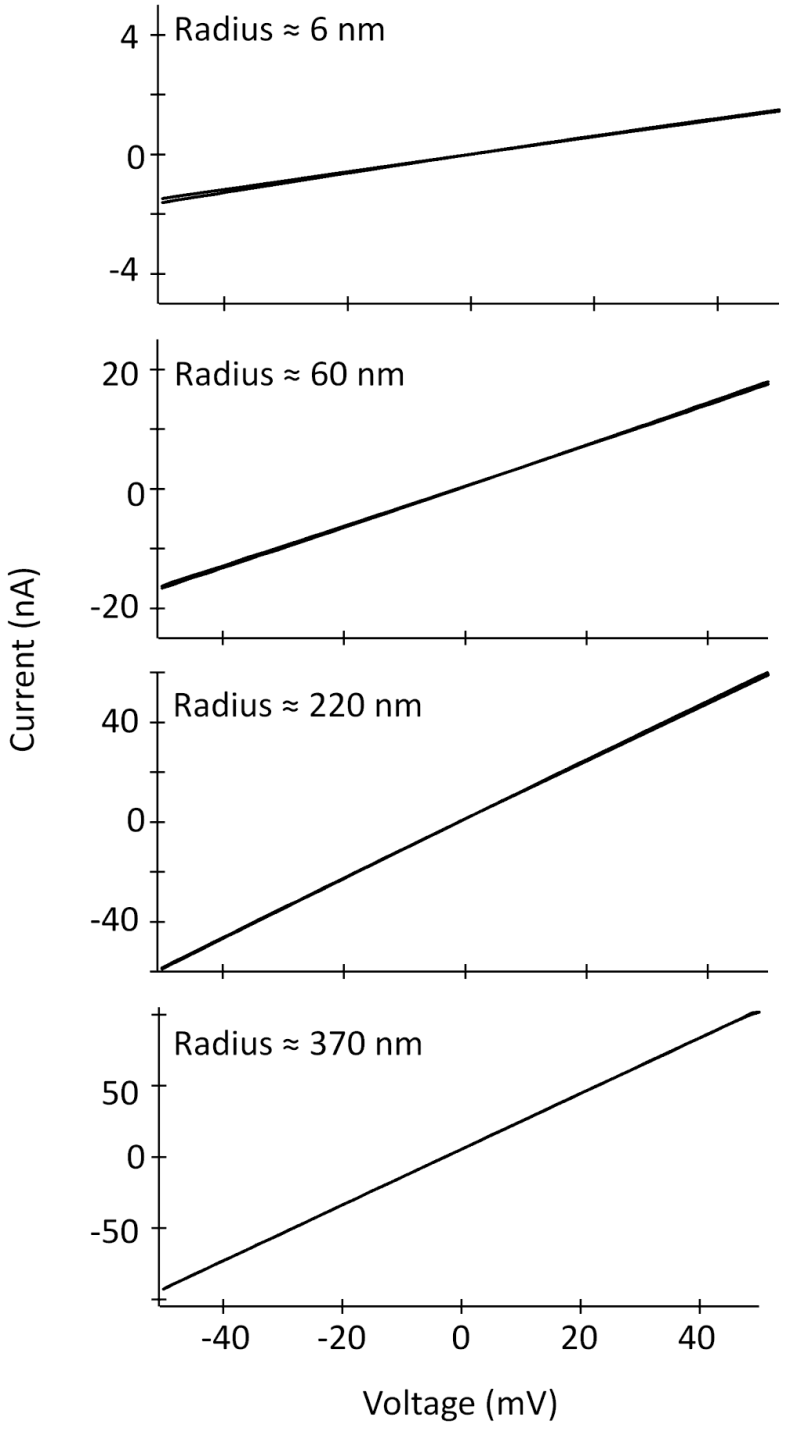
Radius ≈ 6 nm
4
0
-4
Radius ≈ 60 nm
20
0
-20
Radius ≈ 220 nm
40
0
-40
Radius ≈ 370 nm
50
0
-50
Current (nA)
-40
-20
0
20
40
Voltage (mV)

lengths much greater than the orifice radius, the resistance is a function of only r_1 and θ, eq. (3.1).

$$R_p = \frac{1}{\kappa r_1}\left(\frac{1}{\pi \tan\theta} + \frac{1}{4}\right) \tag{3.1}$$

In a 1 M KCl solution (κ_{bulk} = 0.1119 $\Omega^{-1}cm^{-1}$ at 25 ^{o}C)[38] and assuming $\theta \sim 10^{o}$ (estimated by optical microscopy from the shape of the sharpened W wire used to template the pore), eq. (3.1) can be simplified to yield the pore orifice radius r_1 (cm) (with ~10% error) in terms of the measured resistance R_p

$$r_1 = \frac{19}{R_p} \tag{3.2}$$

Eq. (3.2) was used to estimate the pore radii corresponding to the *i-V* curves in Figure 3.7. While there is some uncertainty in these values, the electrical measurements indicate that very small nanopores can be created in quartz membranes.

3.4 Conclusions

We have demonstrated that nanopore membranes with orifice radii as small as 10 nm can be fabricated in 25 to 75 μm-thick fused quartz membranes using a relatively simple bench-top fabrication method. Suspended bilayers can be deposited across the pore orifice and used for ion channel recordings. The

resistance of the quartz/bilayer seals are > 1TΩ for 1000 nm-radius orifice nanopores. This high-resistance seal in combination with the low conductivity of fused quartz results in immeasurably small background currents when using QNMs for ion channel recordings. Additionally, it has been suggested that using a quartz support may improve the signal-to-noise during ion channel recordings due to the low high-frequency capacitance of quartz,[14-17] allowing faster data acquisition rates required in biopolymer translocation analysis and detection of rapid single molecule binding events. Although the 10 kHz filtering of the electrical signal in the current study does not allow high bandwidth analysis, this promising feature of QNMs will be explored in the future.

3.5 References

(1) Terstappen, G.C. *Drug Discovery Today: Technologies* **2005**, *2,* 133-140.

(2) Dabraoski, M.A.; Dekermendjian, K.; Lund, P.-E.; Krupp, J.J.; Sinclair, J.; Larsson, O. *CNS & Neurological Disorders-Drug Targets* **2008**, *7*, 122-128.

(3) Haddock, P. *American Pharmaceutical Review* **2006**, *9*, 119-122.

(4) Landry, Y.; Gies, J.-P. *Fundamental & Clinical Pharmacology* **2008**, *22*, 1-18.

(5) Jean-Yves, Le G.; Olivier, S.; Pierre, B.; Ahmed, A.; Christophe, V. *Recent Patents on Anti-Cancer Drug Discovery* **2007**, *2*, 189-202.

(6) Shim, J.W.; Gu, L.Q. *Anal. Chem.***2007**, *79*, 2207-2213.

(7) White, Ervin, E.N.; Yang, T.; Chen, X.; Daniel, S.; Cremer, P.S.; White, H.S. *J. Am. Chem. Soc.* **2007**, *129*, 11766-11775.

(8) Ervin, E.N.; Kawano, R.; White, R.J.; White, H.S. *Anal. Chem.* **2008**, *80*, 2069–2076.

(9) Ervin, E.N.; White, R.J.; White, H.S. *Anal. Chem.* **2009**, *81*, pp 533–537.

(10) Kawano, R.; Schibel, A. E. P.; Cauley, C. White, H.S. *Langmuir*, **2009**, *25*, 1233–1237.

(11) Lathrop, D. K.; Ervin, E.N.; Barrall, G.A.; Keehan, M.G.; Kawano. R.; Krupka, M.A; White, H.S.; Hibbs, A. H. *J. Am. Chem. Soc.* **2010**, *132* (6), 1878-1885.

(12) Hille, B. *Ionic Channels of Excitable Membranes*; Sinauer Assocates Inc.: Sunderland, 1992.

(13) Procopio, J.; Varanda, W.A.; Fornes, J.A. *Biochimica et Biophysica Acta* **1982**, 688, 808-810.

(14) Fertig, N.; Blick, R.; Behrends, J.C. *Biophysical Journal* **2002**, *82*, 3056-3062.

(15) Fertig, N.; George, M.; Klau, M.; Meyer, C.; Tilke, A.; Sobotta, C.; Blick, R.H.; Behrends, J.C. *Receptors and Channels* **2003**, *9*, 29-40.

(16) Rea, J.L.; Levis, R.A. *Pflügers Archive: European journal of physiology* **1992**, *420*, 618-620.

(17) Levis, R.A.; Rea, J.L. *Biophysical Journal* **1993**, *65*, 1666-1677.

(18) Zhang, B.; Wood, M.; Lee, H. *Anal. Chem.*, in press, **2009**.

(19) In reference 13, only bilayer resistivity values are reported. The seal resistance is computed from the reported orifice diameter.

(20) Fertig, N.; Meyer, Ch.; Blick, R.H.; Trautmann, Ch.; Behrends, J.C. *Physical Review E* **2001**, *64*, 040901 (1-4).

(21) Gu, L.-Q.; Braha, O.; Conlan, S.; Cheley, S.; Baley, H. *Nature* **1999**, *398*, 686-690.

(22) Bayley, H.; Braha, O.; Gu, L.-Q. *Adv. Mater.* **2000**, *12*, 139-142.

(23) Braha, O.; Gu, L.-Q.; Zhou, L.; Xiaofeng, L.; Cheley, S.; Bayley, H. *Nature Biotechnology* **2000**, *18*, 1005-1007.

(24) Deamer, D.; Branton, D. *Acc. Chem. Res*. **2002**, *35*, 817-825

(25) Vercoutere, W.A.; Winters-Hilt, S.; DeGuzman, V.S.; Deamer, D.; Ridino, S.E.; Rodgers, J.T.; Olsen, H.E.; Marziali, A.; Akeson, M. *Nucleic Acids Research* **2003**, *31*, 1311-1318.

(26) DeGuzman, V.S.; Lee, C.C.; Deamer, D.W.; Vercoutere, A. *Nucleic Acids Research* **2006**, *34*, 6425-6437.

(27) Kasianowicz, J.J.; Brandin, E.; Branton, D.; Deamer, D.W. *Proc. Natl. Acad. Sci.* **1996**, *93*, 13770-13773.

(28) Akeson, M.; Branton, D.; Kasianowicz, J.J.; Brandin, E.; Deamer, D.W. *Biophysical Journal* **1999**, *77*, 3227-3233.

(29) Meller, A.; Nivon, L.; Brandin, E.; Golovchenko, J.; Branton, D. *Proc. Natl. Acad. Sci.* **2000**, *97*, 1079-1084

(30) Song, L.; Hobaugh, M.R.; Shustak, C.; Cheley, S.; Bayley, H.; Gouaux, J.E. *Science* **1996**, *274*, 1859-1866

(31) Gouaux, E. *Journal of Structural Biology* **1998**, *121*, 110-122.

(32) Jayasighe, L.; Miles, G.; Bayley, H. *Journal of Biological Chemistry* **2006**, *281*, 2195-2204.

(33) Zhang, B.; Galusha, J.; Shiozawa, P.G.; Wang, G.; Bergren, A.J.; Jones, R.M.; White, R.J.; Ervin, E.N.; Cauley, C.; White, H.S. *Anal. Chem.* **2007**, *79*, 4778–4787.

(34) Alverez, O. How to Set Up a Bilayer System. In *Ion Channel Reconstitution*; Miller, C. Ed.; Plenum Publishing Co.: New York, 1986; pp 115-130.

(35) Bayley, H.; Cremer, P.S. *Nature* **2001**, *413*, 226-230.

(36) White, S. H., The Physical Nature of Planar Bilayer Membranes. in *Ion Channel Reconstitution*; Miller, C.; Plenum Publishing Co.: New York,1986,115-130.

(37) White, R.J.; Zhang, B.; Daniel, S.; Tang, J.M.; Ervin, E. N.; Cremer, P.S.; White, H.S. *Langmuir*, **2006**, *22*, 10777–10783.

(38) (a) Kroner, R. C. *J.AOAC,* **1973**, 56, 295; (b) Pratt, K. W.; Koch, W.f.; Wu, Y.C.; Berezansky *Pure Appl. Chem.,* **2001***, 73,* 1783.

CHAPTER 4

FLUORESCENCE MICROSCOPY OF THE PRESSURE-DEPENDENT STRUCTURE OF LIPID BILAYERS SUSPENDED ACROSS CONICAL NANOPORES

4.1 Introduction

Ion channel recordings have gained much attention in recent years for single-molecule detection, drug screening, and DNA sequencing, in addition to traditional investigations of fundamental biophysical phenomena.[1-15] Consequently, focus has been brought to the development of solid supports for suspended lipid bilayer membranes. In recent reports, we have described the fabrication and application of glass and fused quartz nanopore membranes (GNM and QNM, respectively) for ion channel recordings.[16-21] The GNM/QNM contains a single, conically shaped nanopore embedded within an ~50 μm-thick membrane at the end of a glass or fused quartz capillary. A lipid bilayer can be suspended across the orifice following modification of the glass or quartz surface with 3-cyanopropyldimethylchlorosilane to impart an intermediate hydrophobic surface character. The assumed structure of the lipid bilayer membrane across the nanopore orifice is presented in Figure 4.1A. Suspended lipid bilayers on

GNMs and QNMs display exceptional stability and long lifetimes due to the reduced area of the bilayer (~1 μm^2 for a typical 500 nm-radius nanopore orifice).[20-22] In addition, the reduced bilayer area minimizes the bilayer capacitance which can limit high-frequency data acquisition.

Ion-channel activity using GNMs and QNMS is only observed with the application of a small positive pressure (<100 mmHg) across the membrane, from the nanopore interior relative to the exterior bulk solution, and is observed as a discrete increase in current due to protein reconstitution within the bilayer (α-HL has a conductance of ~1 nS in 1 M KCl[23]). This activity can be reversed by removing the pressure, or by applying a small negative pressure.[20] The pressure controlled channel activity is observed regardless of whether the protein is in the solution inside the capillary or in the external bulk solution, and can be repeatedly turned on and off as the applied pressure is varied between positive and negative pressures, respectively. Figure 4.1B shows an example current-time (*i-t*) trace of α-hemolysin (α–HL) ion channel activity as a function of applied pressure. This unique ability to control ion channel activity indicates a dynamic pressure-dependent bilayer structure. To our knowledge, the nanopore membrane is the only ion channel support for which pressure can be used to reversibly control ion channel activity.

When a solution of lipid molecules dispersed in an organic solvent is spread across a large circular opening (≥ 50 μm-radius) in a hydrophobic solid membrane, e.g., Teflon, that is immersed in an aqueous solution, a lipid bilayer

Figure 4.1. (A) Cross-sectional schematic (not drawn to scale) of an α–HL pore embedded in a bilayer suspended across the orifice of a QNM. (B) Example *i-t* trace showing the pressure-controlled α–HL activity in a solution containing 1 M KCl, 30 mM Tris-HCl, 10 mM EDTA (pH 7.4), and 3 μM α–HL. The step increases in current correspond to individual α–HL pores when a positive applied pressure, +*P*, of 50 mmHg (*internal nanopore solution* vs. *external solution*) is applied across the lipid bilayer; α–HL pore activity disappears when the pressure is either removed or reversed (-*P*). *i-t* data were collected at an applied voltage of 30 mV (*internal* vs. *external*).

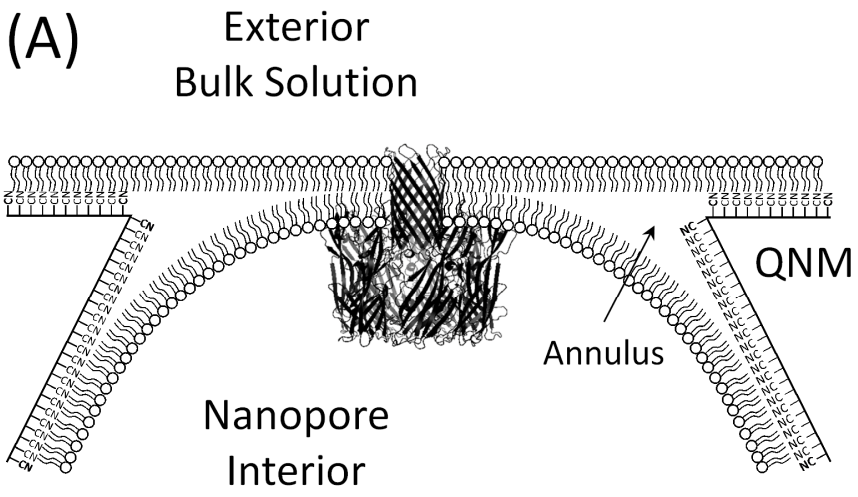
(A)
Exterior
Bulk Solution
QNM
Annulus
Nanopore
Interior

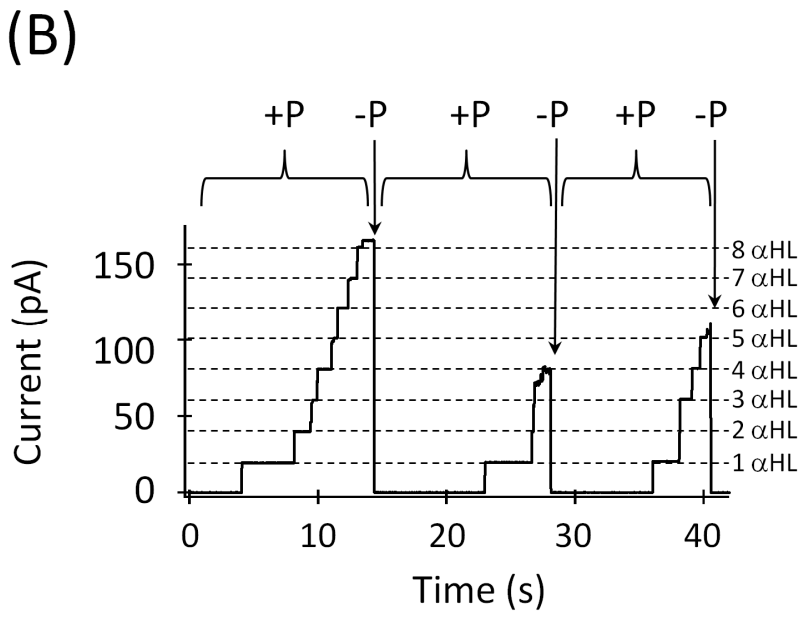
(B)
+P
-P
+P
-P
+P
-P
Current (pA)
150
100
50
0
0
10
20
30
40
Time (s)
8 αHL
7 αHL
6 αHL
5 αHL
4 αHL
3 αHL
2 αHL
1 αHL

will spontaneously form across the opening as a means to reach the lowest free energy state.[24] This suspended bilayer structure is described as possessing a region of bulk lipid solution around the perimeter of the lipid bilayer, adjacent to the walls of the circular opening, which is defined as the annulus, torus, or Plateau-Gibbs border.[25-28] The annulus region contains organic solvent and excess lipid molecules, which are organized into inverse micelles.[28] The bilayer is suspended across the orifice and is connected to the solid support via the annulus. The spontaneous thinning of the lipid solution into a lipid bilayer is due to (i) the curvature-induced pressure driven flow of the bulk lipid solution into the Plateau-Gibbs border, (ii) van der Waals interactions between the aqueous phases separated by the bilayer, and (iii) van der Waals interactions between the hydrocarbon chains of the lipid molecules.[25-28] Additionally, when a voltage is applied across the lipid structure, the electric field aids in thinning.[26-28]

The orifice cross-sectional areas of GNMs and QNMs are ~2 to 3 orders of magnitude smaller than in the traditional devices (Teflon membranes, Delrin cups, etc.) used for investigating the annulus region and mechanism of bilayer thinning. The larger orifices in these polymer membranes will have a smaller volume of lipid solution relative to the orifice dimensions, in comparison with GNM/QNMs; thus, the smaller size of GNM/QNMs may inhibit the lipid solution from spontaneously thinning across the orifice. If the lipid solution does not thin into a bilayer, ion channel reconstitution or activity will not occur. We observe that an external pressure force is required for observing ion channel activity using

GNM/QNMs, suggesting a fundamental difference in the bilayer structure suspended across large and small orifices.

Fluorescence imaging has been shown to be useful in characterizing the nature of artificial bilayers,[29-31] and imaging techniques have previously been successfully combined with electrical recordings to simultaneously monitor ion channel activity.[32-34] Here, epi-illumination fluorescence microscopy is used to observe the structure of lipid bilayers suspended across the orifice of a QNM, as a function of applied pressure. Nile red fluorescent dye is dissolved in the lipid solution (1,2-diphytanoyl-*sn*-glycero-3-phosphocholine in decane) used to form a bilayer. The resulting bilayer is imaged as a function of applied pressure while simultaneously recording the α-HL ion channel activity. To avoid fluorescent artifacts from the glass in GNMs, nanopore membranes prepared from fused quartz capillaries are used. QNMs possess similar surface properties and ion channel reconstitution capabilities as GNMs, in addition to improved electrical and optical properties.[21,35] It is found that the bilayer structure and lipid solution distribution at conical-shaped pores varies as a function of pressure. A thinning and protrusion of the bilayer (which allows for ion channel reconstitution) occurs with positive pressure, and a withdrawal of the lipid solution into the pore occurs with negative pressure. The fluorescence images are consistent with the dependence of ion channel activity on applied pressure.

4.2 Experimental Section

4.2.1 Chemicals and Materials

Aqueous solutions were prepared using 18 MΩ·cm water obtained from a Barnstead E-pure water purifier. KCl, K_2HPO_4, KH_2PO_4, and EDTA were used as received from Mallinckrodt to prepare buffered electrolyte solutions (containing either 1 M KCl, 10 mM PBS, and 1 mM EDTA (pH 7.4), or 1 M KCl, 30 mM Tris-HCl, and 10 mM EDTA (pH 7.4)). 3-cyanopropyldimethylchlorosilane was used as received from Gelest. Decane was obtained from Fisher Scientific and 1,2-diphytanoyl-*sn*-glycero-3-phosphocholine (DPhPC) was obtained from Avanti Polar Lipids in 10 mg aliquots dispersed in chloroform. Nile red dye was purchased from Invitrogen (Cat. No. N-1142) as a powder and dispersed in chloroform (spectroscopy/LC grade, from Omnisolve) and stored at -4° C at a concentration 0.5 mg per mL when not in use. α–HL monomer was obtained from Sigma-Aldrich as a lyophilized powder and stored at 0.6 mg per mL H_2O in a -80° C freezer, and diluted to ~240 nM with buffered electrolyte upon thawing. α-HL solutions were stored in the refrigerator (4 °C) for short periods of time between experiments. Glass coverslides (No. 1, 22 x 22 mm) were obtained from VWR and used to form the base of a well when attached to a glass cylinder via epoxy. This well was used as the experimental cell for simultaneously recording ion channel activity and fluorescence images. Ag wire for Ag/AgCl electrodes was purchased from Alpha Aesar (0.25 mm and 0.5 mm diameter).

4.2.2 QNM Fabrication

The fabrication of the QNM has been previously reported,[21] and is only briefly described here. A 50-μm-radius tungsten (W) wire is attached to a W rod via silver conductive adhesive paste; the end of the wire is then electrochemically sharpened in 1.5 M NaOH while applying 10 V_{PP} at 60 Hz. The nanopore membrane is formed by initially sealing the end of a 3-4 cm length of fused quartz capillary with a H_2/O_2 flame. Once the fused quartz membrane is formed, the sharpened W wire is inserted into the capillary and positioned within 15 μm of the membrane. The quartz is then heated again in the H_2/O_2 flame while applying a vacuum to the end of the capillary, collapsing the fused quartz membrane until the W wire is sealed into the membrane. The sealed end of the capillary is polished, leaving a thin fused quartz membrane (25-75 μM thick) in which a W disk is exposed. Finally, the W wire is partially etched out of the orifice in a 1.5 M NaOH solution by applying 10 V_{PP} at 60 Hz; the remaining wire is manually removed by pulling the W rod out of the capillary. The approximate size of the W disk is monitored during polishing with an electrical feedback circuit which indicates when the desired radius has been reached. The radius of the nanopore orifice is determined from the measured conductance in 1 M KCl.[18-20] The fused quartz surface is chemically modified with 3-cyanopropyldimethyl-chlorosilane in order to create the hydrophobic surface character required for formation of the suspended bilayer structure.[19,20]

4.2.3 Electrical Measurements

The QNM was filled with buffered electrolyte containing 240 nM α–HL and submerged in a cell containing the same electrolyte (without α–HL). Ag/AgCl electrodes (fabricated by immersing a Ag wire in Clorox bleach for 10 min) were used to apply a voltage bias (+40 mV, *internal* vs. *external*) across the QNM. One Ag/AgCl electrode (0.25 mm diameter) was placed inside the QNM capillary and the second (0.5 mm diameter) was placed in the external cell. The back of the QNM was sealed with a Dagan Corporation pipette holder attached to a pressure line and syringe; positive and negative pressures were applied by compression and release of the syringe plunger, respectively, and measured using a sphygmomanometer pressure gauge. A voltage was applied across the GNM with a Dagan Corporation CHEM-CLMAP (Voltammeter and Amperometer Voltage Clamp Amplifier) interfaced with a PC and the current was monitored.

4.2.4 Bilayer Formation

To prepare the lipid for bilayer formation, a nitrogen stream was used to dry the chloroform from the DPhPC solution and the lipid was re-dispersed in 1 mL decane. Nile red dye was then added to the lipid solution at a concentration of 0.001% (by mass) in 10 mg DPhPC per mL decane. The 0.001% Nile red lipid solution was painted across the QNM orifice with a pipette tip while an *i-t* trace was recorded. A decrease in conductance to ~10 pS (corresponding to an ~100 GΩ bilayer seal) indicates that a bilayer has formed.[20] Positive pressure was applied to the back of the QNM until α–HL insertion was observed and then

negative pressure was used to remove the α–HL activity. While monitoring α–HL activity through the *i-t* trace, fluorescence microscopy was used to image the bilayer as a function of applied pressure. Protein channel activity was used to verify the presence of a functional bilayer; only bilayers that exhibited protein channel conductance were imaged. Figure 4.2 shows a depiction of the experimental setup.

4.2.5 Fluorescence Microscopy and Pressure Dependent α-Hemolysin Ion Channel Reconstitution

Fluorescence images of the bilayer suspended across the QNM were captured with an inverted epi-illumination fluorescence microscope. The beam from a Lexel Model 95 argon ion laser, tuned to 488-nm, was passed through a Pellin-Broca prism, and selectively blocked with an electronic Uniblitz shutter to minimize sample photobleaching. The beam was scattered with a rotating, roughened glass disc to average the illumination speckle pattern. A 55-mm focal length lens (f/1.2) was used to reimage the scattered laser spot through the objective. A band-pass excitation filter (D480/30, Chroma) and a long-pass dichroic beam splitter (505dclp, Chroma) were placed before the objective (Nikon Plan Fluor 100x, 1.3 NA). The fluorescence emitted from the sample was collected by the same objective and separated from the excitation light via the dichroic beam splitter and a 510-nm long pass emission filter (HQ510lp, Chroma); the depth of field was 1 μm. The fluorescence image was acquired with

Figure 4.2. Schematic depiction of the experimental system for measuring the fluorescence intensity from the QNM suspended bilayer as a function of applied pressure, while simultaneously performing ion channel recordings. The QNM with a suspended DPhPC bilayer is submerged in a cell positioned on the stage of an inverted epi-illumination fluorescence microscope, while *i-t* data are simultaneously recorded in a solution containing 1 M KCl, 10 mM PBS, 1 mM EDTA (pH 7.4). The internal volume of the QNM capillary contained 240 nM α-HL dissolved in the same solution, and is connected to a gas-tight syringe for pressure control. The QNM surface is moved in the +/- *z* direction relative to the microscope objective by moving the optical stage. In the experiments described below, z = 0 corresponds to the QNM exterior surface being located at the microscope focal point, while positions below (nanopore interior) and above (exterior bulk solution) the QNM surface are indicated as -*z* and +*z*, respectively.

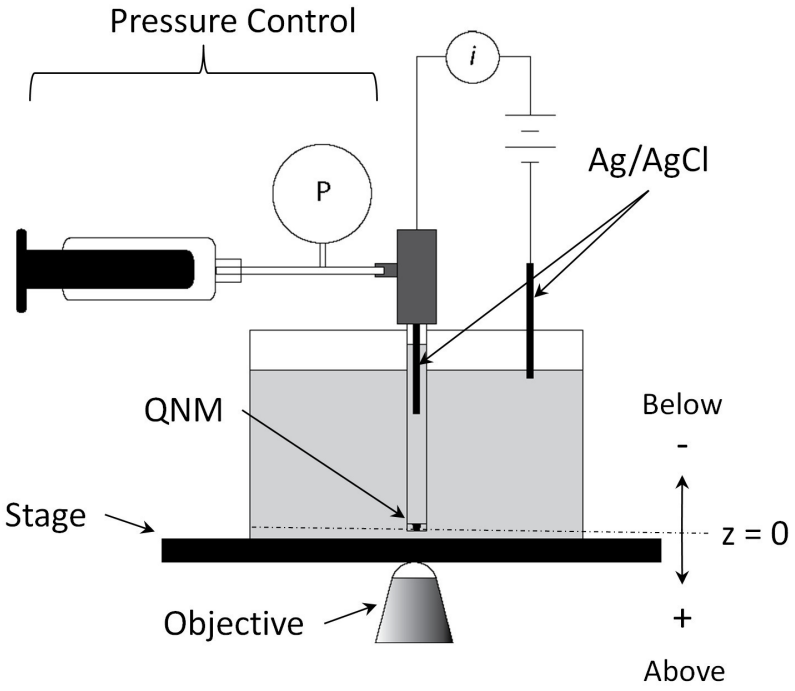
Pressure Control
i
P
Ag/AgCl
QNM
Below
-
Stage
z = 0
Objective
+
Above

a Photometrics CoolSNAP HQ CCD detector (1392 x 1040 imaging array with 6.45 x 6.45 μm pixels).

Once a bilayer was formed, the position of the QNM was adjusted above the microscope stage using a micro-positioner to bring the QNM surface into the focus of the objective. Images were captured with the focus of the objective at varying depths, as indicated in Figure 4.2: (i) at the external QNM surface (z = 0), (ii) above the external surface (+z) into the bulk solution, and (iii) below the external surface (-z) into the nanopore interior. The objective was adjusted in the z-direction by +/- 2 μm increments to image the Nile red distribution as a function of applied pressure. Each fluorescence image was acquired at a 1.0 s integration time.

4.3 Results and Discussion

4.3.1 Bilayer Fluorescence as a Function of Applied Pressure

Nile red is a hydrophobic dye and when dissolved in a hydrophobic environment[36,37] such as the acyl chain region of a lipid membrane,[38,39] or the decane/lipid solution, its fluorescent emission is readily detectable. Nile red is very sensitive to the hydrophobicity of its environment,[40-42] it fluoresces strongly in a lipid/decane solution, and is weakly emitting when dissolved in aqueous solution.[43] Thus, the fluorescence signal from the Nile red was used to image the distribution of the lipid/decane membrane at the QNM surface as a function of the applied pressure. Line scans of fluorescence intensity over the pore face and nanopore orifice were plotted to quantitatively assess the pressure-dependent

bilayer structure. In these experiments, QNMs with orifice radii (1.5-2 μm) slightly larger than those previously employed in ion channel recordings (0.5-1 μm) were used in order to observe structural features in the fluorescence images. The pressure-dependent activity of α-HL with these larger QNMs, however, is qualitatively similar to that previously reported.[20]

Figure 4.3 demonstrates how the fluorescence intensity varies across the QNM surface as a function of applied pressure. In this experiment, the QNM surface is brought into the focal plane of the microscope (z = 0), and a positive pressure (80 mmHg) is applied across the membrane (internal vs. external solution). Beginning at ~600 s in the *i-t* trace, an α-HL channel is reconstituted in the bilayer, yielding a conductance of ~1 nS (40 pA at V_{app} = 40 mV) in agreement with literature values in 1.0 M KCl.[22] The *i-t* traces were recorded with an open cell, without a Faraday cage, in order to simultaneously record the fluorescence images, resulting in electrical noise larger than usually present in the α-HL channel recordings using glass nanopores.[22]

The fluorescence image obtained at positive pressure showed a decrease of fluorescence intensity over the pore orifice. Application of a negative pressure resulted in the immediate loss of α-HL activity, and an increase in the fluorescence intensity across the pore orifice (relative to positive pressure). Upon bilayer rupture at a higher pressure (>100 mmHg), the fluorescence intensity decreases across the nanopore membrane surface. Although the absolute fluorescence intensity and background signal vary using different QNMs and bilayers, the relative change in fluorescence intensity over the pore orifice as

Figure 4.3. (A) *i-t* trace showing the reconstitution of a single αHL channel in a DPhPC bilayer suspended across the ~2 μm-radius orifice of a QNM. The solution conditions are the same as in Figure 4.2, and the *i-t* trace was obtained at a voltage of 40 mV. +*P* corresponds to +80 mmHg (internal vs. external solution), while -*P* corresponds to -20 mmHg. The bilayer was ruptured by applying 120 mmHg. (B) Fluorescence images and intensity line scans of the QNM/DPhPC bilayer were taken at ~650 s (+*P*), ~690 s (-*P*), and ~1130 s (bilayer rupture) during the ion channel recording. The dashed horizontal lines correspond approximately to the orifice circumference, with the center of the orifice located at ~36 μm.

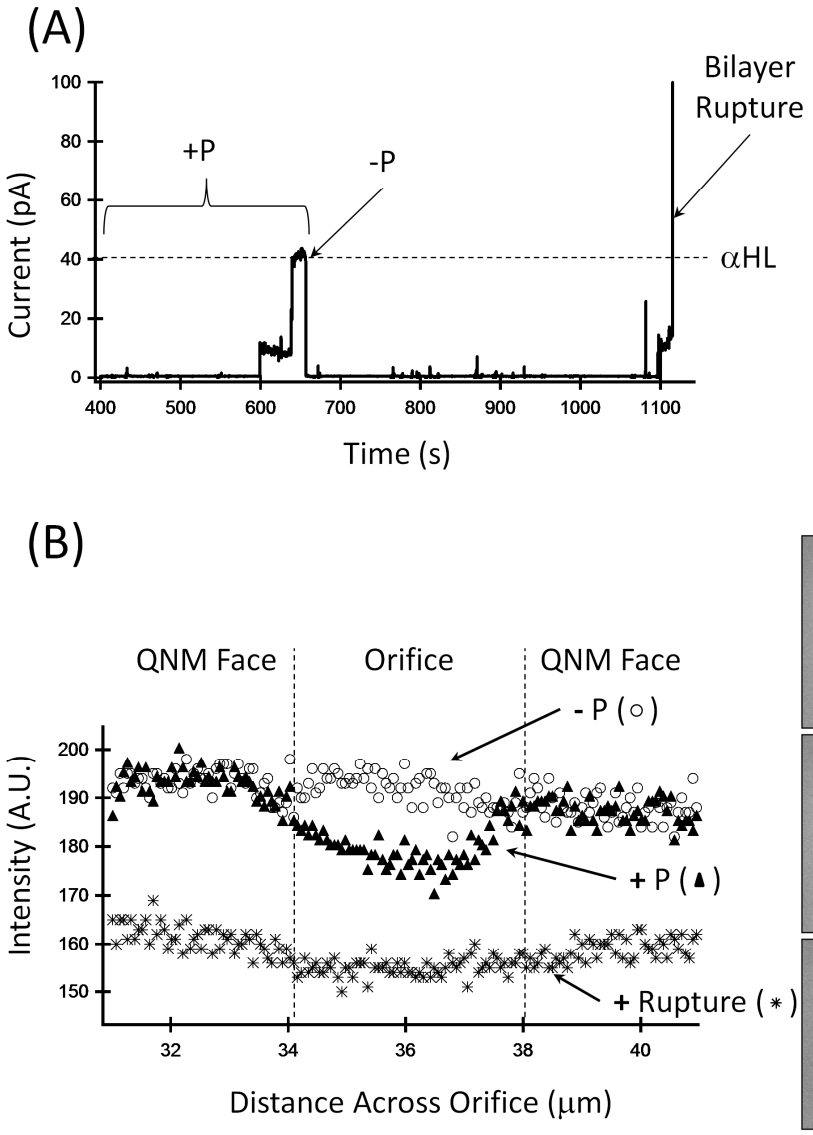
(A)
Bilayer
Rupture
+P
-P
αHL
Current (pA)
Time (s)
(B)
QNM Face
Orifice
QNM Face
- P (○)
+ P (▲)
+ Rupture (∗)
Intensity (A.U.)
Distance Across Orifice (μm)
3 μm
-P
+P
Rupture

a function of applied pressure is reproducible. A positive pressure applied from the internal solution results in a decrease in fluorescence intensity across the pore orifice, where the lipid bilayer is located.

4.3.2 Bilayer Fluorescence as a Function of Applied Pressure and Objective Focus Depth

Pressure dependent changes in the fluorescence intensity across the pore orifice were investigated as a function of the objective focus depth, Figure 4.4. Upon protein channel insertion with positive pressure, fluorescent images were acquired above the external surface ($z>0$, see Figure 4.2), at the external pore surface ($z=0$), and below the external surface ($z<0$). A negative pressure was applied and images were again recorded above the external surface, at the external pore surface, and below the external surface. Acquisition of the images was repeated again once the bilayer was ruptured. Fluorescence images are shown in Figure 4.4A as a function of the objective focus depth (at $z=+4$, 0, or -4), while Figure 4.4B plots the line scans of the fluorescence intensity over the pore face as a function of the objective focus depth ($z=+6$ to $z=-6$), and finally Figure 4.4C illustrates the lipid/decane structure as interpreted from the results presented in Figure 4.4A and 4.4B.

Figure 4.4A (left) and Figure 4.4B (left) summarize the results of a series of fluorescence imaging for 60 mmHg applied pressure (nanopore interior relative to the exterior bulk solution). The fluorescent images (Figure 4.4A) and line

Figure 4.4. (A) Fluorescent images of QNM DPhPC bilayer with the microscope objective focus above the external QNM external surface (z = +4 μm), at the external surface (z = 0), and below the external surface (z = -4 μm) as a function of pressure left to right: +P (+60 mmHg), -P (-20 mmHg), and after bilayer rupture. (B) Fluorescent intensity line scans recorded for +6 < z < -6 μm at 2 μm increments at +60 and -20 mmHg, and after bilayer rupture. (C) Schematic representation of the bilayer structure as interpreted from the fluorescent microscopy data.

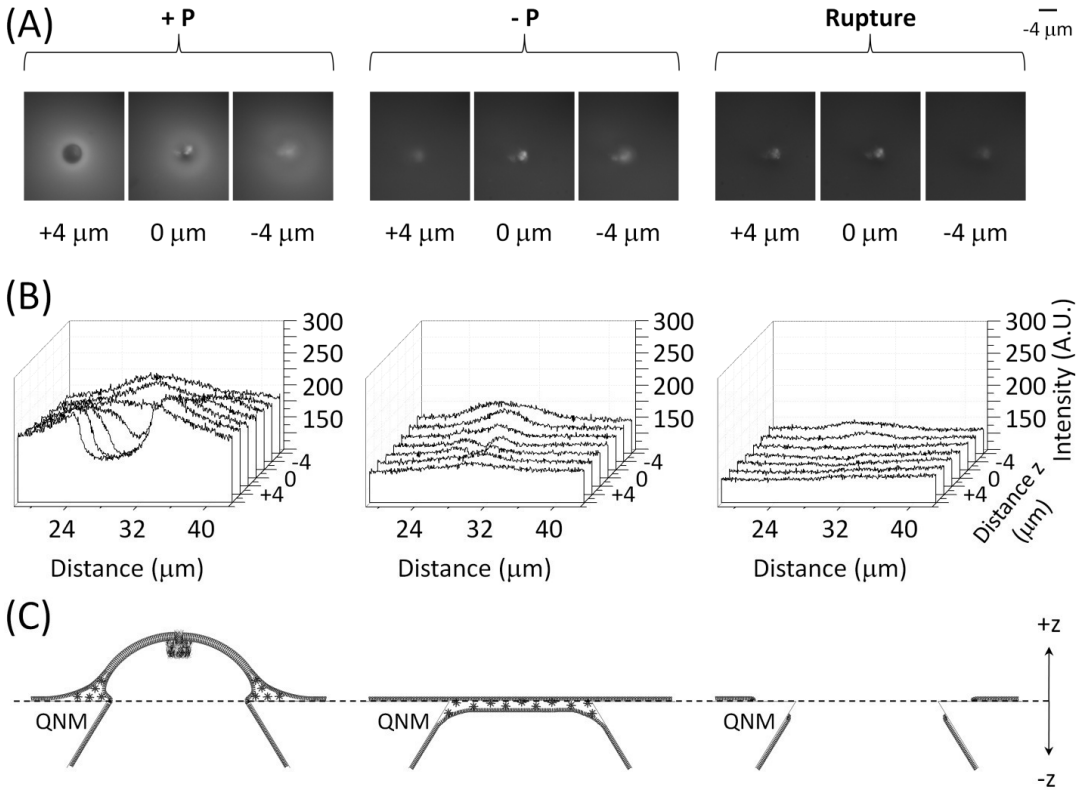
(A)
+ P
- P
Rupture
-4 µm
+4 µm
0 µm
-4 µm
+4 µm
0 µm
-4 µm
+4 µm
0 µm
-4 µm
(B)
300
250
200
150
Intensity (A.U.)
-4
0
+4
Distance z (µm)
24
32
40
Distance (µm)
Distance (µm)
Distance (µm)
(C)
+z
-z
QNM
QNM
QNM

scans (Figure 4.4B) show the lipid distribution from -6 μm below the external surface, at the pore face (0 μm), to +6 μm above the external surface. At the pore surface (0 μm), there is a decrease in fluorescence intensity across the orifice and on the surface around the orifice. Above the external surface (+4 μm) there is a ring of fluorescence brighter than the QNM orifice, and a decrease in fluorescence within the center. This configuration corresponds to conditions favorable for α–HL reconstitution, and suggests a structure where the lipid solution is forced outside of and away from the orifice, resulting in a convex bilayer structure; the lipid/decane membrane has thinned to where it can be spanned by an α-HL channel (Figure 4.4C, left). This hypothesis is further supported by previous observations that a pressure gradient induces curvature to the bilayer.[44-46] Images obtained below the external surface (-4 μm) show that there is fluorescence concentrated across the orifice; this is attributed to lipid and decane collecting within the orifice and scattered fluorescence from the pore walls.

Figure 4.4A (center) and Figure 4.4B (center) summarize the results at a negative applied pressure at various objective focus depths. When negative pressure is applied to the QNM, the fluorescence intensity decreases across the surface of the pore, and increases across the pore orifice relative to the surrounding surface. This is the case for both above the external surface (up to +6 μm) and at the pore surface (0 μm); again, the fluorescence observed when the focus of the objective is below the external surface (up to -6 μm) is postulated to be lipid and decane within the orifice and scattered fluorescence from the pore

walls. The microscope objective has a depth of field of ~1 μm and will collect out of focus fluorescence as well. However, the increase in fluorescence intensity across the pore orifice relative to the pore surface can be compared with images obtained at positive pressure where the intensity on the surface is greater than that across the orifice. The fluorescence distribution upon applying negative pressure suggests that dye (and thus lipid and decane) is accumulating within the orifice. These results are interpreted as the lipid/decane solution being pulled into the pore and thickening of the solution layer across the orifice as the bilayer leaflets are separated (Figure 4.4C, center). This conclusion is consistent with the observation that smaller orifice dimensions (<70 μm) are prohibitive to spontaneous thinning of the lipid/solvent solution across the orifice.[47] Negative or zero pressure allows the lipid and decane to distribute within the pore and along the capillary walls, whereas positive pressure forces the lipid out from the pore, thinning the solution to the limit of a functional lipid bilayer.

Finally, Figure 4.4A (right) and 4B (right) summarize the fluorescence data following the rupture of the bilayer at high pressure. When the bilayer is ruptured, there is a decrease in fluorescence over the surface and within the pore as seen from the intensity decrease compared with the positive and negative pressure images and line scans. These results are interpreted as an irreversible loss of the lipid and dye from the orifice region (Figure 4.4C, right).

4.4 Conclusions

Fluorescence microscopy images obtained during ion channel recordings indicate that applying a positive pressure across the QNM results in a redistribution of the decane/lipid solution favorable for bilayer formation and ion channel activity. The fluorescence images suggest that positive pressures push the decane/lipid solution outward from the orifice (towards the external solution) creating a convex lipid bilayer structure suitable for ion channel reconstitution. Removal of this positive pressure (either zero or negative applied pressure) results in loss of ion channel activity, a consequence of the decane/lipid solution being drawn into the orifice, as indicated by the increased fluorescence in the orifice region. Most likely, this flow results from surface tension pulling the decane/lipid solution into the pore. The loss of ion channel activity after removal of the external positive pressure suggests that the lipid bilayer structure is unstable as the decane/lipid solution is drawn through the orifice of the pore.

4.5 References

(1) Terstappen, G.C. *Drug Discov. Today* **2005**, *2,* 133-140.

(2) Dabraoski, M.A.; Dekermendjian, K.; Lund, P.-E.; Krupp, J.J.; Sinclair, J.; Larsson, O. *CNS Neurol. Disord.: Drug Targets* **2008**, *7*, 122-128.

(3) Haddock, P. *American Pharmaceutical Review* **2006**, *9*, 119-122.

(4) Landry, Y.; Gies, J.-P. *Fundam. Clin. Pharmacol.* **2008**, *22*, 1-18.

(5) Jean-Yves, Le G.; Olivier, S.; Pierre, B.; Ahmed, A.; Christophe, V. *Recent Pat. Anti-Cancer Drug Discovery* **2007**, *2*, 189-202.

(6) Shim, J.W.; Gu, L.Q. *Anal. Chem.* **2007**, *79*, 2207-2213.

(7) Gu, L.-Q.; Braha, O.; Conlan, S.; Cheley, S.; Baley, H. *Nature* **1999**, *398*, 686-690.

(8) Bayley, H.; Braha, O.; Gu, L.-Q. *Adv. Mater.* **2000**, *12*, 139-142.

(9) Braha, O.; Gu, L.-Q.; Zhou, L.; Xiaofeng, L.; Cheley, S.; Bayley, H. *Nat. Biotechnol.* **2000**, *18*, 1005-1007.

(10) Deamer, D.; Branton, D. *Acc. Chem. Res*. **2002**, *35*, 817-825.

(11) Vercoutere, W.A.; Winters-Hilt, S.; DeGuzman, V.S.; Deamer, D.; Ridino, S.E.; Rodgers, J.T.; Olsen, H.E.; Marziali, A.; Akeson, M. *Nucleic Acids Res.* **2003**, *31*, 1311-1318.

(12) DeGuzman, V.S.; Lee, C.C.; Deamer, D.W.; Vercoutere, A. *Nucleic Acids Res.* **2006**, *34*, 6425-6437.

(13) Kasianowicz, J.J.; Brandin, E.; Branton, D.; Deamer, D.W. *Proc. Natl. Acad. Sci.* **1996**, *93*, 13770-13773.

(14) Akeson, M.; Branton, D.; Kasianowicz, J.J.; Brandin, E.; Deamer, D.W. *Biophys. J.* **1999**, *77*, 3227-3233.

(15) Meller, A.; Nivon, L.; Brandin, E.; Golovchenko, J.; Branton, D. *Proc. Natl. Acad. Sci.* **2000**, *97*, 1079-1084.

(16) Zhang, B.; Zhang, Y.; White, H.S. *Anal. Chem.* **2004**, *76*, 6229-6238.

(17) Zhang, B.; Zhang, Y.; White, H.S. *Anal. Chem.* **2006**, *78*, 477-483.

(18) Zhang, B., Galusha, J.; Shiozawa, P.G.; Wang, G.; Bergren, A.J.; Jones, R.M.; White, R.J.; Ervin, E.N.; Cauley, C.C.; White, H.S. *Anal. Chem.* **2007**, *79*, 4778-4787.

(19) White, R.J.; Zhang, B.; Daniel, S.; Tang, J.M.; Ervin, E.N.; Cremer, P.S.; White, H.S. *Langmuir* **2006**, *22*, 10777-10783.

(20) White, R.J.; Ervin, E.N.; Yang, T.; Chen, X.; Daniel, S.; Cremer, P.S.; White, H.S. *J. Am. Chem. Soc.* **2007**, *129*, 11766-11775.

(21) Schibel, A. E. P.; Edwards, T.; Kawano, R., Lan, W.; White, H. S. *Anal. Chem.* **2010**, *82*, 7259-7266.

(22) (a) Kawano, R.; Schibel, A. E. P.; Cauley, C.; White, H. S. *Langmuir* **2008**, *25*, 2850-2855. (b) Ervin, E. N.; Kawano, R.; White, R. J.; White, H. S. *Anal. Chem.* **2008**, *80*, 2069-2076. (c) Ervin, E. N.; Kawano, R.; White, R. J.; White, H. S. *Anal. Chem.* **2008**, *81*, 533-537. (d) Lathrop, D. K.; Ervin,

E. N.; Barrall, G. A.; Keehan, M. G.; Kawano, R.; Krupka, M. A.; White, H. S.; Hibbs, A. H. *J. Am. Chem. Soc.* **2010**, *132*, 1878-1885. (e) Schibel, A. E. P.; An, N.; Jin, Q.; Fleming, A. M.; Burrows, C. J.; White, H. S. *J. Am. Chem. Soc.* **2010**, *132*, 17992-17995. (f) Chen, Q. Liu, J.; Schibel, A. E. P.; White, H. S.; Wu, C. *Macromolecules* **2010**, *43*, 10594-10599.

(23) Bayley, H.; Cremer, P.S. *Nature* **2001**, *413*, 226-230.

(24) Mueller, P.; Rudin, D.O.; Tien, H.T.; Wescott, W.C. *J. Phys. Chem.* **1963**, *67*, 534-535.

(25) Tien, H.T.; Diana, A. L. *Chem. Phys. Lipids* **1968**, *2*, 55-101.

(26) White, S. H. *Biophys. J.* **1970**, 10, 1127-1148.

(27) White, S. H. *Biophys. J.* **1972**, *12*, 432-445.

(28) White, S. H. The Physical Nature of Planar Bilayer Membranes. In *Ion Channel Reconstitution*; Miller, C. Ed.; Penum Publishing Co.: New York, 1986, pp 3-35.

(29) Thompson, N. L.; Plamer, A. G., III; Wright, L. L.; Scarborough, P. E. *Comments Mol. Cell Biol.*, **1988**, *5*, 109-131.

(30) Korlach, J.; Schwille, P.; Webb, W. W.; Feigenson, G. W. *Proc. Natl. Acad. Sci. USA* **1999**, *96*, 8461-8466.

(31) Samsonov, A. V.; Mihalyov, I.; Cohen, F. S. *Biophys. J.* **2001**, *81*, 1466-1500.

(32) Ide, T.; Yanagida, T. *Biochem. Biophys. Res. Commun.* **1999**, *265*, 595-599.

(33) Ries, R. S.; Choi, H.; Blunck, R.; Bezanilla, F.; Heath, J. R. *J. Phys. Chem. B* **2004**, *108*, 16040-16049.

(34) Suzuki, H.; Tabata, K. V.; Noji, H.; Takeuchi, S. *Langmuir*, **2006**, *22*, 1937-1942.

(35) Sakmann B. and Neher, E., Ed. *Single-Channel Recording*; Plenum Press: New York, 1983.

(36) Hou, Y.; Bardo, A. M.; Martinez, C.; Higgins, D. A. *J. Phys. Chem. B* **2000**, *104*, 212-219.

(37) Martin-Brown, S. A.; Fu, Y.; Saroja, G.; Collinson, M. M.; Higgins, D. A. *Anal. Chem.* **2005**, *77*, 486-494.

(38) Krishnamoorthy, I.; Krishnamoorthy, G. *Biochim. Biophys. Acta* **1998**, *1414*, 255-259.

(39) Gao, G.; Mei, E.; Lim, M.; Hochstrasser, R. M. *J. Am. Chem. Soc.* **2006**, *128*, 4814-4822.

(40) Sackett, D. L.; Knutson, J. R.; Wolff, J. *J. Biol. Chem.* **1990**, *265*, 14899-14906.

(41) Dutta, A. K.; Kamada, K.; Ohta, K. *J. Photochem. Photobiol., A* **1996**, *93*, 57-64.

(42) Hou, Y.; Bardo, A. M.; Martinez, C.; Higgins, D. A. *J. Phys. Chem. B* **2000**, *104*, 212-219.

(43) Gao, F.; Mei, E.; Lim, M.; Hochstrasser, R. M. *J. Am. Chem. Soc.* **2006**, *128*, 4814-4822.

(44) Neher, E. *Biochim. Biophys. Acta* **1974**, *373*, 327-336.

(45) Fisher, L. R.; Parker, N. S. *Biophys. J.* **1984**, *46*, 253-258.

(46) Vassilev, P. M.; Kanazirska, M. P.; Tien, H. T. *Bioelectrochem. Bioenerg.* **1986**, *15*, 395-406.

(47) Mayer, M.; Kriebel, J. K.; Tosteson, M. T.; Whiteside, G. M. *Biophys. J.* **2003**, *85*, 2684-2695.

CHAPTER 5

SEQUENCE-SPECIFIC SINGLE-MOLECULE ANALYSIS OF 8-OXO-7,8-DIHYDROGUANINE LESIONS IN DNA BASED ON UNZIPPING KINETICS OF COMPLEMENTARY PROBES IN ION CHANNEL RECORDINGS

5.1 Introduction

Detection of chemical damage to genomic and mitochondrial DNA remains an important and challenging task.[1] In an ideal case, one would determine the precise chemistries and locations of all modifications occurring on individual DNA strands in healthy vs. diseased cells and be able to monitor such changes as a function of oxidative, alkylative, or micronutrient stress.[2,3] In the case of the key base oxidation product 8-oxo-7,8-dihydroguanine (OG), the most sensitive and accurate methods of quantification involve either the comet assay to produce strand breaks at each lesion or digestion followed by LC-MS analysis.[4] Shortcomings of these procedures include the loss of sequence information surrounding the lesion and the difficulty in distinguishing between multiple lesions on one strand relative to the average of a set of strands. We therefore sought a single-molecule method that would overcome these limitations.[5]

As a step towards these goals, we report the ability of short oligodeoxynucleotides to interrogate a target strand of DNA, in a sequence specific manner, for the presence of OG vs. G via electrophoretically driven translocation through an α-hemolysin (α-HL) ion channel. Other laboratories have shown that the translocation time constant τ of single-stranded DNA (ssDNA) oligomers through the nanopore is greatly increased when a terminal hairpin is present which must unfold before threading through the narrow constriction zone of α-HL.[6-11] Alternatively, addition of a small complementary DNA probe sequence also increases τ by providing a quasi-stable duplex which must unzip before translocation of the strand can be completed.[12-15] We chose the latter approach in designing a detection method for OG vs. G in a specific target sequence (Figure 5.1).

A unique feature of OG is its ability to base pair to either C or A with nearly equal stability, compared to the parent base G, which forms a highly stable base pair only with C. NMR and x-ray crystallographic studies provide the base pair structures shown in Figure 5.2.[16-21] The Watson-Crick OG:C base pair, in which both bases are in the normal *anti* conformation about the glycosidic bond, is slightly destabilized compared to the G:C base pair because of steric interactions between the C8 oxo group and the C4' oxygen of the same nucleotide; typical duplex melting temperatures are ~2 °C lower for the OG:C pair.[22] The adverse steric interaction may be relieved by rotating OG to a *syn* conformation which presents the Hoogsteen face of OG for pairing with A via two complementary H bonds rather than three. The OG:A base pair usually has a T_m lowered by

Figure 5.1. Unzipping of hydbridized DNA as it translocates through an α-HL ion channel.

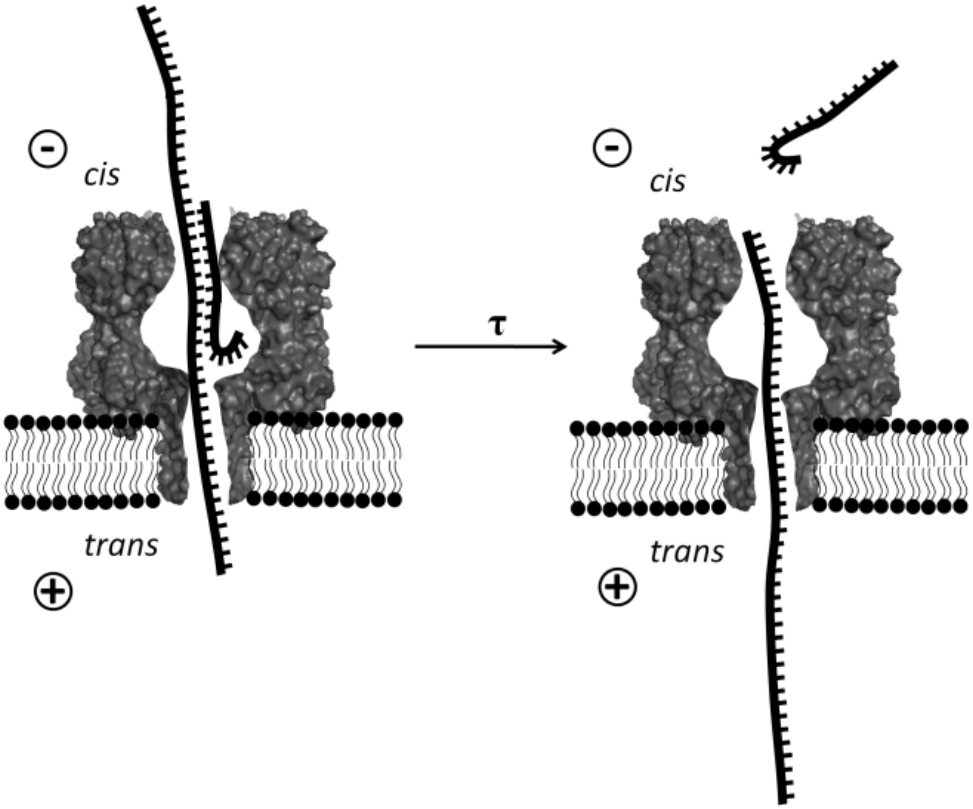
cis
trans
τ
cis
trans

Figure 5.2. Base pairing scheme of G vs. OG opposite C or A. The sugar-phosphate backbone distance (arrows) of a G(anti):A(anti) mismatch (red arrow) is wider than that of a OG(syn):A(anti) pair or a Watson-Crick G:C pair, accounting for its lower stability in the duplex.

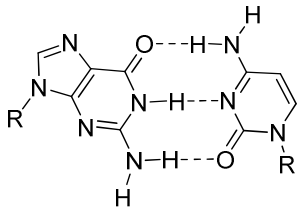

G(*anti*) : C(*anti*)

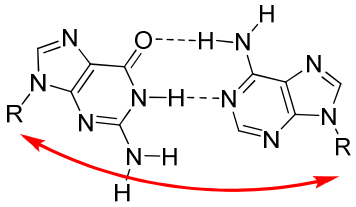

G(*anti*) : A(*anti*)

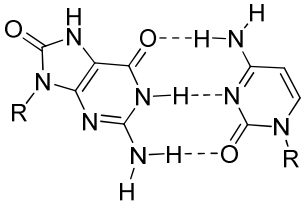

OG(*anti*) : C(*anti*)

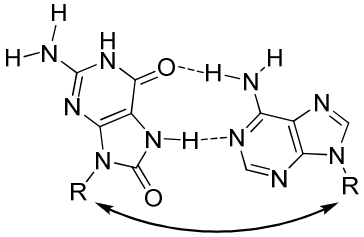

OG(*syn*) : A(*anti*)

another 1-2 °C compared to OG:C. In contrast, the presence of a G:A mismatch is significantly more destabilizing to a short duplex (ΔT_m = 6-8 °C) because two purines in *anti* conformations require a wider backbone spacing (Figure 5.2, red arrow).[23] Alternative structures for the G:A mismatch may be stabilized in tandem mismatches that provide greater π stacking or in other conformations that require low pH;[21,24-26] however, these conditions are not present in the single X:Y base (mis)pairs of the current study.

5.2 Experimental Section

5.2.1 DNA Preparation and Purification

The oligodeoxynucleotides were synthesized from commercially available phosphoramidites (Glen Research, Sterling, VA) by the DNA-Peptide Core Facility at the University of Utah. After synthesis, each oligodeoxynucleotide was cleaved from the synthetic column and deprotected according to the manufacturer's protocols, followed by purification using a semipreparation ion-exchange HPLC column with a linear gradient of 25% to 100% B over 30 min while monitoring absorbance at 260 nm (A = 20 mM Tris, 1 M NaCl pH 7 in 10% CH_3CN/90% ddH_2O, B = 10% CH_3CN/90% ddH_2O, flow rate = 3 mL/min). The purities of the oligodeoxynucleotides were determined by analytical ion-exchange HPLC running the previously mentioned buffers and method, with the exception that the flow rate was 1 mL/min. The identities for the oligodeoxynucleotides containing the modified bases OG and I were confirmed by ESI-MS.

5.2.2 Melting Temperature Analysis

The dsDNA samples were formed by placing each strand in buffer (10 mM PBS, pH 7.4, 1 M KCl) at a 1 μM concentration, followed by heating the sample at 90 ^{o}C for 5 min, then allowing the samples to slowly cool to room temperature over 3 h. Next, the samples were loaded into T_m analysis cuvettes following the manufacturer's protocol (Beckman DU 650) and placed into a UV/vis spectrophotometer equipped with a temperature-regulated heat block. Samples were thermally equilibrated at 25 ^{o}C for 20 min followed by heating to 70 ^{o}C at a rate of 0.5 ^{o}C/min. As the samples were heated, absorbance readings at 260 nm were taken every 0.5 min. The background corrected data were plotted and the T_m values were determined using two-point average analysis. Since refinement to determine the best possible probes occurred after conducting the translocation experiments, the T_m studies for the 10-mer, 12-mer, and 15-mers were not collected under the same experimental conditions as the probes containing the modified base I; thus the data do not appear to be self consistent, and this inconsistency in T_m analysis has been previously described.[27] Because of this experimental error, only data collected under identical conditions were directly compared to generate ΔT_m values.

5.2.3 Chemicals and Materials

All aqueous solutions were prepared with ultrapure water obtained from a Barnstead E-pure water purifier, with a resistance > 18 MΩ. KCl (Sigma-Aldrich), K_2HPO_4 (Mallinckrodt Chemicals), KH_2PO_4 (Mallinckrodt Chemicals), EDTA

(Mallinckrodt Chemicals), and HCl (EMD) were used as received. A 1 M KCl, 10 mM PBS, and 1 mM EDTA (pH 7.4) buffered electrolyte solution was prepared and filtered using a sterile 0.22 μm Millipore vacuum filter (Fisher Scientific) before use, and was used for all unzipping experiments. Wild-type α-hemolysin (referred to as α-HL above) was obtained as a monomer, excreted from *Staphylococcus aureus*, as a lyophilized powder from Sigma-Aldrich and List Biological Laboratories. The α-HL was frozen in ultrapure water at a concentration of 1 mg per mL for long-term storage in a -80 °C freezer, and upon use was diluted with buffered electrolyte and added to the experimental cell. The phospholipid 1,2-diphytanoyl-*sn*-glycero-3-phosphocholine (DPhPC) was purchased as a powder from Avanti Polar Lipids and stored in a -20 °C freezer. Before use, the DPhPC powder was dispersed in decane (Fisher Scientific) for a concentration of 10 mg DPhPC per mL decane. Glass nanopore membranes (GNM) were fabricated as previously described,[28] and used as a solid support for a suspended bilayer for ion channel reconstitution. Before use, GNMs were chemically modified via silanization with 2% (v:v) 3-cyanopropyldimethyl-chlorosilane (Gelest, Inc.) in acetonitrile (Fisher Scientific).[29] Upon use, GNMs were rinsed inside and out with acetonitrile, ethanol, and water, before being filled with buffered electrolyte. Ag/AgCl electrodes were prepared from 0.25 mm diameter silver wire (Alfa Aesar) being soaked in bleach. All DNA oligomers were obtained as described above, and were annealed by mixing the 65mer and probe at a 1:1 ratio, placing DNA mixture in a 90 °C water bath, and allowing

sample to slowly cool to room temperature. When not in use, the annealed DNA was stored at 4 °C.

5.2.4 Electrical Measurements

Current-time (*i-t*) measurements were performed for the unzipping experiments with 10mer and 15mer probes using a Dagan Corporation CHEM-CLAMP (Voltammeter and Amperometer Voltage Clamp Amplifier) and a Pine Instrument Company RDE4 Analog Bipotentiostat, interfaced with a PC. An in-house written LabVIEW 8.2 (National Instruments) program was used to record the *i-t* traces. Data for the 12mer duplexes were collected using a custom built high-impedance, low noise amplifier and data acquisition system (Electronic Bio Sciences, San Diego CA).

The GNM was rinsed with ethanol and ultra pure water prior to use, then filled with buffered electrolyte. An Ag/AgCl electrode was positioned inside the GNM and the back of the GNM was sealed using a Dagan Corporation pipette holder, which was attached to a pressure gauge and 10 mL gas-tight syringe (Hamilton). A second Ag/AgCl electrode was positioned within the experimental cell; the same buffered electrolyte within the GNM was used to fill the cell and submerge the GNM orifice, α-HL was then added to the cell (external to the GNM). A voltage was applied across the GNM orifice and the resultant current was measured as a function of time; voltages were applied *cis* vs.*trans* using the CHEM-CLAMP instrumentation and *trans* vs.*cis* for the EBS DC system, with respect the α-HL channel which was always external to the GNM.

A suspended bilayer was generated by depositing a 10 mg DPhPC per mL decane lipid solution across the GNM orifice, which produced a drop in conductance as a voltage was applied across the GNM orifice; an open GNM orifice has a resistance of ~10 MΩ and the presence of a bilayer increases the resistance to ~100 GΩ. A pressure was then applied to the back of the GNM to thin the lipid solution into a functional bilayer for protein channel reconstitution to occur.[29] After protein channel insertion, the annealed DNA was added to the experimental cell to a final concentration of 5 μM. A minimum of 500 events were collected for each sample, except the 15mer samples due the stability of the duplex as discussed above. Data were collected with a 20 kHz filter and sampled at 100 kHz.

5.2.5 Data Analysis

Only events that were >1 ms in duration and produced ≥ 75% blocking to the open channel current were analyzed. Histograms of event duration were plotted and fit as a single exponential decay for either each population as a whole to determine τ, or as two populations to determine $\tau_{3'}$ and $\tau_{5'}$. When the data were fit as whole populations to determine τ, the fit excluded the first bin to avoid weighting the fit toward faster event durations due to unduplexed DNA. Events where extracted using QuB (version 1.5.0.31) and fit using OriginPro (ver 8). Density plots were generated using data analysis programs provided by Electronic Bio Sciences, San Diego.

5.3 Results and Discussion

5.3.1 10mer and 15mer Duplex Unzipping

In the present work, we took advantage of the difference in stability of G vs. OG opposite C or A to design short complementary probes that would slow the translocation of ssDNA through the α-HL ion channel. Experiments were conducted initially with a set of 10mer (10merC or 10merA) and 15mer (15merC and 15merA) probes complementary to the central region of a 65mer (denoted as G or OG) resulting in the following eight duplexes: G:10merC or A, OG:10merC or A, G:15merC or A and OG:15merC or A, as shown in Table 5.1 (sequences were selected to minimize secondary structure). Melting temperature, T_m, studies conducted in the same buffer solution (10 mM PBS, pH 7.4, 1 M KCl, 1 mM EDTA) as used for electrical measurements of the nanopore showed the general trends expected for stability of a single X:Y mispair compared to a native G:C pair. The order of stability was found to be G:C > OG:C > OG:A > G:A for both 10mer probes and 15mer probes annealed to the 65mer target strand. The 10mer probes were more sensitive to the presence of a single base mismatch; the T_m for a G:A mismatch was 8 °C lower than the parent G:C in the 10mer but only 5.5 °C lower in the 15mer duplex.

Electrical measurements were employed to determine the duplex stability as a function of the unzipping time constant τ. To perform these measurements, a voltage was applied across an α-HL ion channel reconstituted into a lipid bilayer suspended across the orifice of a glass nanopore membrane (GNM).[5,29-34] The annealed duplex DNA was then electrophoretically driven into the α-HL

Table 5.1. Melting temperatures (T_m) determined through thermal denaturation studies for 10mer and 15mer complementary probes annealed to a target 65mer oligodeoxynucleotide.

5'-$(T)_{25}$-TTGAGCC**X**TCAGATG-$(T)_{25}$ 10mer: 3'CTCAG**Y**AGTC		
Sequence	T_m (°C)	ΔT_m (°C)
X=G, Y=C	51.9 ± 0.6	--
X=G, Y=A	44.1 ± 0.6	-7.8 ± 0.8
X=OG, Y=C	49.0 ± 1.6	-2.9 ± 1.7
X=OG, Y=A	47.3 ± 1.3	-4.6 ± 1.4
5'-$(T)_{25}$-TTGAGCC**X**TCAGATG-$(T)_{25}$ 15mer: 3'AACTCAG**Y**AGTCTAC		
Sequence	T_m (°C)	ΔT_m (°C)
X=G, Y=C	58.2 ± 1.0	--
X=G, Y=A	52.7 ± 0.6	-5.5 ± 1.2
X=OG, Y=C	57.8 ± 0.5	-0.4 ± 1.1
X=OG, Y=A	53.5 ± 1.2	-4.7 ± 1.6

channel where it unzipped for translocation (Figure 5.1). The analysis of duplex unzipping kinetics was performed by plotting histograms of $\log_{10}$(events) vs.event duration time. From the slope of these histograms, the translocation time constant τ was determined for each duplex by assuming that unzipping follows a first-order kinetics law. Figure 5.3 shows an example fitting for G:10merC (or A) and OG:10merC (or A) for +80 mV applied voltage (*trans* vs.*cis*). Probes of 25 nucleotides in length (5'-AAAAAAACATCTGA**(C or A)**GGCTCAAAAA) were also examined, but due to the very stable nature of the resulting duplex, an adequate sample of events could not be collected for voltages <140 mV; thus, 25mer probes were not studied further.

Measurements of the translocation of 65mers G and OG in the presence of C or A-containing complementary probes indicated a correlation between the values of τ and T_m. Figure 5.4 shows the time constant for unzipping as a function of the melting temperature for 10mer and 15mer duplex sequences. As seen from these data, the unzipping time increases in the order G:C > OG:C > OG:A > G:A, and correlates well with duplex melting temperatures, for both 10 and 15mer probes. The duplexes generated with the 10mer probes exhibited unzipping times that were distinctly different from one another at +80 mV, but at higher voltages (+100 mV and +120 mV) unzipping proceeded at similar rates, decreasing the measurement sensitivity. For the 15mer duplexes, use of a lower voltage (+80 mV) resulted in event durations that were very long (> 10 s for G:15merC), making it difficult to collect an adequate population of events to distinguish between the different duplexes, and at higher voltages again the

Figure 5.3. Plot of $\log_{10}$(Events) vs. event duration for unzipping of duplexes formed with a 65mer containing G or OG at position 33 and either C or A centered opposite in the 10mer: G:10merC, G:10merA, OG:10merC, and OG:10merA. The slope of the straight line is used to compute the unzipping time constant, τ, at 80 mV, *trans vs. cis.*

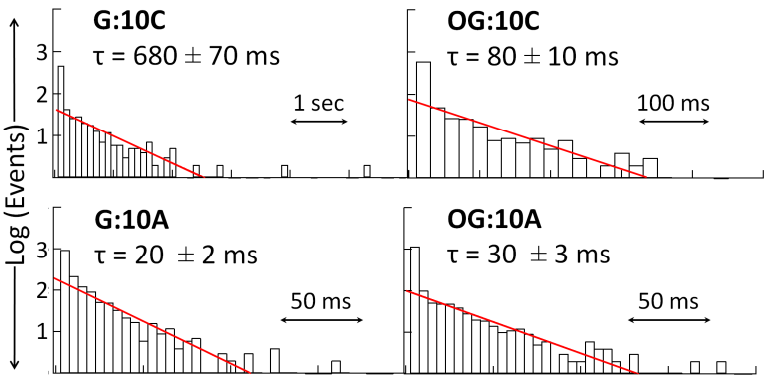
G:10C
τ = 680 ± 70 ms
1 sec
OG:10C
τ = 80 ± 10 ms
100 ms
G:10A
τ = 20 ± 2 ms
50 ms
OG:10A
τ = 30 ± 3 ms
50 ms
Log (Events)
3
2
1

Figure 5.4. Plot of $\log_{10}[\tau(ms)]$ as a function of the duplex melting temperature for G:10merC or A (abbreviated G:10C and G:10A) and OG:15merC or A (abbreviated as OG:15C and OG:15A). Data are shown for applied biases of 80 mV, 100 mV, and 120 mV, *trans vs. cis*.

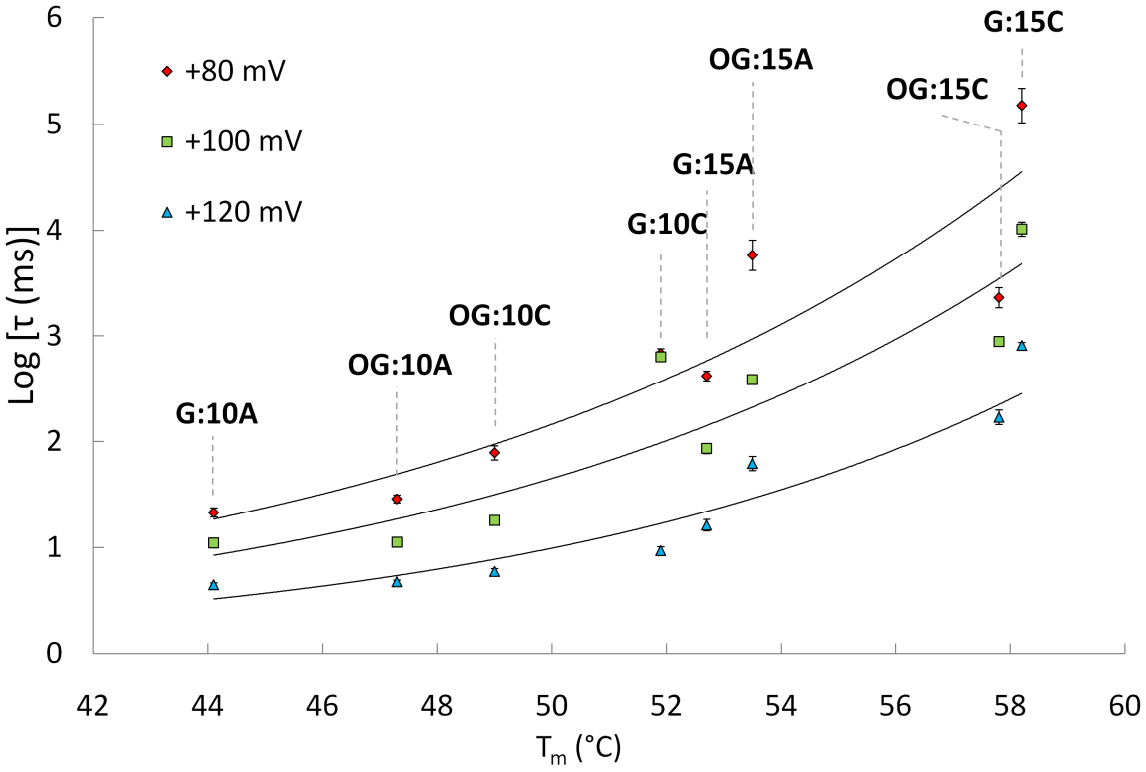
+80 mV
+100 mV
+120 mV
G:10A
OG:10A
OG:10C
G:10C
G:15A
OG:15A
OG:15C
G:15C
Log [τ (ms)]
T_m (°C)
0
1
2
3
4
5
6
42
44
46
48
50
52
54
56
58
60

unzipping times show less sensitivity to the duplex stability. From this initial study it was determined that the probe design must balance the lower sensitivity of the 10mer and the longer τ values of the 15mer that limit event frequency. This process of probe refinement is described below.

5.3.2 12mer Duplex Unzipping

Although the 10mer probes displayed T_m values that were more sensitive to the presence of a single X:Y mispair, the τ values for the 15mer probes were generally in a better event duration range for discriminating between G and OG. Duplexes with T_m values >50 °C provided sufficiently long translocation times that could be readily discerned from translocations of the 65mer (~280 μs). In order to refine the probe design, we sought methods to enlarge the difference in event duration between OG:A and G:A mispairs. Previous studies have shown that locating the mismatch further away from the center of the probe led to a greater distinction in unzipping times between correctly paired and mismatched duplexes.[35] Thus, two new sets of 12mer probes were tested in which the X:Y base pair of interest was located near either the 3' end or the 5' end of the probe, and care was taken to maintain the same number of G:C and A:T base pairs in each of the two sets so that a meaningful comparison could be made. As a further refinement, the G:C base pair immediately 5' to the G/OG site was converted to a C:I base pair. Inosine (I) is the nucleoside form of the hypoxanthine base which lacks the 2-amino group of G and forms a weaker base pair with C. We predicted this substitution might destabilize the adjacent G:A

mispair to a greater extent than the OG:A pair; G:A mispairs are known to be sensitive to the surrounding sequence, particularly on the 5' side of the G site.[25] The T_m data for the resulting 12mer probes annealed to 65mer target strands are shown in Tables 5.2A, 5.2B, and 5.2C, in which the probe is shifted in either the 5' or 3' direction or centered on the X:Y pair of interest.

The data in Tables 5.2A-C confirm that the displacement of the probe sequences with respect to the potential mismatched base pair can influence the thermal stability of the duplexes. Importantly, shifting the probe sequence toward the 3' direction relative to the target strand (Y in position 10) led to a greater difference between the relatively stable OG:A pairing (ΔT_m = -4.6 °C with respect to G:C, Table 5.2C) and the unstable pairing of G:A (ΔT_m = -8.3 °C) compared to other probe arrangements. When the probe was shifted in the opposite direction (position 3), the ΔT_m values were smaller (Table 5.2A).

Electrical measurement of the 12mers annealed to G or OG-containing 65mers unzipping and translocating through the α-HL ion channel were conducted at 80 mV to maximize the apparent differences in unzipping times due to the duplex stability. The unzipping time, τ, was determined in the same manner as described above for the 10mer and 15mer duplexes; the unzipping events were plotted as histograms of $\log_{10}$(events) vs. event duration. A plot of τ as a function of the shift in probe position is presented in Figure 5.5 for each of the 12mer duplexes shown in Table 5.2.

We again found that the unzipping times corresponded well to the melting temperatures; for each position (3, 6, and 10), the τ value reflects the expected

Table 5.2. T_m studies with 12mer complementary probes in various positions of X:Y. The probe strand is shifted 5' (A), centered (B), or shifted 3' (C) with respect to the interrogated base X. The position of Y is denoted as position 3, 6, or 10, accordingly.

A. Position 3 5'-$(T)_{23}$-TTTTGAGCCXTCAGATGTT-$(T)_{23}$ 3'-AA AACTCAIYAG		
Sequence	T_m (°C)	ΔT_m (°C)
X=G, Y=C	54.2 ± 0.4	--
X=G, Y=A	48.1 ± 1.3	-6.2 ± 1.4
X=OG, Y=C	52.8 ± 0.3	-1.4 ± 0.5
X=OG, Y=A	50.5 ± 0.3	-3.7 ± 0.5
B. Position 6 5'-$(T)_{23}$- TT TTGAGCCXTCAGATGTT -$(T)_{23}$ 3'-ACTCGIYAGTCT		
Sequence	T_m (°C)	ΔT_m (°C)
X=G, Y=C	55.0 ± 0.1	--
X=G, Y=A	50.2 ± 0.3	-4.8 ± 0.3
X=OG, Y=C	53.0 ± 1.3	-2.0 ± 1.3
X=OG, Y=A	51.0 ± 0.1	-4.0 ± 0.1
C. Position 10 5'-$(T)_{23}$- TT TTGAGCCXTCAGATGTT -$(T)_{23}$ 3'-GIYAGTCTACAA		
Sequence	T_m (°C)	ΔT_m (°C)
X=G, Y=C	51.8 ± 0.3	--
X=G, Y=A	43.5 ± 0.7	-8.3 ± 0.8
X=OG, Y=C	48.8 ± 0.4	-3.0 ± 0.5
X=OG, Y=A	47.2 ± 0.3	-4.6 ± 0.4

I = inosine

Figure 5.5. Plot of τ as a function of position for the X:Y site of interest. Y position is denoted relative to the 5' end of the 12-mer probe sequence. Sequences are shown in Table 5.2.

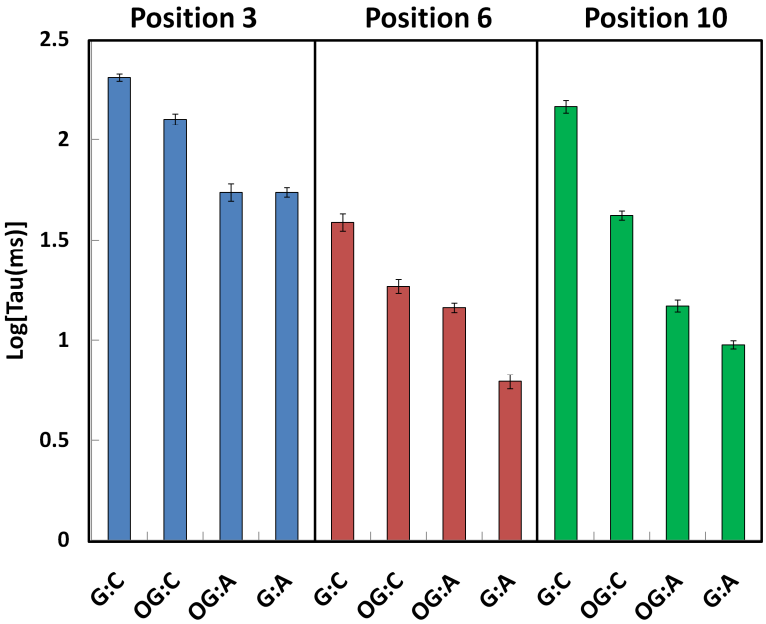
Position 3
Position 6
Position 10
Log[Tau(ms)]
2.5
2
1.5
1
0.5
0
G:C
OG:C
OG:A
G:A
G:C
OG:C
OG:A
G:A
G:C
OG:C
OG:A
G:A

duplex stability as shown in the melting temperatures (Table 5.2), G:C > OG:C > OG:A > G:A. Additionally, the largest difference in τ between the duplexes occurs for position 10 as predicted by the ΔT_m discussed above, demonstrating that the unzipping time τ is a sufficient measure of duplex DNA stability to allow the presence of a single DNA damage site to be detected.

However, these positional studies highlighted another feature of DNA translocation with the ion channel: DNA can enter the α-HL channel to unzip the duplex from either the 5' or 3' orientation. For the generation of the asymmetrical 12mer probes (position 3 and position 10), the duplex unzipping times are expected to depend on whether the strand enters from the terminus closer to or farther away from the mismatched base pair. The melting temperature, a thermodynamic phenomenon, will not reflect the kinetics of 5' or 3' initiated dissociation, whereas the unzipping of a duplex in the α-HL channel has been shown to differ based on 5' or 3' entrance.[36]

To examine 3' vs.5' entrance into the α-HL channel, multi-dimensional plots were generated to examine the current blockage level as a function of event duration and event population density. Figure 5.6 illustrates how the unzipping events are dispersed based on the current blockage level and translocation time. Generally, the duplexes formed with an asymmetrical probe sequence (positions 3 and 10) displayed two populations of events separated by both the current blockage level and the event duration, whereas the symmetrical sequences (position 6 probes) did not show separate event populations based on either parameter. We interpret the multiple populations as being due to 3' vs.5'

Figure 5.6. Plots showing the event population density, least populated (blue) to most populated (red), for the current blockage level of 12mer probes annealed to 65mer target strands as a function of event duration for an applied voltage of -80 mV (*cis vs.trans*).

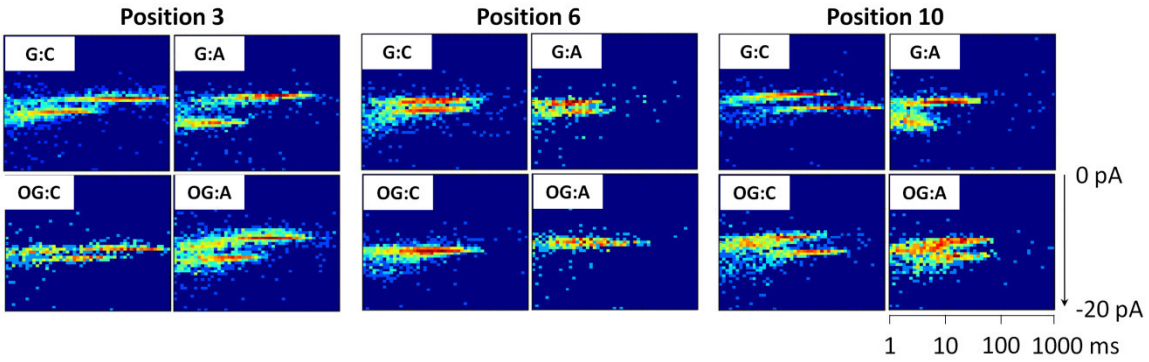
Position 3
Position 6
Position 10
G:C
G:A
OG:C
OG:A
0 pA
-20 pA
1
10
100
1000 ms

entrance into the α-HL channel. It has been shown that for immobilized homopolymer sequences that 3' and 5' entrance into the α-HL channel have different current blockage levels, and these may change significantly based on the nucleotide identity within the channel.[36] Additionally, as shown above and by previous reports, duplex sequences of different stabilities have different unzipping event durations, with the less stable duplex exhibiting the faster time constant.[10,11, 14,37]

Because the 65mer sequence is a heterosequence embedded within a poly-dT background sequence at each end, and based on the orientation of the molecule upon entry into the α-HL channel and the probe sequence, a variable amount of the heterosequence will be within the α-HL channel. Thus, assignment of entry via the 3' or 5' end was not made based on the current blockage level, but rather on the event duration. We assign 3' vs.5' entrance of the 65mer into the α-HL based on the expected stability of the duplex by looking at the first few terminal base pairs. (Note: all 3'/5' designations are made referring to the orientation of the 65mer sequence because it enters the channel first.) For example, the position 3 G:C duplex is expected to be more stable for 3' entrance relative to 5' entrance as there are two G:C base pairs and one A:T base pair on the 3' end of the duplex, but three A:T base pairs on the 5' end (Table 5.2). Thus the 3' entrance is expected to produce a longer unzipping time due to the higher G:C base pair content. Examining the position 3 G:C duplex density plot in Figure 5.6, the deeper blocking events have longer event durations than those of more shallow blocking, indicating that the deeper block

corresponds to 3’ entrance whereas the more shallow blocking level with shorter event durations indicates 5’ entrance. The opposite is expected to be true for the position 10 G:C duplex, where the higher terminal G:C base pair content is located at the 5’ end of the duplex, which is expected to produce longer event durations relative to the 3’. From the density plot in Figure 5.6, the deeper blockage assigned as 3’ entrance possesses shorter event durations relative to the shallower 5’ blockage. This convention of the deeper blockage corresponding to 3’ entrance and shallower blockages being 5’ entrance was applied to all the duplexes that could easily be separated into two distinct populations. The data for each duplex were separated into two populations and fit with a single exponential decay to determine the unzipping time constants, $\tau_{3'}$ and $\tau_{5'}$ for 3’ entrance or 5’ entrance, respectively. The position 6 OG:C and OG:A duplexes could not be resolved into two populations, and the time constant was assigned to be τ.

Figure 5.7 compares the time constants for 3’ vs.5’ entrance as assigned by the expected event duration from the orientation specific duplex stability. This $\tau_{3'}$ and $\tau_{5'}$ assignment agrees remarkably well with the predicted unzipping times for 3’ and 5’ entry. For the symmetrical probe sequence where the data can be resolved into two populations (G:C and G:A, position 6), there is little difference between $\tau_{3'}$ and $\tau_{5'}$. This is expected as both duplexes possess the same amount of terminal G:C base pair content. It is not understood why two populations are not resolvable for OG:C and OG:A in position 6. Further, for position 3 duplexes, as discussed above, the 5’ entrance is expected to reflect a

Figure 5.7. Plot of $\tau_{3'}$ (light bars) and $\tau_{5'}$ (dark bars) as a function of position for the X:Y pair. The assignment of $\tau_{3'}$ and $\tau_{5'}$ is based on the expected event duration times for duplex unzipping. Position 6 OG:C and OG:A duplexes could not be resolved into two distinct populations and were only assigned a single τ (striped bars).

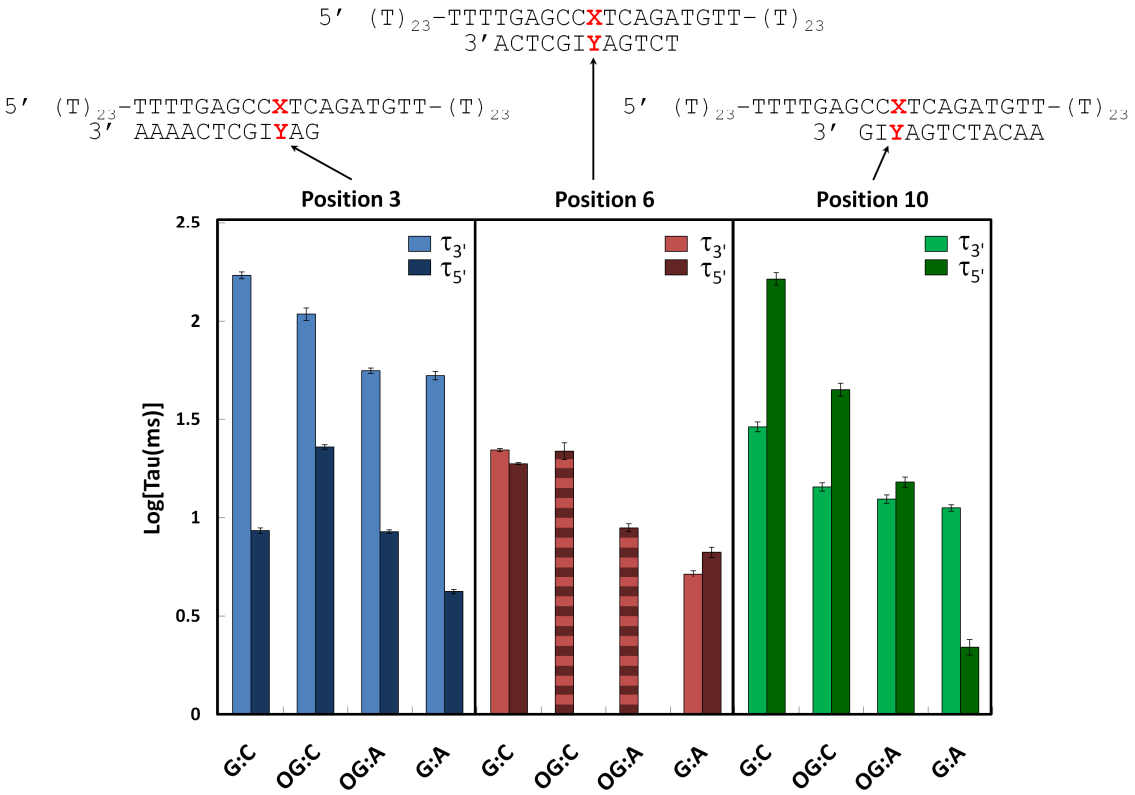
5′ (T)23-TTTTGAGCCXTCAGATGTT-(T)23
3′ACTCGIYAGTCT
5′ (T)23-TTTTGAGCCXTCAGATGTT-(T)23
3′ AAAACTCGIYAG
5′ (T)23-TTTTGAGCCXTCAGATGTT-(T)23
3′ GIYAGTCTACAA
Position 3
Position 6
Position 10
Log[Tau(ms)]
2.5
2
1.5
1
0.5
0
τ3'
τ5'
G:C
OG:C
OG:A
G:A

more stable duplex relative to 3' entrance. This is observed for position 3 duplexes G:C, OG:C, and OG:A, with $\tau_{3'} > \tau_{5'}$, but also for G:A, which is not well understood as the G:A mismatch should destabilize the duplex for 3' entrance. Finally, for position 10 duplexes, the 5' entrance is expected to be more stable than the 3' entrance ($\tau_{3'} < \tau_{5'}$), except for the G:A duplex where the mismatch destabilizes the 5' end of the duplex relative to the 3'. This prediction is reflected in $\tau_{3'} > \tau_{5'}$.

It has been previously demonstrated that the entry of ssDNA into the α-HL pore will produced two event populations as a result of either 3' entry or 5' entry of the DNA strand,[36] separated in current blockage level and event duration.[38] Additionally, it has been reported that 5' entry is less favorable relative to 3' entry due to the tilt of the DNA bases toward the 5' terminus, making 5' entry, and subsequent translocation, occur at a lower rate relative to 3' entry.[12,38,39] Based on this, it was not anticipated that distinct populations would appear as shown in Figure 6, separated by both the event duration and current blockage level, with an applied bias of 80 mV, as an 80 mV voltage bias is near the minimum electrophoretic force required to initiate DNA interaction with the α-HL channel.[40] Other duplex unzipping experiments have noted multiple event populations distinguishable by the event duration for a single duplex DNA sample,[11,13,14,37,41] requiring a more complicated analysis than presented above. Unlike the previous duplex unzipping experiments in which the current blockage level was not emphasized in the analysis, and only the temporal separation was directly applied, the analysis presented here uses the current blockage to distinguish

populations prior to analyzing the temporal separation. This allowed a simplified mechanism to be applied via single-exponential fits that generally correspond well to the relative 3' vs. 5' duplex stability. It is unknown if the duplex region influences the DNA entry into the α-HL channel in a manner different from ssDNA, allowing equal 3' and 5' entry rates.

Overall, the data presented in Figure 5.7 reveal that the relative position of a DNA damage site can be determined by how it influences the stability in an orientation specific manner. Deviations present in the data from the expected duplex stability are attributed to possible interactions other than hydrogen bond strength between the base pairs and are not fully understood. However, further refinement of the probe design may lead to improved sensitivity to DNA damage, for example by chemical modification within the probe to further stabilize or destabilize the resultant duplex.

5.4 Conclusions

These studies demonstrate that a single oxidized damage site can be detected in a sequence specific manner by annealing a probe sequence to sequence surrounding the damage site, and observing the rate of duplex unzipping required for translocation through the α-HL ion channel. The presence of a single OG will influence the duplex stability in a specific manner depending on whether OG base pairs with C or A, both of which produce event duration times distinct from the native G:C and G:A base pairs. Additionally, if the probe is designed so that the DNA damage site occurs on the 3' or 5' end of the probe,

as opposed to the middle, the duplex stability will vary based on 5' or 3' entry into the α-HL channel and will be reflected in the current blockage level as a function of the event duration, producing two distinct populations of events. This ability to discern the relative location of the DNA damage site is a first step towards location specific DNA damage detection. Further tailoring of the probe sequence with additional chemical modifications might be used to enhance the selectivity for the DNA damage site, providing a powerful tool in DNA damage detection and characterization.

5.5 References

(1) Cadet, J.; Poulsen, H. *Free Radical Biology and Medicine* **2010**, *48*, 1457-1459.

(2) Delaney, J. C.; Essigmann, J. M. *Chemical Research in Toxicology* **2008**, *21*, 232-252.

(3) Cadet, J.; Douki, T.; Ravanat, J.-L. *Free Radical Biology and Medicine* **2010**, *49*, 9-21.

(4) Azqueta, A.; Shaposhnikov, S.; Collins, A. R. *Mutation Research/Genetic Toxicology and Environmental Mutagenesis* **2009**, *674*, 101.

(5) Schibel, A. E. P.; An, N.; Jin, Q.; Fleming, A. M.; Burrows, C. J.; White, H. S. *J. Am. Chem. Soc.* **2010**, *51*, 17992-17995.

(6) Vercoutere, W.; Winters-Hilt, S.; Olsen, H.; Deamer, D.; Haussler, D.; Akeson, M. *Nature Biotechnol.* **2001**, *19*, 248-252.

(7) Vercoutere, W. A.; Winters-Hilt, S.; DeGuzman, V. S.; Deamer, D.; Ridino, S. E.; Rodgers, J. T.; Olsen, H. E.; Marziali, A.; Akeson, M. *Nucl. Acids Res.* **2003**, *31*, 1311-1318.

(8) Winters-Hilt, S.; Vercoutere, W.; DeGuzman, V. S.; Deamer, D.; Akeson, M.; Haussler, D. *Biophys. J.* **2003**, *84*, 967-976.

(9) Dudko, O. K.; Mathe, J.; Szabo, A.; Meller, A.; Hummer, G. *Biophys. J.* **2007**, *92*, 4188-4195.

(10) Mathé, J.; Visram, H.; Viasnoff, V.; Rabin, Y.; Meller, A. *Biophys. J.* **2004**, *87*, 3205-3212.

(11) McNally, B.; Wanunu, M.; Meller, A. *Nano Lett.* **2008**, *8*, 3418-3422.

(12) Muzard, J.; Martinho, M.; Mathé, J.; Bockelmann, U.; Viasnoff, V. *Biophys. J.* **2010**, *98*, 2170-2178.

(13) Sauer-Budge, A. F.; Nyamwanda, J. A.; Lubensky, D. K.; Branton, D. *Phys. Rev. Lett.* **2003**, *90*, 238101-1-4.

(14) Sutherland, T. C.; Dinsmore, M. J.; Kraatz, H.-B.; Lee, J. S. *Biochem. Cell Biol.* **2004**, *82*, 407-412.

(15) Viasnoff, V.; Chiaruttini, N.; Bockelmann, U. Eur. *Biophys. J.* **2009**, *38*, 263-269.

(16) McAuley-Hecht, K. E.; Leonard, G. A.; Gibson, N. J.; Thomson, J. B.; Watson, W. P.; Hunter, W. N.; Brown, T. *Biochemistry* **1994**, *33*, 10266-10270.

(17) Lipscomb, L. A.; Peek, M. E.; Morningstar, M. L.; Verghis, S. M.; Miller, E. M.; Rich, A.; Essigmann, J. M.; Williams, L. D. *Proc. Natl. Acad. Sci. USA* **1995**, *92*, 719-723.

(18) Maskos, K.; Gunn, B. M.; LeBlanc, D. A.; Morden, K. M. *Biochemistry* **1993**, *32*, 3583-3595.

(19) Carbonnaux, C.; Van der Marel, G. A.; Van Boom, J. H.; Guschlbauer, W.; Fazakerley, G. V. *Biochemistry* **1991**, *30*, 5449-5458.

(20) Nikonowicz, E. P.; Gorenstein, D. G. *Biochemistry* **1990**, *29*, 8845-8858.

(21) Patel, D. J.; Kozlowski, S. A.; Ikuta, S.; Itakura, K. *Biochemistry* **1984**, *23*, 3207-3217.

(22) Plum, G. E.; Grollman, A. P.; Johnson, F.; Breslauer, K. J. *Biochemistry* **1995**, *34*, 16148-16160.

(23) Berashevich, J.; Chakraborty, T. *J. Chem. Phys.* **2009**, *130*, 015101.

(24) Allawi, H. T.; SantaLucia, J. *Biochemistry* **1998**, *37*, 2170-2179.

(25) Cheng, J.-W.; Chou, S.-H.; Reid, B. R. *J. Mol. Biol.* **1992**, *228*, 1037-1041.

(26) Gao, X.; Patel, D. J. *J. Am. Chem. Soc.* **1988**, *110*, 5178-5182.

(27) Mergny, J.-L.; Lacroix, L. *Oligonucleotides* **2003**, *13*, 515-537.

(28) Zhang, B.; Galusha, J.; Shiozawa, P.G.; Wang, G.; Bergren, A.J.; Jones, R.M.; White, R.J.; Ervin, E.N.; Cauley, C.; White, H.S. *Anal. Chem.* **2007**, *79*, 4778–4787.

(29) White, R. J.; Ervin, E. N.; Yang, T.; Chen, X.; Daniel, S.; Cremer, P. S.; White, H. S. *J. Am. Chem. Soc.* **2007**, *129*, 11766-11775.

(30) Kawano, R.; Schibel, A. E. P.; Cauley, C.; White, H. S. *Langmuir* **2008**, *25*, 2850-2855.

(31) Ervin, E. N.; Kawano, R.; White, R. J.; White, H. S. *Anal. Chem.* **2008**, *80*, 2069-2076.

(32) Ervin, E. N.; Kawano, R.; White, R. J.; White, H. S. *Anal. Chem.* **2008**, *81*, 533-537.

(33) Lathrop, D. K.; Ervin, E. N.; Barrall, G. A.; Keehan, M. G.; Kawano, R.; Krupka, M. A.; White, H. S.; Hibbs, A. H. *J. Am. Chem. Soc.* **2010**, *132*, 17992-17995.

(34) Chen, Q.; Liu, J.; Schibel. A. E. P.; White, H. S.; Wu, C. *Macromolecules* **2010**, *43*, 10594-10599.

(35) Urakawa, H.; El Fantroussi, S.; Smidt, H.; Smoot, J. C.; Tribou, E. H.; Kelly, J. J.; Noble, P. A.; Stahl, D. A. *Appl. Environ. Microbiol.* **2003**, *69*, 2848-2856.

(36) Purnell, R. F.; Mehta, K. K.; Schmidt, J. J. *Nano Lett.* **2008**, *8*, 3029-3034.

(37) Howorka, S.; Cheley, S.; Bayley, H. *Nat. Biotechnol.* **2001**, *19*, 636-639.

(38) Mathé, J.; Aksimentlev, A.; Nelson, D. R.; Schulten, K.; Meller, A. *Proc. Natl. Acad. Sci.* **2005**, *102*, 12377-1282.

(39) Akeson, M.; Branton, D.; Kasianowics, J. J.; Brandin, E.; Deamer, D. W. *Biophys. J.* **1999**, *77*, 3227-3233.

(40) Henrickson, S. E.; Misakian, M.; Robertson, B.; Kasianowicz, J. J. *Phys. Rev. Lett.* **2000**, *85*, 3057-3060.

(41) Howorka, S.; Movileanu, L.; Braha, O.; Bayley, H. *Proc. Natl. Acad. Sci.* **2001**, *98*, 12996-13001.

5.6 Appendix

In this appendix, the approach to determine the unzipping time constant τ is examined for the duplex unzipping experiments described in section 5.2.4. Unzipping events were collected and plotted as event duration histograms. The data were treated using two strategies, but both assume a first-order kinetics law.

Data were fit as single populations for the 10mer, 12mer, and 15mer duplexes; plots of $\log_{10}$(Events) vs. Event Duration were fit with a straight line, from which the slope was used to determine τ. For these fits, the first bin was excluded to prevent the weighting of the fit towards the faster events. Fits treating the data as single populations are shown in Figures 5.9, 5.10 and 5.12. The second type of fitting separates the data into two populations (excluding position 6 OG:C/A), and each population is fit with a single-exponential decay. The data are plotted as Events vs. Event Duration, and all bins are included for each fit, see Figures 5.13-5.17.

Additionally, this appendix also includes a representative melting curve (Figure 5.8), example *i-t* traces for the unzipping events as shown in Figure 5.11, and an example of the 65mer translocation *i-t* trace and event duration histogram (Figure 5.18).

Figure 5.8. Representative T_m profile for the absorbance of the OG:10merA duplex as a function of temperature.

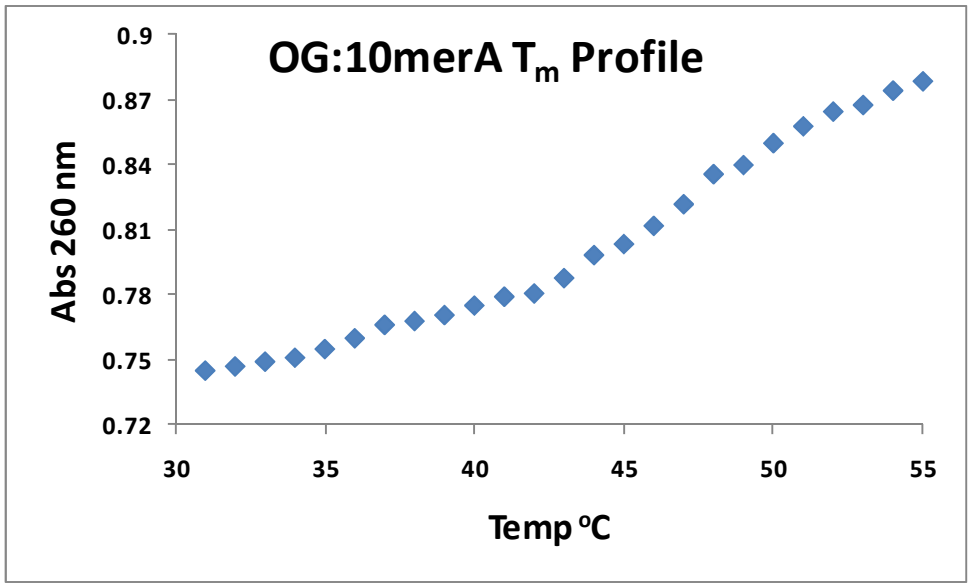
OG:10merA T_m Profile
Abs 260 nm
0.9
0.87
0.84
0.81
0.78
0.75
0.72
30
35
40
45
50
55
Temp °C

Figure 5.9. Event duration histograms for 65merG:10merC/A and 65merOG:10merC/A for (A) +100 mV and (B) +120 mV applied voltage (*trans* vs *cis*).

(A)

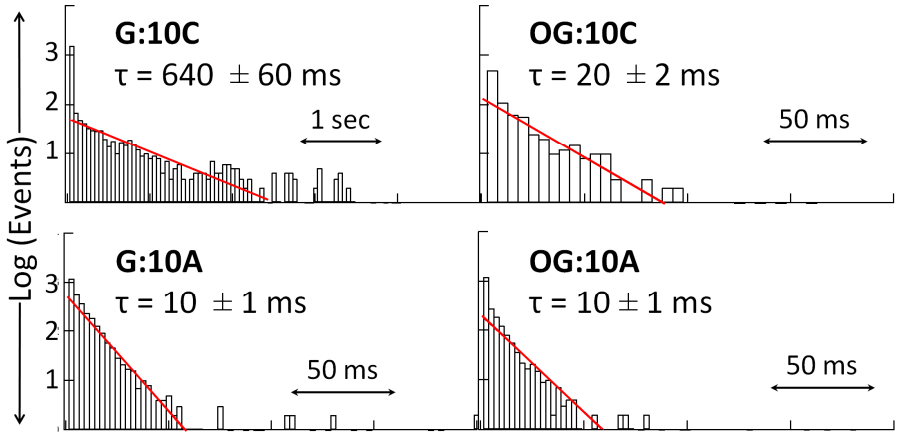
G:10C
τ = 640 ± 60 ms
1 sec
OG:10C
τ = 20 ± 2 ms
50 ms
G:10A
τ = 10 ± 1 ms
50 ms
OG:10A
τ = 10 ± 1 ms
50 ms
Log (Events)
3
2
1

(B)

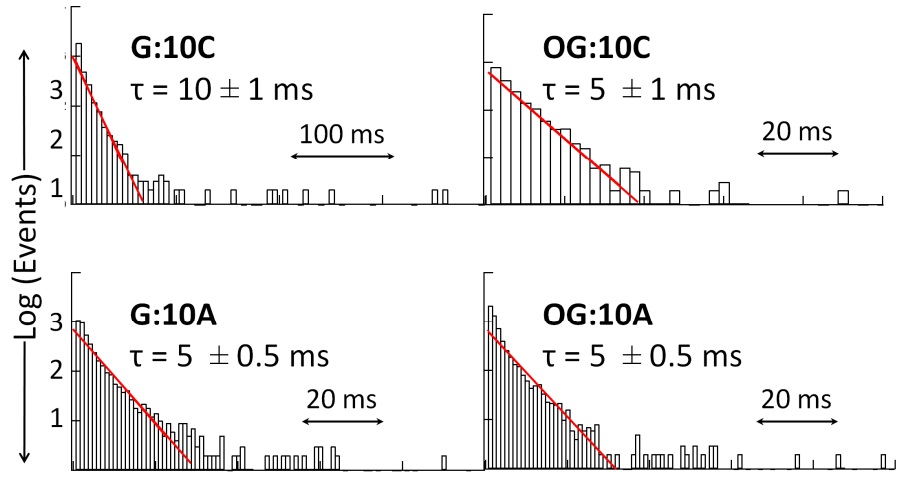
G:10C
τ = 10 ± 1 ms
100 ms
OG:10C
τ = 5 ± 1 ms
20 ms
G:10A
τ = 5 ± 0.5 ms
20 ms
OG:10A
τ = 5 ± 0.5 ms
20 ms
Log (Events)
3
2
1

Figure 5.10. Event duration histograms for 65merG:15merC/A and 65merOG:15merC/A for (A) +80 mV, (B) +100 mV, and (C) +120 mV applied voltage (*trans* vs *cis*). The stability of the 15mer duplexes prohibited the collection of a large population of unzipping events at +80 mV, especially for the more stable G:15merC, OG:15merC, and OG:15merA duplexes.

(A)

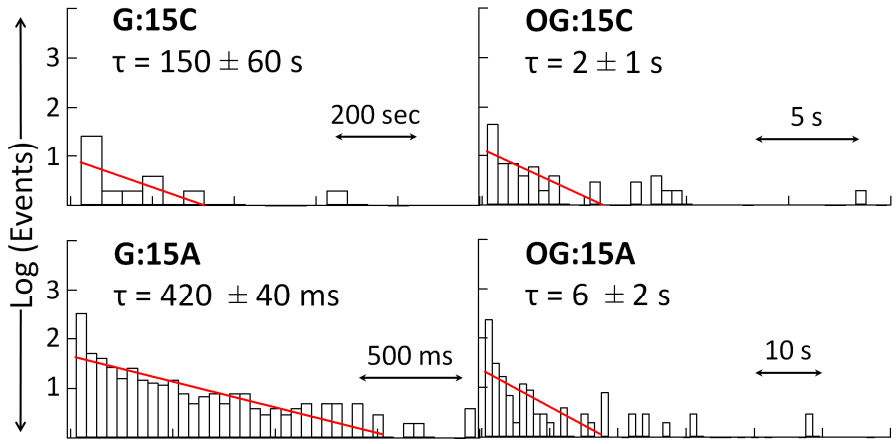
G:15C
τ = 150 ± 60 s
200 sec
OG:15C
τ = 2 ± 1 s
5 s
G:15A
τ = 420 ± 40 ms
500 ms
OG:15A
τ = 6 ± 2 s
10 s
Log (Events)
1
2
3

(B)

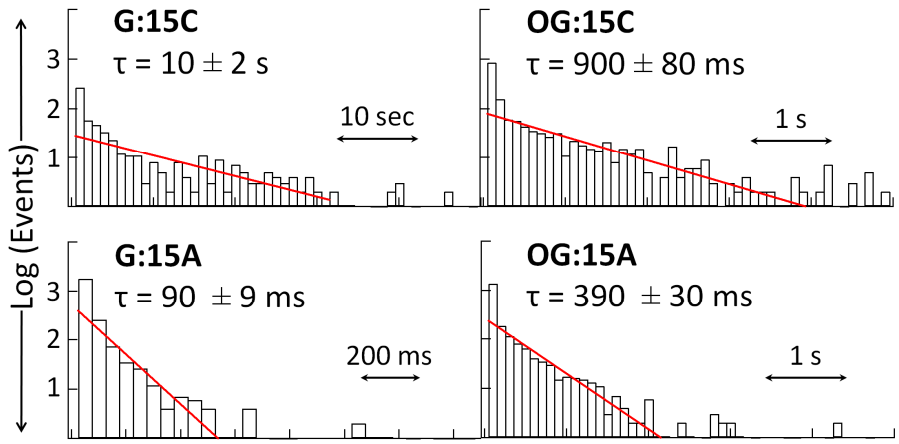
G:15C
τ = 10 ± 2 s
10 sec
OG:15C
τ = 900 ± 80 ms
1 s
G:15A
τ = 90 ± 9 ms
200 ms
OG:15A
τ = 390 ± 30 ms
1 s
Log (Events)
1
2
3

(C)

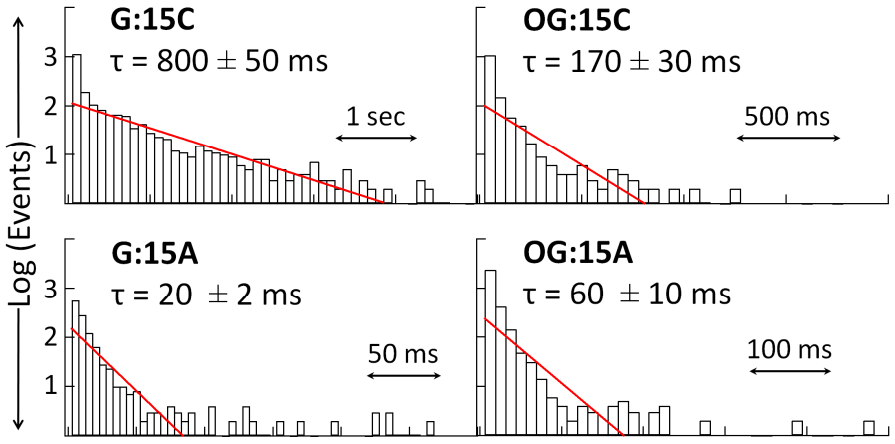
G:15C
τ = 800 ± 50 ms
1 sec
OG:15C
τ = 170 ± 30 ms
500 ms
G:15A
τ = 20 ± 2 ms
50 ms
OG:15A
τ = 60 ± 10 ms
100 ms
Log (Events)
1
2
3

Figure 5.11. Example *i-t* traces for 65merG:12merC, 65merG:12merA, 65merOG:12merC, 65merOG:12merA for -80 mV applied voltage (*cis* vs *trans*), for position 3 (A), position 6 (B), and position 10 (C). Data were filtered to 5 kHz post acquisition for display.

(A)

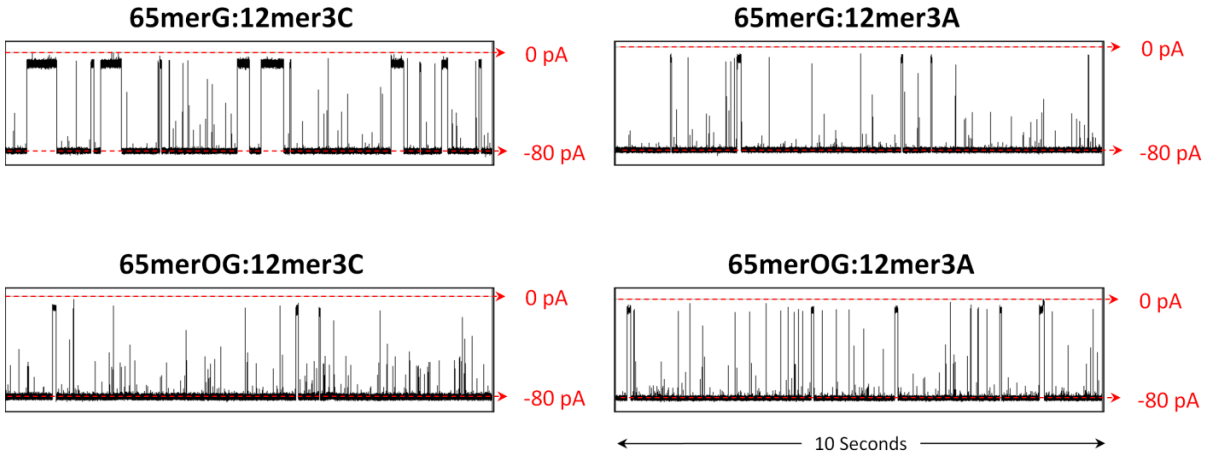
65merG:12mer3C
0 pA
-80 pA
65merG:12mer3A
0 pA
-80 pA
65merOG:12mer3C
0 pA
-80 pA
65merOG:12mer3A
0 pA
-80 pA
10 Seconds

(B)

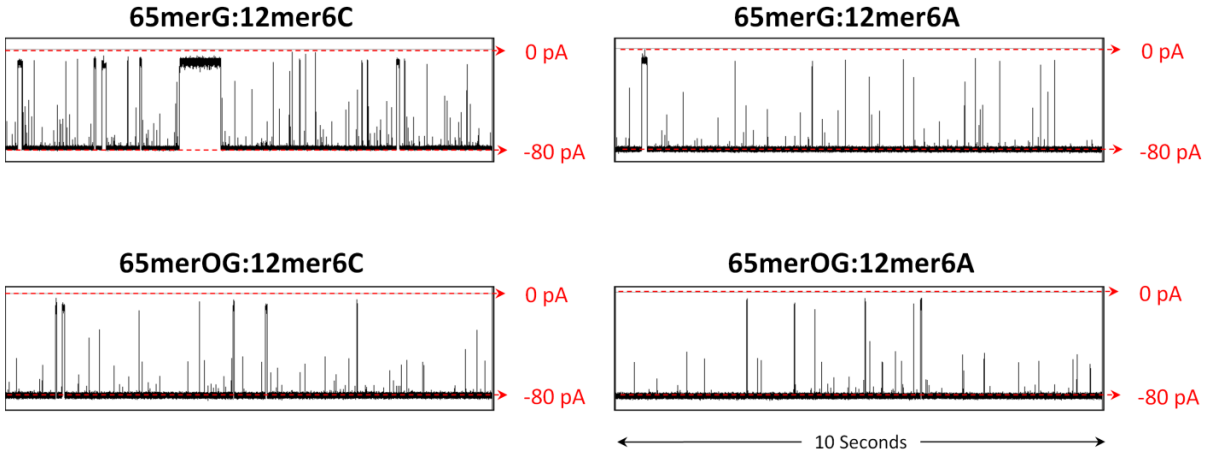
65merG:12mer6C
0 pA
-80 pA
65merG:12mer6A
0 pA
-80 pA
65merOG:12mer6C
0 pA
-80 pA
65merOG:12mer6A
0 pA
-80 pA
10 Seconds

(C)

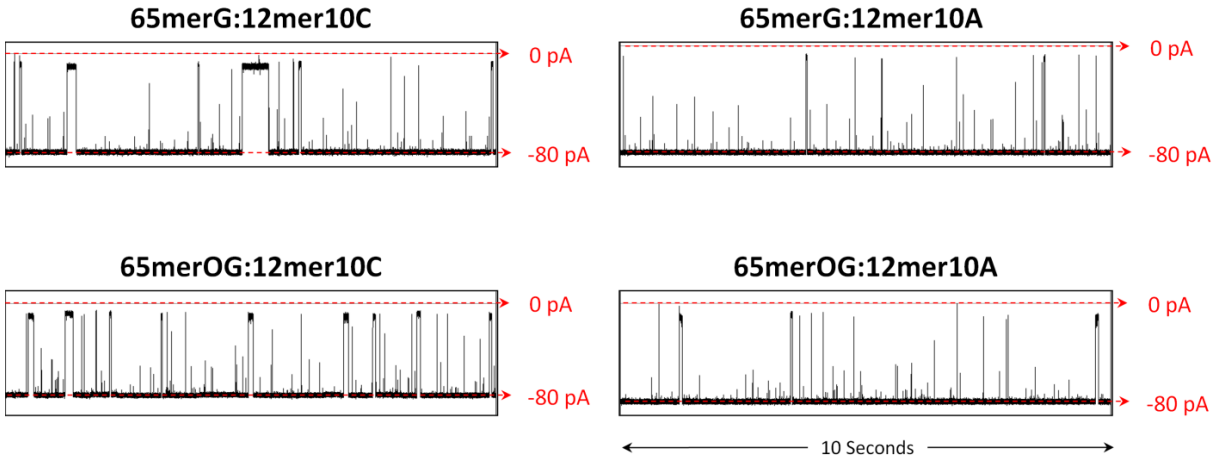
65merG:12mer10C
0 pA
-80 pA
65merG:12mer10A
0 pA
-80 pA
65merOG:12mer10C
0 pA
-80 pA
65merOG:12mer10A
0 pA
-80 pA
10 Seconds

Figure 5.12. Event duration histograms for 65merG:12merC, 65merG:12merA, 65merOG:12merC, 65merOG:12merA for -80 mV applied voltage (*cis* vs *trans*), for position 3 (A), position 6 (B), and position 10 (C).

(A)

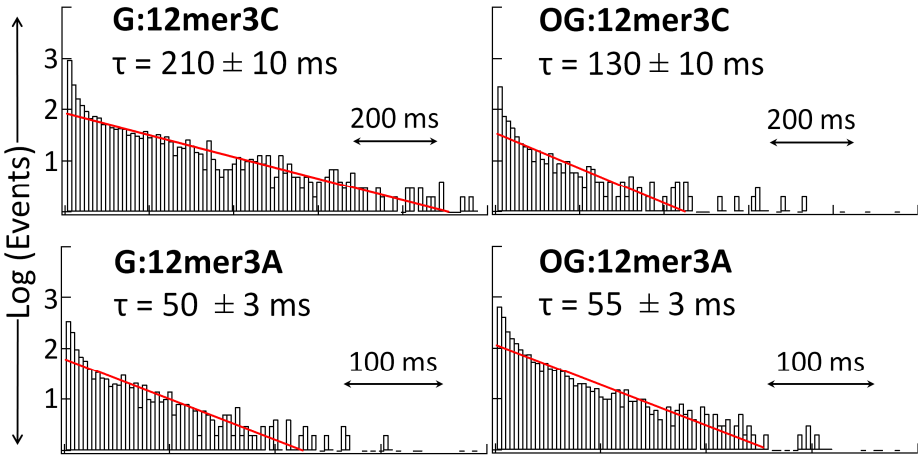
G:12mer3C
τ = 210 ± 10 ms
200 ms
OG:12mer3C
τ = 130 ± 10 ms
200 ms
G:12mer3A
τ = 50 ± 3 ms
100 ms
OG:12mer3A
τ = 55 ± 3 ms
100 ms
Log (Events)
3
2
1

(B)

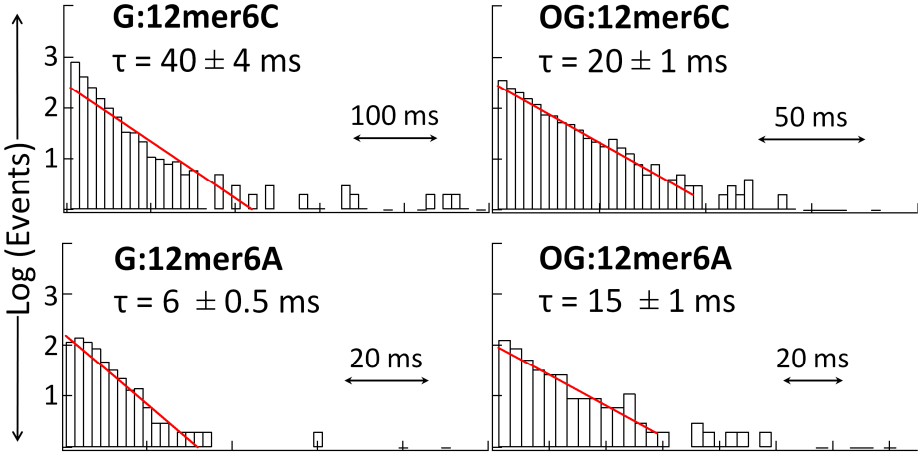
G:12mer6C
τ = 40 ± 4 ms
100 ms
OG:12mer6C
τ = 20 ± 1 ms
50 ms
G:12mer6A
τ = 6 ± 0.5 ms
20 ms
OG:12mer6A
τ = 15 ± 1 ms
20 ms
Log (Events)
3
2
1

(C)

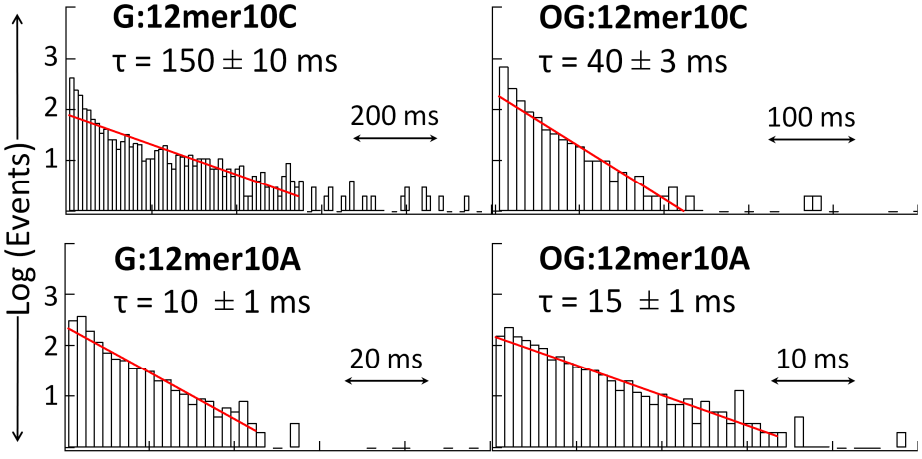
G:12mer10C
τ = 150 ± 10 ms
200 ms
OG:12mer10C
τ = 40 ± 3 ms
100 ms
G:12mer10A
τ = 10 ± 1 ms
20 ms
OG:12mer10A
τ = 15 ± 1 ms
10 ms
Log (Events)
3
2
1

Figure 5.13. Event duration histograms for (A) 65merG:12mer3C and (B) 65merG:12mer3A for $\tau_{3'}$ and $\tau_{5'}$ for -80 mV applied voltage (*cis* vs *trans*).

(A) 65merG:12mer3C

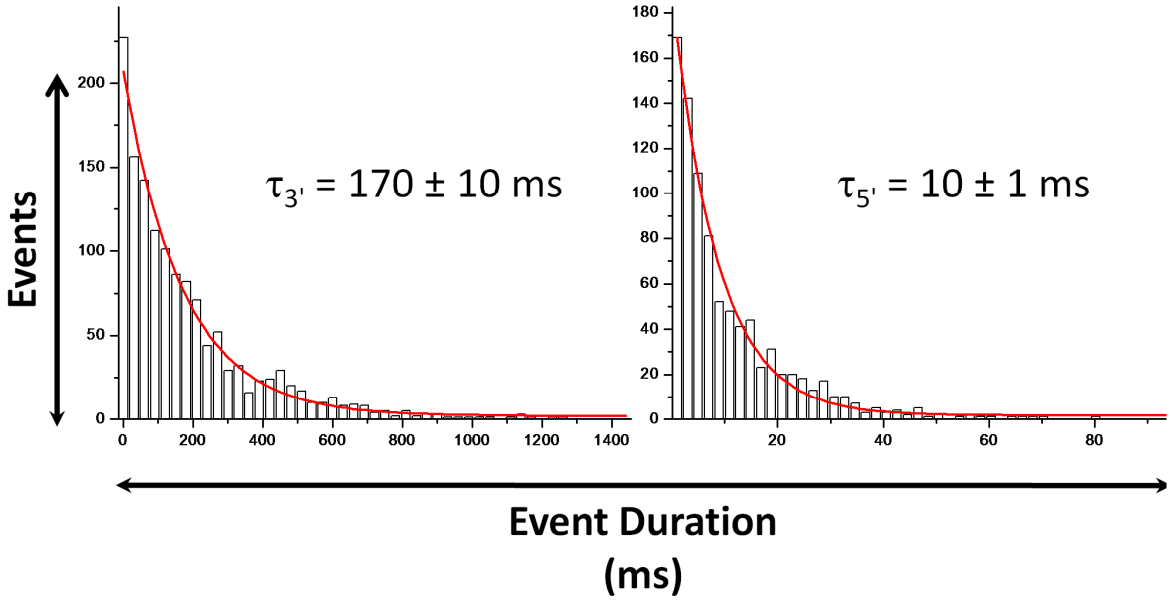

(B) 65merG:12mer3A

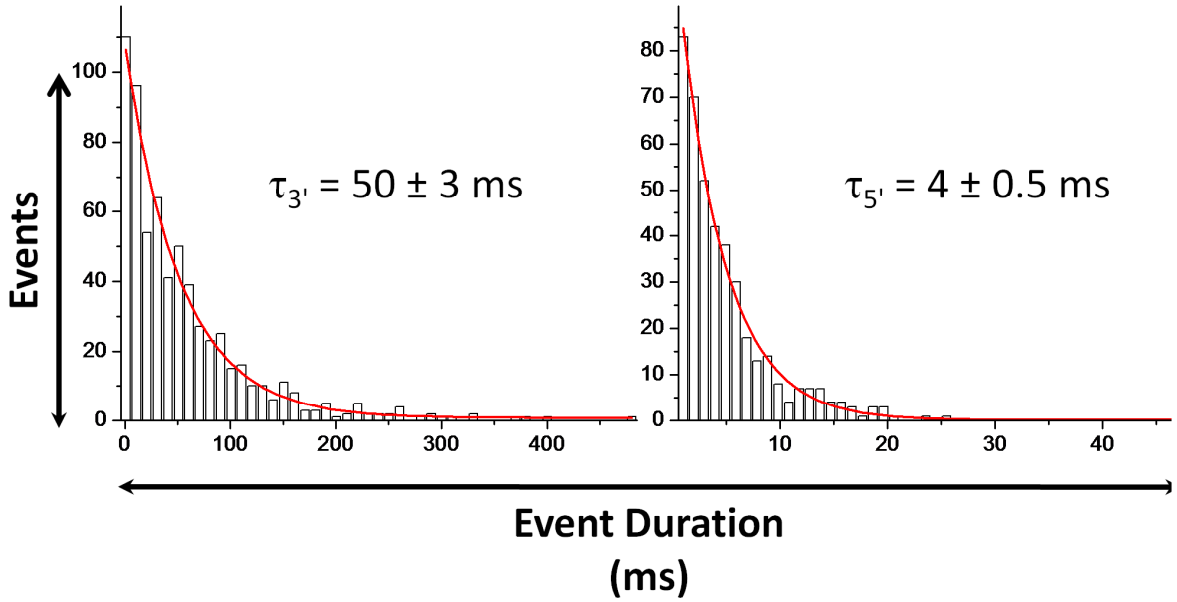

Figure 5.14. Event duration histograms for (A) 65merOG:12mer3C and (B) 65merOG:12mer3A for $\tau_{3'}$ and $\tau_{5'}$ for -80 mV applied voltage (*cis* vs *trans*).

(A) 65merOG:12mer3C

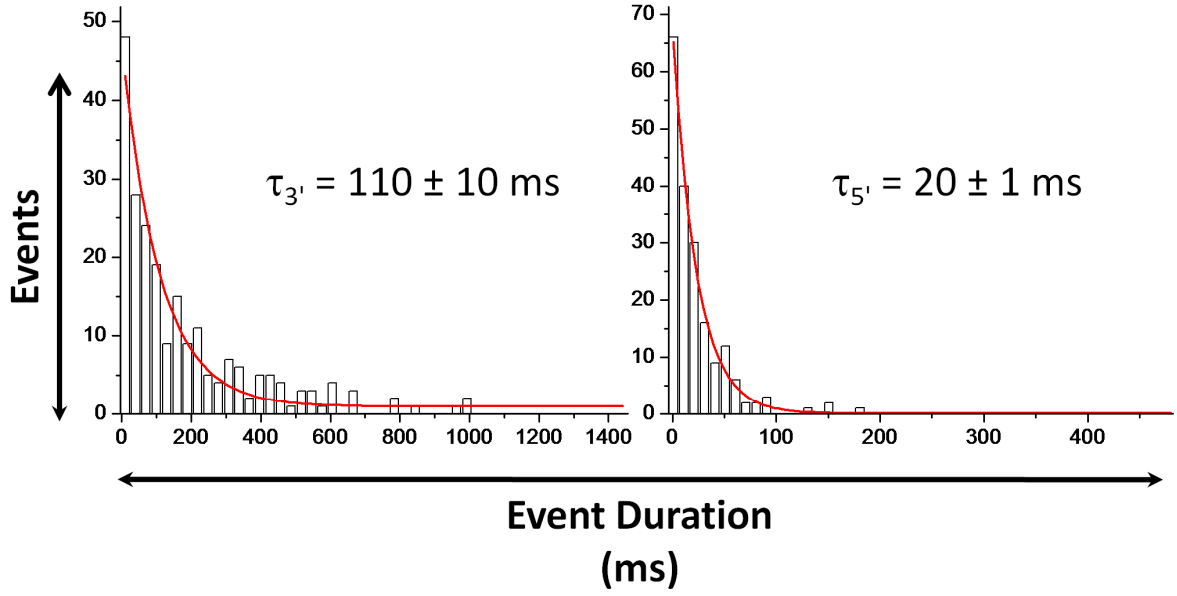

(B) 65merOG:12mer3A

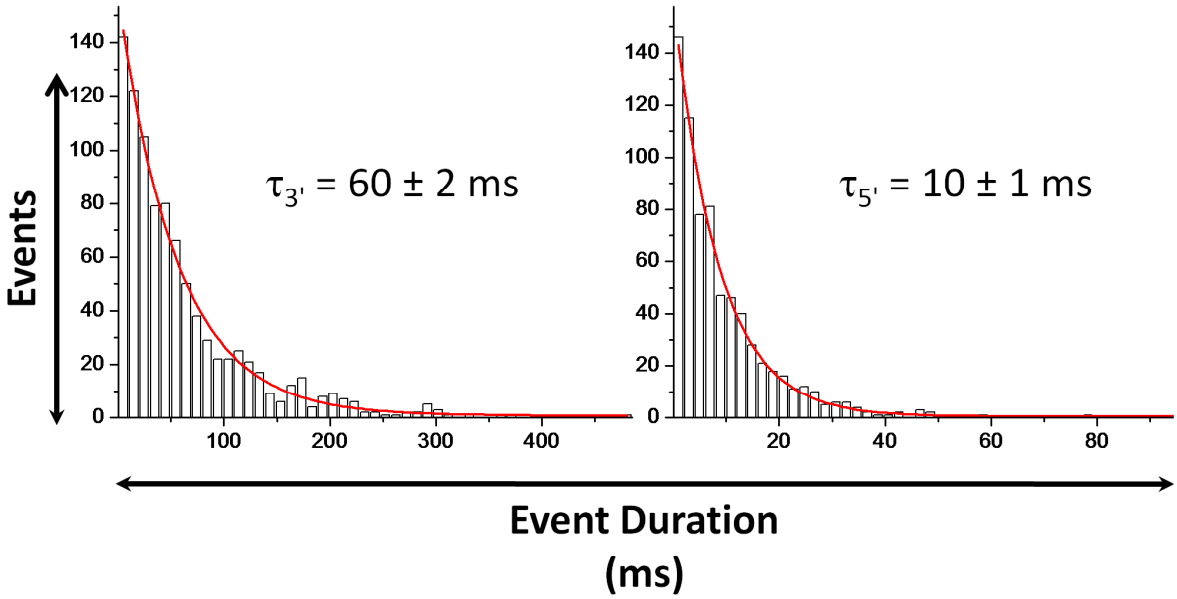

Figure 5.15. Event duration histograms for 65merG:12mer6C and 65merG:12mer6A for $\tau_{3'}$ and $\tau_{5'}$ for -80 mV applied voltage (*cis* vs *trans*).

(A) 65merG:12mer6C

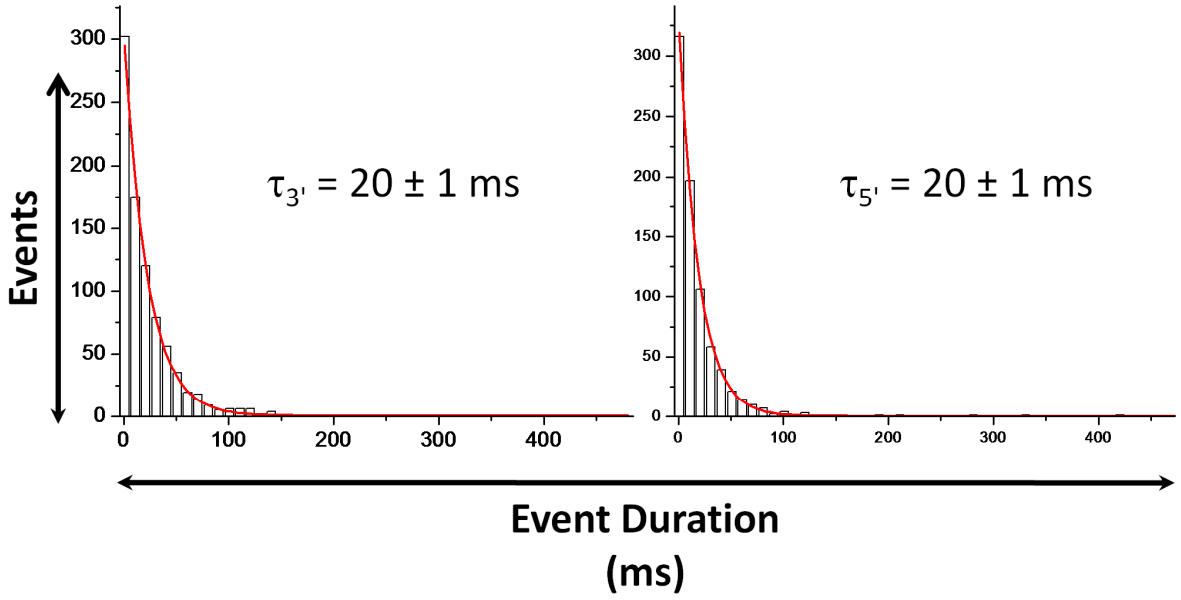

(B) 65merG:12mer6A

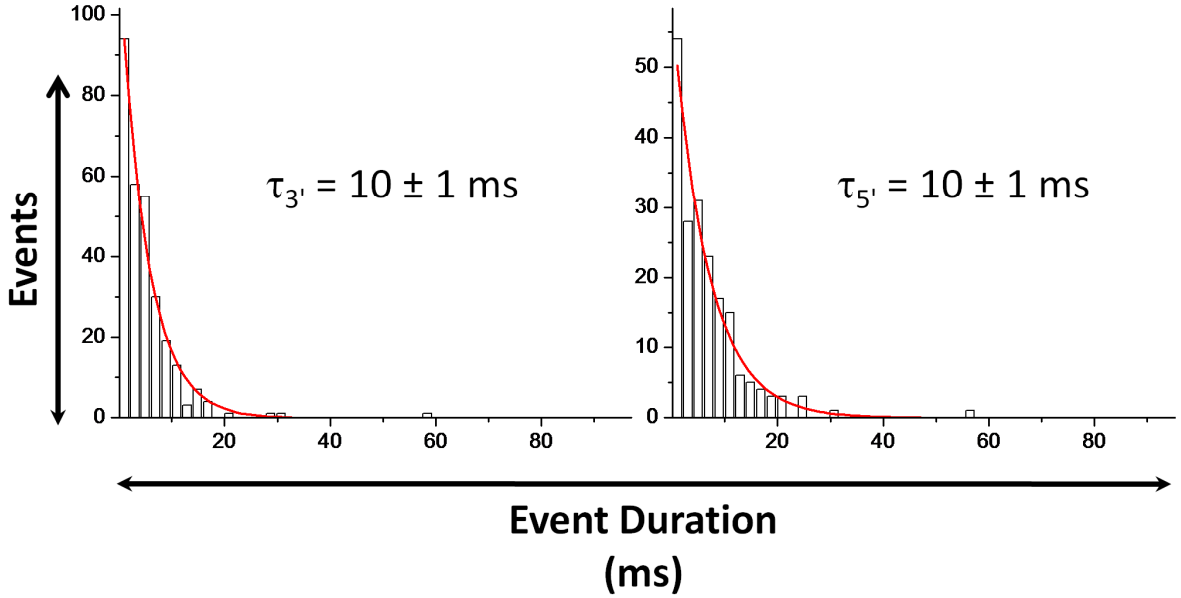

Figure 5.16. Event duration histograms for 65merG:12mer10C and 65merG:12mer10A for $\tau_{3'}$ and $\tau_{5'}$ for -80 mV applied voltage (*cis* vs *trans*).

(A) 65merG:12mer10C

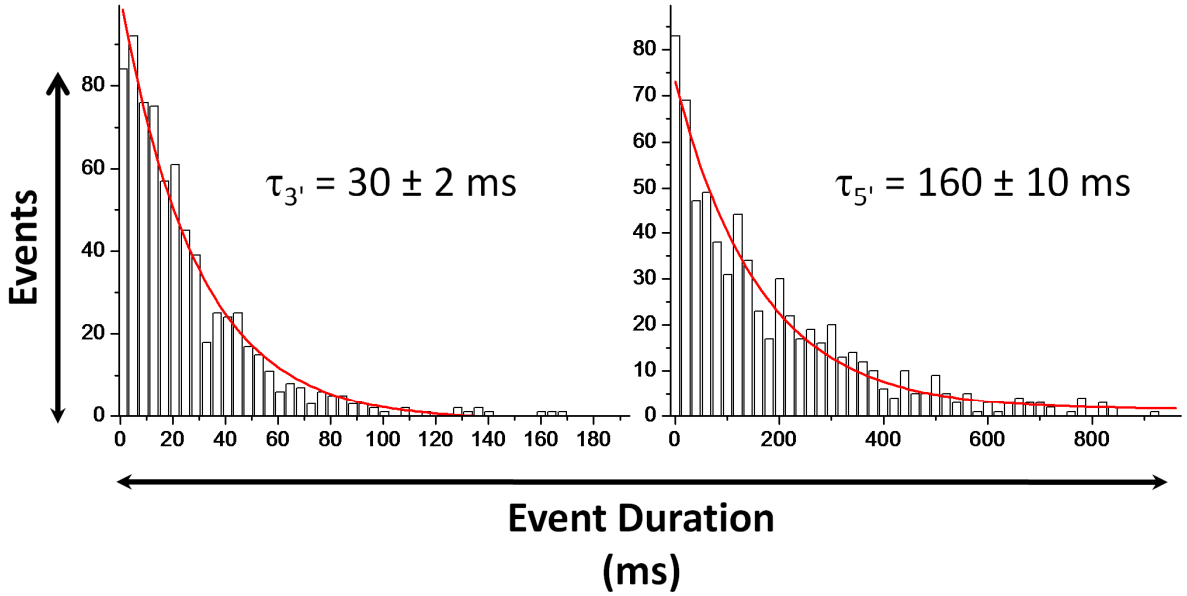

(B) 65merG:12mer10A

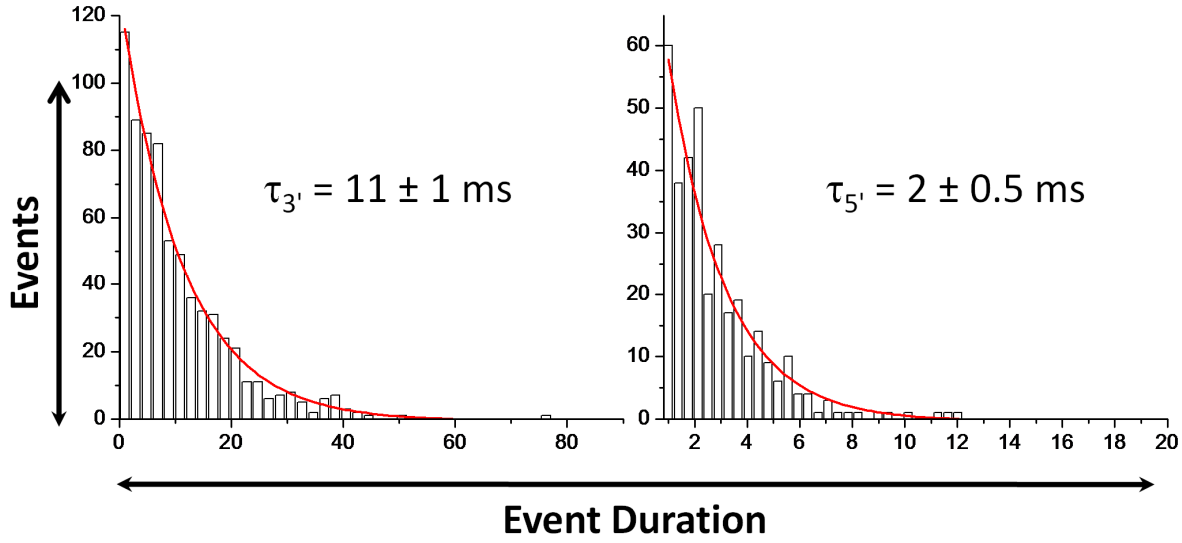

Figure 5.17. Event duration histograms for 65merOG:12mer10C and 65merOG:12mer10A for $\tau_{3'}$ and $\tau_{5'}$ for -80 mV applied voltage (*cis* vs *trans*).

(A) 65merOG:12mer10C

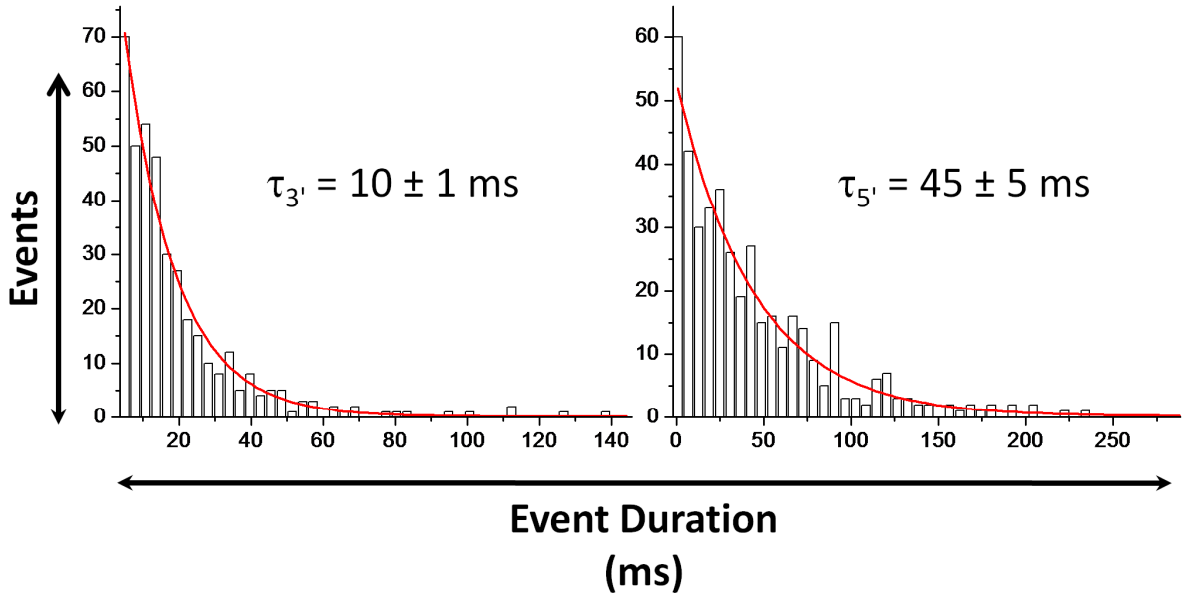

(B) 65merOG:12mer10A

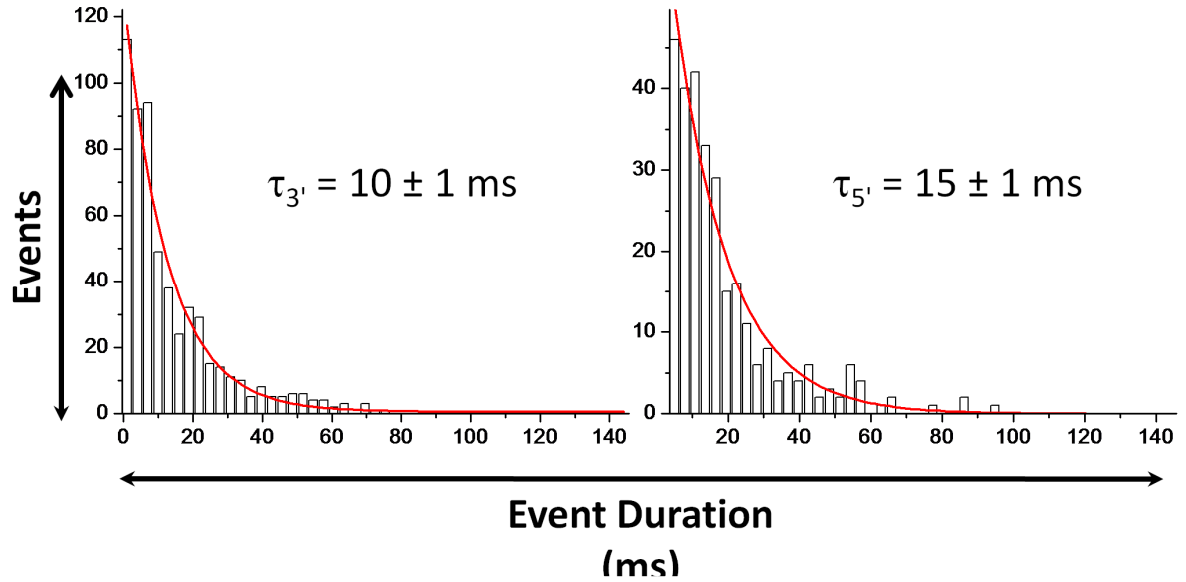

Figure 5.18. Example *i-t* trance for 65merG translocation and event duration histogram at -80 mV applied voltage (*cis* vs *trans*).

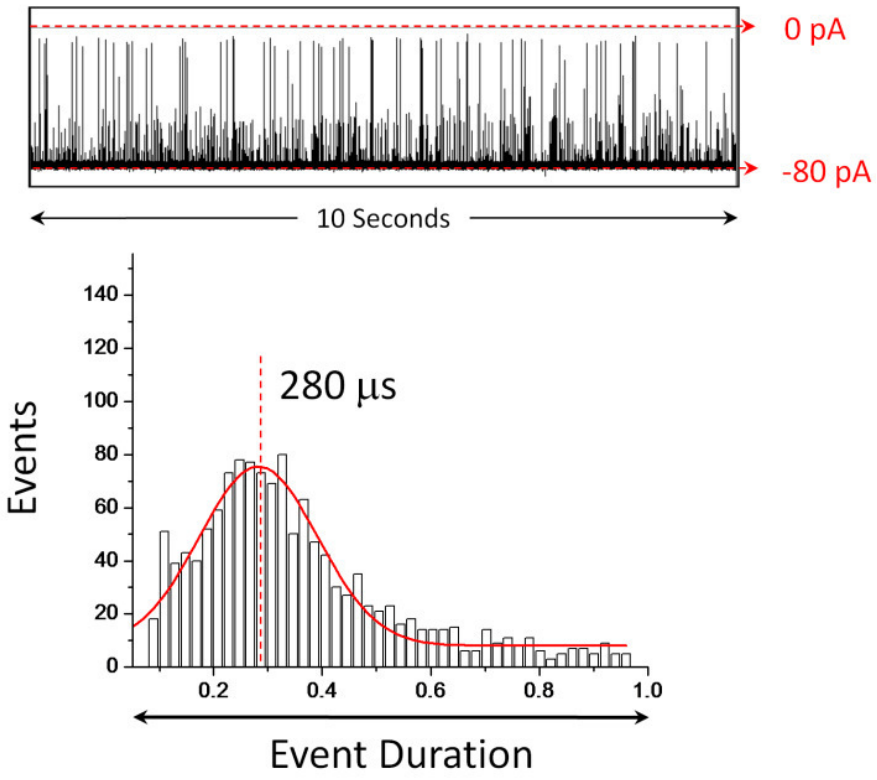
0 pA
-80 pA
10 Seconds
Events
140
120
100
80
60
40
20
0
280 µs
0.2
0.4
0.6
0.8
1.0
Event Duration

CHAPTER 6

NANOPORE DETECTION OF 8-OXO-7,8-DIHYDRO-2'-DEOXY-GUANOSINE IN IMMOBILIZED SINGLE-STRANDED DNA VIA ADDUCT FORMATION TO THE DNA DAMAGE SITE

6.1 Introduction

Oxidative stress in the cell underlies multiple age-related disorders including cancer, heart and neurological diseases.[1] Reactive oxygen species (ROS) arising from metabolism, inflammation and environmental exposure to redox-active compounds lead to oxidation of many cellular components; those reactions occurring on DNA bases are of particular concern for their mutagenic potential.[2,3] Chief among these DNA base lesions is 8-oxo-7,8-dihydroguanine (OG, Figure 6.1), an oxidized base that exists at the level of ~1 in 10^6 bases under normal cellular conditions,[4] but at much higher levels under conditions of stress or in certain disease states.[5] Present methods for detection of OG most commonly involve (1) the comet assay,[6] which can be performed on a single cell although the lesion specificity of the assay is not high, and (2) HPLC-MS/MS methods which provide a more accurate count of specific lesions such as OG, but require complete enzymatic digestion to nucleosides before analysis.[7]

Reproduced with permission from Anna E. P. Schibel, Na An, Qian Jin, Aaron M. Fleming, Cynthia J. Burrows, and Henry S. White "Nanopore Detection of 8-Oxo-7,8-dihydro-2'-deoxyguanosine in Immobilized Single-stranded DNA via Adduct Formation to the DNA Damage Site" *J. Am. Chem. Soc*. **2010**, *132*, 17992-17995.

Figure 6.1. Oxidation of the biomarker OG leads to the hydantoins Sp and Gh, depending on pH and base stacking context. The oxygen labeled "O" is incorporated from H_2O; inclusion of primary amines during oxidation leads to covalent adducts at this site.

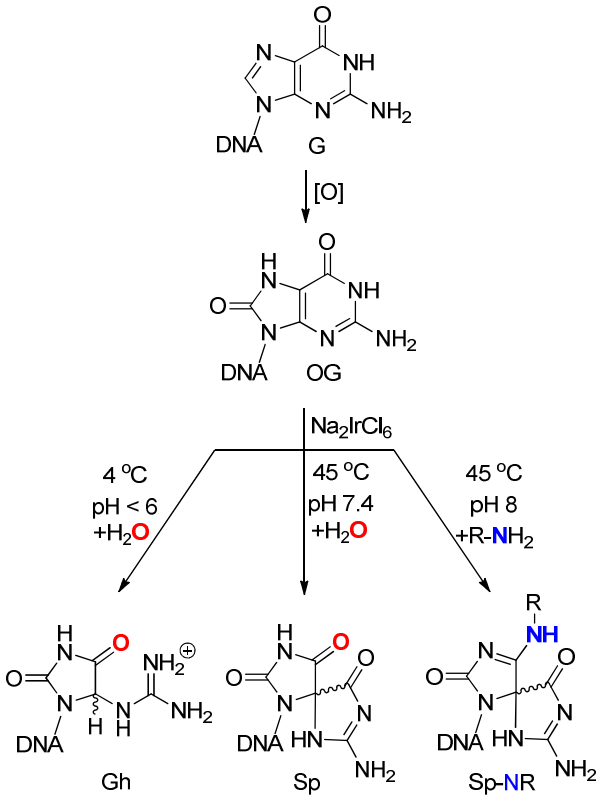
G
[O]
OG
Na2IrCl6
4 °C
pH < 6
+H2O
45 °C
pH 7.4
+H2O
45 °C
pH 8
+R-NH2
Gh
Sp
Sp-NR

Neither of these methods yield sequence information,[8] nor do they provide data on the occurrence of multiple lesions per strand, a phenomenon recognized as highly detrimental to proper DNA function.[9]

In contrast, single-molecule sequencing methods such as nanopore ion channel detection[10] offer the potential to obtain both the identity and the sequence context of base damage sites on individual DNA strands as they translocate through the ion channel. Presently this method is focused on detection of the sequence of the native DNA bases (adenine (A), thymine (T), cytosine (C), and guanine (G)), in order to provide rapid genomic sequencing.[11-17] However, sequencing methods based on translocation of DNA through ion channels, as well as solid-state pores, have proved problematic due to insufficient current resolution between the native bases.[11,13-15,18] It has previously been shown that single-stranded DNA (ssDNA) molecules can be captured and immobilized within an α-hemolysin (α-HL) ion channel by linking a biotin (Btn) molecule directly to the DNA 3' terminus and binding the DNA conjugate to streptavidin (Strep), as the streptavidin is too large to pass the α-HL channel.[19-22] As a result of this immobilization technique, the longer residence time of the DNA molecule within the α-HL channel circumvents many of the issues involved with ssDNA translocation making it possible to distinguish not only the orientation of DNA entering the pore,[19] but a single change in the native base sequence.[21-24]

The method described above should also be applicable to single-molecule sequencing of DNA damage, for which no method currently exists, but has great importance in medicinal diagnostics and in understanding the origins of diseases.

Herein, we describe the detection of a single oxidative base lesion within a background of surrounding native bases by immobilizing single-stranded DNA in an α-HL ion channel.

Because OG is similar in size and shape to the parent base G, we elected to magnify the difference between the two by taking advantage of the greatly reduced redox potential of OG compared to G (0.74 and 1.29 V. vs. NHE, respectively[25]), which results in a high reactivity of OG toward further oxidation. The mild, water-soluble oxidants ferricyanide or hexachloroiridate, oxidize OG selectively in a strand of DNA leading to hydantoin lesions, particularly spiroiminodihydantoin (Sp)[26] when the oxidation of ssDNA is carried out at pH 8.[27] When a primary amine, such as lysine or spermine (Spm), is present during oxidation, an oxidized intermediate is trapped by the nucleophilic amine generating a covalent adduct to OG as a spirocyclic adduct (Sp-NR) (Figure 6.1).[28,29]

Single oxidized base modifications, as outlined in Figure 6.1, were placed within a homopolymer poly-dC background sequence and in the K-*ras* heterosequence. Both sequences were examined for single base oxidative damage through ion channel recordings. The DNA immobilization technique, introduced by the Bayley and Schmidt laboratories,[21,22] was applied to the experiments presented here, and carried out using a wild-type α-HL ion channel reconstituted within a lipid bilayer suspended across a glass nanopore membrane.[30-32]

In the present work, we demonstrate that a simple chemical derivatization of OG to form hydantoin adducts of various sizes can lead to a nearly 10% change in the ion channel blockage current, not only for homopolymer sequences, but heterosequences as well, providing an excellent entry into the single-molecule sequencing of this oxidized lesion. To our knowledge, this is the first presentation of the ability to detect and identify singe-point base lesions within homo- and hetero-polymer native base sequences through ion channel recordings.

A single WT α-HL protein ion channel was reconstituted into a 1,2-diphytanoyl-*sn*-glycero-3-phosphocholine lipid bilayer suspended across the orifices of a glass nanopore membranes (GNM), with orifice radii between 500 and 1000 nm. The GNM provides a robust bilayer support with low electrical noise.[30-32] Because the translocation of ssDNA through α-HL is too fast for accurate single-base identification, we immobilized ssDNA oligomers within the ion channel via a tethered biotin-streptavidin (Strep-Btn) complex (Figure 6.2).[21,22]

A voltage was applied across the α-HL ion channel to electrophoretically drive the Strep-Btn DNA complex into the α-HL ion channel, where it was held for 1 to 2 s to collect current blockage event data. It was then released by reversing the voltage bias, which drives the Strep-Btn DNA into the bulk solution, restoring the open channel current. Figure 6.2 shows a typical *current-time* (*i-t*) trace for the capture of Strep-Btn-C_{40} (hereinafter termed "C_{40}"). When -120 mV was applied (*cis* vs. *trans*), an open channel current level, I_o, and current blockage

Figure 6.2. Strep-Btn-C_{40} structure, example *i-t* trace, and molecule capture/release schematic. A C_{40} ssDNA strand is tethered to a Btn molecule on the 3' end, and for strand immobilization within the α-HL channel, the Btn-DNA is bound to Strep. Schematic not drawn to scale

C_{40}-Btn:
5'- CCCCCCCCCC CCCCCCCCCC CCCCCCCCCC CCCCCCCCCC -Btn

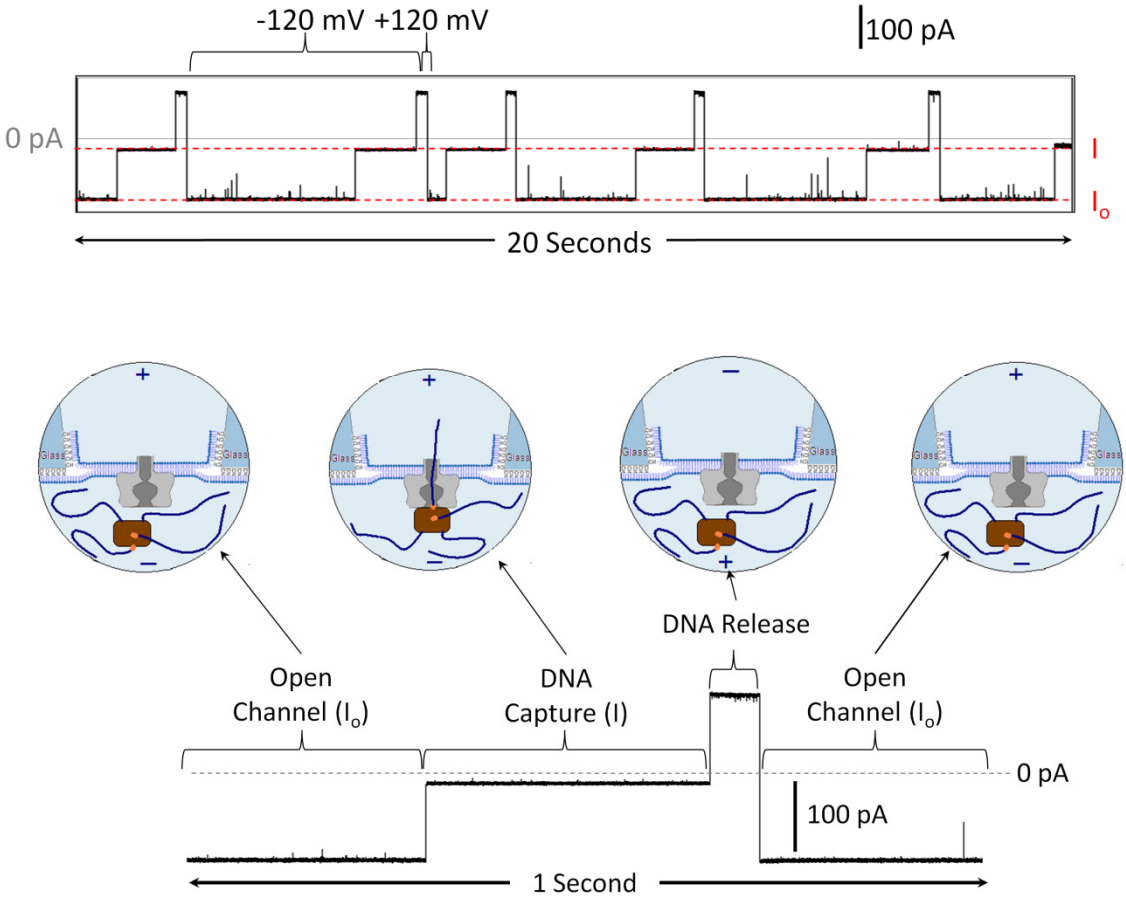

level, I, are observed when the channel is unblocked and blocked by C_{40}, respectively. This capture and release cycle was repeated to collect a population of current blockage events (>100 events) for multiple and different DNA strands within the sample of interest. The schematic in Figure 6.2 illustrates the open channel, capture, release, and open channel cycle for the Strep-Btn immobilization experiment; brief current fluctuation in the open channel current are attributed to noise and unbound single-stranded DNA. All voltages were applied *cis* vs. *trans* with respect to the α-HL channel (corresponding to external vs. internal solutions with respect to the GNM).

Previous work has shown that the native base at position 14, relative to the 3' terminus (ω14) in the DNA strand, has a particularly sensitive influence on the K^+ and Cl^- ion flux in the β-barrel sensing region of α-HL.[21] The DNA lesions under study were initially incorporated into the ω14 position of a poly-dC background with a total length of 40 nucleotides. The ion channel current blockage level of the base lesions at this position were evaluated relative to the unmodified, homopolymer sequence C_{40}.

6.2 Experimental Section

6.2.1 DNA Preparation and Purification

Gly-Pro-Arg-Pro amide, spermine, spermidine, benzylamine, D-(+)-glucosamine, Ac-Lys-OMe, and Na_2IrCl_6, were purchased from commercial suppliers and used without further purification. The 3'-biotinylated oligodeoxynucleotides (ODN) were synthesized from commercially available

phosphoramidites (Glen Research, Sterling, VA) by the DNA-Peptide Core Facility at the University of Utah. After synthesis, each ODN was cleaved from the synthetic column and deprotected according to the manufacturer's protocols, followed by purification using a semi-preparation ion-exchange HPLC column with a linear gradient of 25% to 100% B over 30 min while monitoring absorbance at 260 nm (A = 20 mM Tris, 1 M NaCl pH 7 in 10% CH_3CN/90% ddH_2O, B = 10% CH_3CN/90% ddH_2O, flow rate = 3 mL/min). The identities and purities of the ODNs were determined by negative ion electron spray (ESI^-) on a Micromass Quattro II mass spectrometer equipped with Zspray API source in the mass spectrometry laboratory at the Department of Chemistry, University of Utah.

The ODN-hydantoin/ODN-Sp-NR products were synthesized using the methodology previously established by the Burrows laboratory.[33,34,35] Briefly, the **ODN-Gh** products were produced by incubating OG-containing oligomers (10 μM, 1 nmole) in ddH_2O at 4 ^oC for 30 min; 12 equivalents of Na_2IrCl_6 (120 μM, 12 nmoles) were titrated into the ODN samples. After a 30 min incubation, the reactions were terminated with Na_2EDTA (pH 8, 1 mM, 100 nmoles). The **ODN-Sp** products were synthesized by allowing the OG-containing oligomers (10 μM, 1 nmole) in 75 mM NaP_i buffer (pH 7.4) to incubate at 45 ^oC for 30 min, followed by addition of 12 equivalents of Na_2IrCl_6 (120 μM, 12 nmoles), and Na_2EDTA (pH 8, 1 mM, 100 nmoles) was used to quench the oxidant after the reactions proceeded for 30 min.

The syntheses of **ODN-Sp-NRs** were achieved by thermally equilibrating the OG-containing oligomers (10 μM, 1 nmole) and various amines (2 mM, 200 nmoles) in 75 mM NaPi buffer (pH 8.0) at 45 ^{o}C for 30 min; then 15 equivalents of Na_2IrCl_6 (150 μM, 15 nmoles) were titrated into the samples that were then left for 30 min. The reactions were quenched the same way as previously described.

All the products were purified by an analytical ion-exchange HPLC column with a linear gradient of 25% to 100% B over 30 min while monitoring absorbance at 260 nm (A = 20 mM Tris, 1 M NaCl pH 7 in 10% CH_3CN/90% ddH_2O, B = 10% CH_3CN/90% ddH_2O, flow rate = 1 mL/min). *ODN-Sp-spermine and ODN-Sp-spermidine products were used immediately due to their instability.*[34]

6.2.2 Chemicals and Materials

Aqueous solutions mentioned below were prepared using >18 MΩ·cm ultrapure water from a Barnstead E-pure water purifier. KCl (Sigma-Aldrich), trizma base (Sigma-Aldrich), EDTA (Mallinckrodt Chemicals), and HCl (EMD) were used as received. A buffered electrolyte solution of 1.0 M KCl, 25 mM Tris-HCl, and 1.0 mM EDTA (pH 7.9) was prepared and used for all ion channel recording measurements. The buffered electrolyte solution was filtered using a sterile 0.22 μm Millipore vacuum filter (Fisher Scientific). The wild type protein channel α-hemolysin (α–HL), isolated from *Staphylococcus aureus* as a monomer, was obtained as a lyophilized powder from List Biological Laboratories and stored at concentration of 0.5 mg α–HL per mL ultra pure water in a -20 °C

freezer. Upon use, the αHL solution was diluted to a concentration of 0.05 mg α–HL per mL using the above mentioned buffered electrolyte and added directly to the experimental cell. The phospholipid 1,2-diphytanoyl-*sn*-glycero-3-phosphocholine (DPhPC) was purchased from Avanti Polar Lipids as a powder and stored in a -20 °C freezer. Upon use, the DPhPC powder was dispersed in decane (Fisher Scientific) to a concentration of 10 mg DPhPC per mL decane. Glass nanopore membranes (GNMs) were fabricated as previously described,[30,31] and before use as a bilayer support, were silanized in 2% (v:v) 3-cyanopropyldimethylchlorosilane in acetonitrile (Fisher Scientific) overnight.[32] Ag/AgCl electrodes were prepared by soaking silver wire (0.25 mm diameter, Alfa Aesar) in bleach. All DNA oligomers studied were obtained as described above, and DNA molecule binding to streptavidin was achieved by mixing DNA and streptavidin at a 4:1 ratio and incubating at room temperature for 10 min.

6.2.3 Electrical Measurements

Current-time (*i*-*t*) measurements were performed using a custom built high-impedance, low noise amplifier and data acquisition system (Electronic Bio Sciences, San Diego CA). Before use, a GNM was rinsed with ethanol and ultra pure water, and finally filled with buffered electrolyte. The GNM was positioned within the EBS DC System via a pipette holder (Dagan Corporation), where the back end was sealed to a pressure gauge and 10 mL gas-tight syringe (Hamilton). An Ag/AgCl electrode wire was positioned inside the GNM and a second Ag/AgCl electrode was positioned in the experimental cell, external to the

GNM. The same buffered electrolyte used to fill the GNM was added to the EBS DC System experimental cell, α–HL was also added to the experimental cell (external to the GNM). Voltage was applied across the GNM orifice, *cis* vs. *trans* with respect to the α–HL channel, and external vs. internal with respect to the GNM, and the resultant current was measured as a function of time.

Suspended bilayers were generated through painting. To form a suspended bilayer, a plastic pipette tip (gel-loading tips, flat, 1-200 μL, 0.4 mm) was filled with lipid solution and gently pulled across the GNM face, over the orifice. The establishment of a bilayer was confirmed by observing a drop in conductance as voltage was applied across the GNM orifice; an open pore has a resistance of approximately 10 MΩ, while a bilayer suspended across a GNM exhibits a resistance of around 100 GΩ.[32] After bilayer formation, a pressure was applied to the back of the GNM for protein channel reconstitution to occur.[32] Strep-Btn DNA was added to the cell in 100-200 nM increments. DNA was captured and held using an applied voltage of -120 mV (*cis* vs. *trans*), and released by reversing the bias. The modified sample of interest was added to the experimental cell first, and after an adequate number of blockage events are collected, a second control sample, Strep-Btn C_{40}, was added to the cell to provide a reference position. Data were collected with a 10 kHz low pass filter, and 50 kHz data acquisition rate.

6.2.4 Data Analysis

Only capture events longer than 1 second were included in data analysis. All event current blockage values (I) were normalized by the immediately preceding open channel current (I_o), and expressed as $\%I/I_o$. The Strep-Btn C_{40} $\%I/I_o$ peak position was set as the reference position 0. $\%I/I_o$ for all other molecules is reported relative to Strep-Btn C_{40}; more blocking $\%I/I_o$ values are negative relative to Strep-Btn C_{40} and less blocking $\%I/I_o$ values are positive relative to Strep-Btn C_{40}.

6.3 Results and Discussion

6.3.1 Oxidative Damage Detection

Our initial efforts focused on defining the electrical signature of a single oxidized guanine lesion suspended within the α-HL channel. Figure 6.3 shows histograms of the percent blockage current when G at position ω14, in a poly-dC background, was substituted by OG or by the further oxidation products Sp or Gh (guanidinohydantoin). C_{40} was used as a reference and current blockage for all molecules is reported referenced to the blockage level of C_{40}, which is assigned a value of $\%I/I_o = 0$; all experiments were reproduced at least once, and peak positions relative to C_{40} are consistent in position (within 0.1%). In the poly-dC sequence context, G is about 1.2% less blocking than C, and OG yields an electrical signature nearly identical to G. The hydantoin products Sp and Gh are shifted from G and OG, and display broader histograms possibly due to the formation of diastereomeric pairs for each of these products as well as multiple

Figure 6.3. Current blockage histograms comparing guanine (G), 8-oxo-7,8-dihydroguanine (OG), spiroiminodihydantoin (Sp), and guanidinohydantoin (Gh) at position ω14 relative to C_{40}. All oxidation products are within a poly-dC background, $C_{39}X_{\omega 14}$. C_{40} is used as a reference sample; the % I/I_o for C_{40} was set equal to 0 and % I/I_o for all other samples is relative to C_{40}.

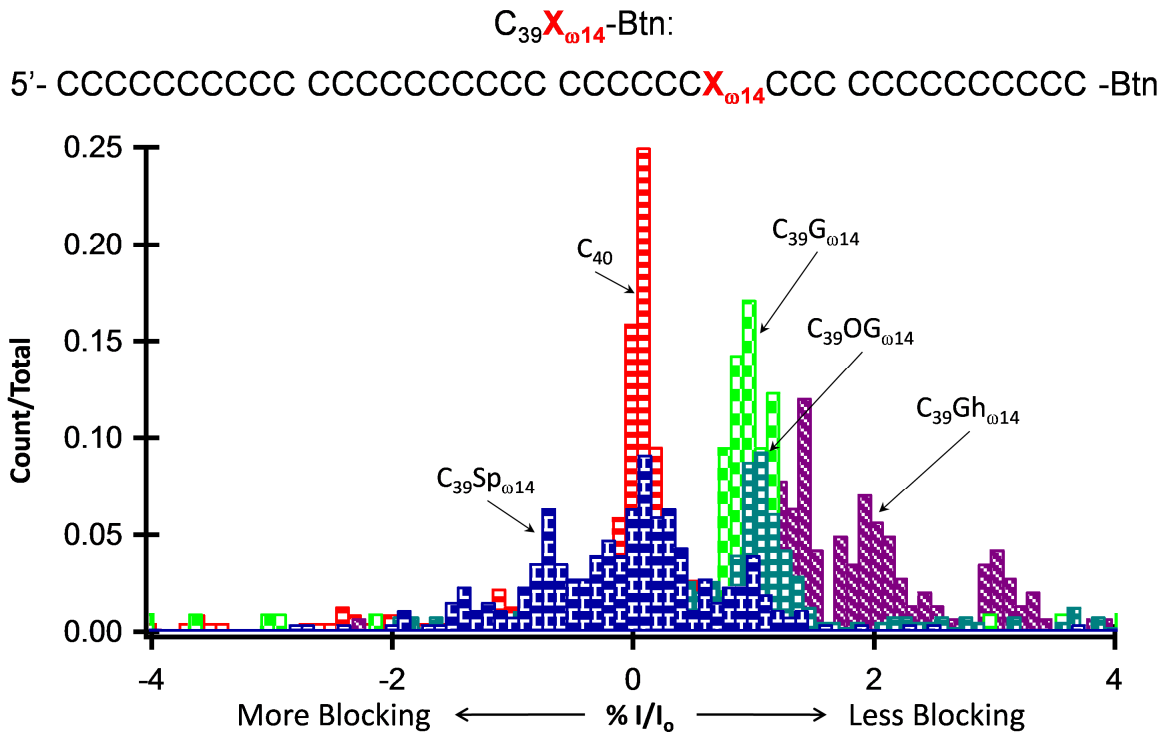
C39Xω14-Btn:
5'- CCCCCCCCCC CCCCCCCCCC CCCCCCXω14CCC CCCCCCCCCC -Btn
0.25
0.20
0.15
0.10
0.05
0.00
Count/Total
C40
C39Gω14
C39OGω14
C39Ghω14
C39Spω14
-4
-2
0
2
4
More Blocking
% I/Io
Less Blocking

conformations that might exist due to poor base stacking of hydantoins compared to normal bases.

6.3.2 Oxidative Damage Detection via Adduct Formation

Although the oxidative lesions OG, Sp, and Gh give current blockage signatures significantly different from the native G base, we hypothesized that even larger spirocyclic adducts (Sp-X) created by the oxidation of OG in the presence of a primary amine (Figure 6.1) would modulate the ion channel current to an even larger extent. The amines selected to form adducts were chosen to modify the size and geometry of the DNA strand at position ω14.

Amine adducts introduced at position ω14 within the poly-dC background, $C_{39}X_{\omega 14}$, included: benzylamine (Bz), lysine (Lys), glucosamine (GlcN), spermidine (Spd), spermine (Spm), and Gly-Pro-Arg-Pro amide (GPRP). Figure 6.4 shows the structures for the spirocyclic adducts mentioned above and the $\%I/I_o$ histograms relative to C_{40}. The $C_{39}Spd_{\omega 14}$ and $C_{39}Spm_{\omega 14}$ adducts are long, linear, and flexible adducts, and both produce multiple, more blocking $\%I/I_o$ peaks compared with $C_{39}G_{\omega 14}$, blocking up to 5% and 7% more current, respectively; Spm being the larger adduct compared with Spd, produced the deepest current blockades. $C_{39}Lys_{\omega 14}$ produced multiple current blockage levels, with $\%I/I_o$ peaks spread over a large range, roughly 1-5% more blocking than $C_{39}G_{\omega 14}$, with a prominent peak on top of C_{40}. The $C_{39}Lys_{\omega 14}$ peak that is approximately 1% more blocking than $C_{39}G_{\omega 14}$, has a similar $\%I/I_o$ peak position and distribution to $C_{39}Sp_{\omega 14}$ (Figure 6.3), and is possibly a result of Lys having

Figure 6.4. $\%I/I_o$ histograms comparing benzylamine (Bz), lysine (Lys), glucosamine (GlcN), spermidine (Spd), spermine (Spm), and Gly-Pro-Arg-Pro amide (GPRP) adducts at position $\omega 14$ relative to C_{40}. All adducts are within a poly-dC background, $C_{39}X_{\omega 14}$. C_{40} was used as a reference sample; the $\%I/I_o$ for C_{40} was set equal to 0, and $\%I/I_o$ for all other samples is relative to C_{40}.

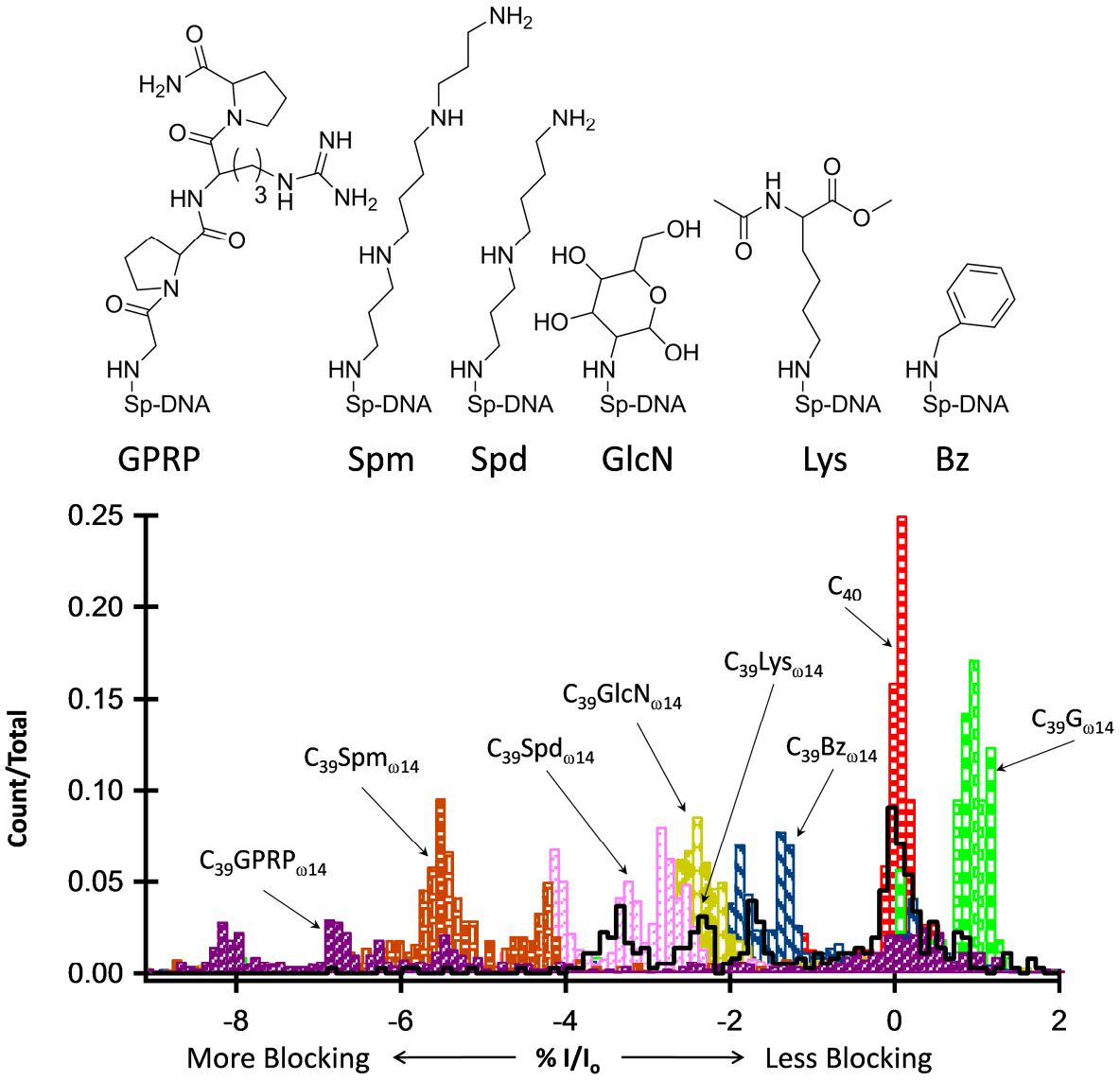
GPRP
Spm
Spd
GlcN
Lys
Bz
Sp-DNA
Count/Total
0.25
0.20
0.15
0.10
0.05
0.00
C40
C39Lysω14
C39GlcNω14
C39Gω14
C39Spdω14
C39Bzω14
C39Spmω14
C39GPRPω14
-8
-6
-4
-2
0
2
More Blocking
% I/Io
Less Blocking

been hydrolyzed to Sp. The bulky spirocyclic adducts produced the most variable current blockage signals. For example, $C_{39}Bz_{\omega 14}$, $C_{39}GlcN_{\omega 14}$, and $C_{39}GPRP_{\omega 14}$, all resulted in deeper current blockades compared with $C_{39}G_{\omega 14}$, and all produced signals with a broad distribution of current blockage levels and noise amplitudes. The various current blockage levels and noise amplitudes are thought to be associated with cyclic adducts adopting different conformations within the α-HL channel.

$C_{39}Bz_{\omega 14}$ and $C_{39}GlcN_{\omega 14}$ produced an approximately 3 and 4% negative shift in $\%I/I_o$, respectively, relative to $C_{39}G_{\omega 14}$. The $C_{39}GPRP_{\omega 14}$ adduct produced events with the deepest current blockades, up to 10% compared with $C_{39}G_{\omega 14}$, but the distribution was very broad and contained a prominent population of events with current blockage levels similar to that of C_{40}. This is interpreted to suggest the molecule is not readily entering the sensing regions of the channel, resulting in a current blockage signal arising from the surrounding poly-dC sequence. To further test the ability to detect oxidative damage within a natural DNA sequence, base modifications were examined within an immobilized heterosequence.

6.3.3 Oxidative Damage Detection in a Heterosequece

The oxidatively damaged species OG, Sp, and Gh, as well as the spermine adduct to OG (Spm) were selected for immobilization studies within a heterosequence background to determine the extent to which a DNA damage site can be detected in a sequence of biological relevance. These lesions permit

the study of primary DNA damage products as well as a simple adduct to OG (Spm), all of which produced strong $\%I/I_o$ peaks rather than a dispersed population of blockage currents. The heterosequence selected for study was a portion of the K-*ras* gene near codon 12 embedded in a poly-dT background while maintaining the 40-mer length (Figure 6.5). A poly-dT background is used to avoid secondary structures which occur as the poly-dC interacts with the G-rich K-*ras* sequence. Point mutations within codon 12 of the K-*ras* proto-oncogene have been shown to cause uncontrolled cell growth and loss of cell differentiation, leading to various human adenocarcinomas.[36]

Specifically, in lung cancer, the K-*ras* gene predominantly undergoes a G → T transversion mutation (GGT → GTT) that could result from the failure to repair guanine oxidative damage before replication.[36,37] Thus, we positioned the K-ras sequence within the α-HL channel in such a way that the central G of codon 12, or its oxidized derivatives, was located at the ω14 position. Results for detecting the native gene sequence (K-*ras*-$G_{\omega 14}$), oxidation products OG (K-*ras*-$OG_{\omega 14}$), Sp (K-*ras*-$Sp_{\omega 14}$), and Gh (K-*ras*-$Gh_{\omega 14}$), as well as the Spm adduct (K-*ras*-$Spm_{\omega 14}$), are displayed in Figure 6.5.

When comparing the $\%I/I_o$ peaks for modifications within the poly-dC background against the K-*ras* sequence, it is apparent that the surrounding sequence has a profound influence on the current signature and event population distribution. Specifically, K-*ras*-$G_{\omega 14}$ and *K-ras*-$OG_{\omega 14}$ produced $\%I/I_o$ peaks separated by approximately 1% from each other, with the K-*ras*-$G_{\omega 14}$ producing the lesser blockage. Whereas G and OG produced overlapping histograms

Figure 6.5. $\%I/I_o$ histograms for G, OG, Sp, Gh, and Spm base modifications at position ω14 relative to C_{40}. All adducts are within a poly-dT background, Btn-K-*ras*-$X_{\omega 14}$. C_{40} was used as a reference sample; the $\%I/I_o$ for C_{40} was set equal to 0, and $\%I/I_o$ for all other samples was relative to C_{40}. The $\%I/I_o$ peak positions relative to C_{40} and among modified DNA molecules have shifted blocking order compared with modifications within a homopolymer background, indicating that the current blockage level is not only influenced by the modification itself, but also the surrounding sequence.

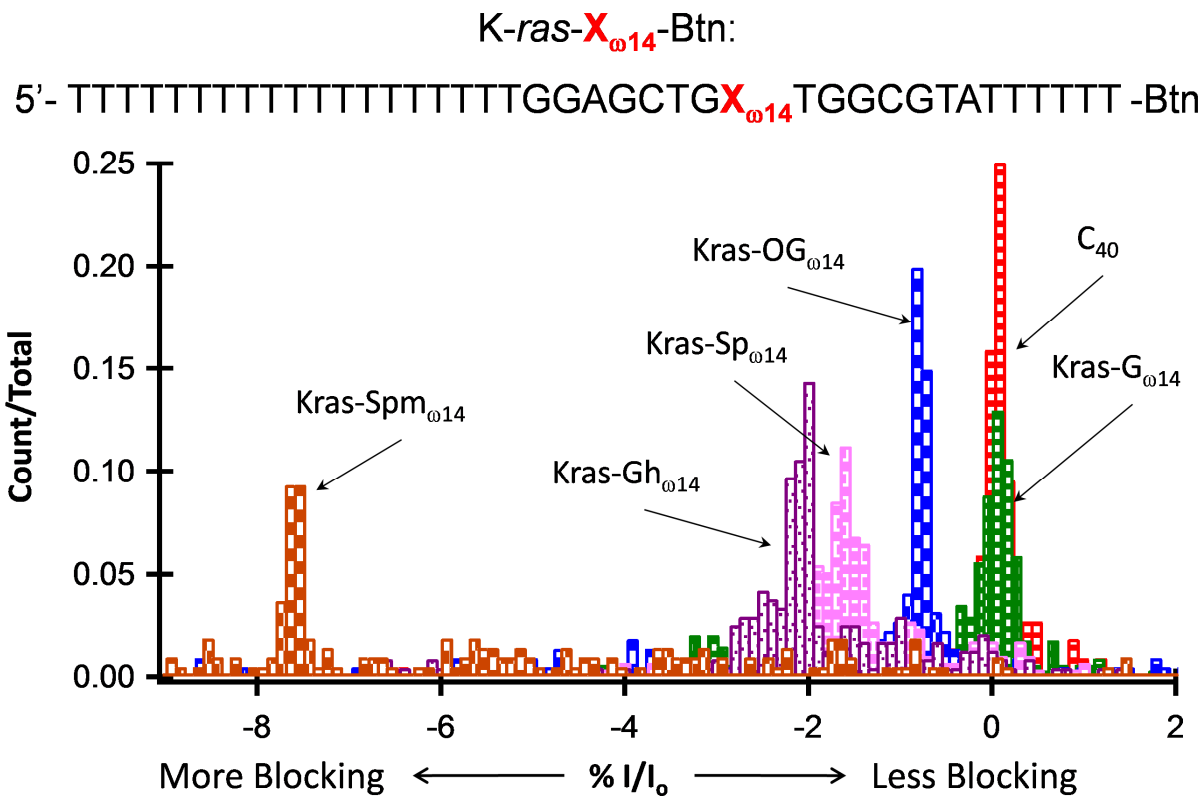
K-ras-X ω14 -Btn:
5'- TTTTTTTTTTTTTTTTTTTTGGAGCTGX ω14 TGGCGTATTTTTT -Btn
Count/Total
0.25
0.20
0.15
0.10
0.05
0.00
Kras-Spm ω14
Kras-Gh ω14
Kras-Sp ω14
Kras-OG ω14
C 40
Kras-G ω14
-8
-6
-4
-2
0
2
More Blocking
% I/I o
Less Blocking

in the C_{40} background, their signatures are quite distinct and show narrower distributions in the K-*ras* sequence. K-*ras*-$Sp_{\omega 14}$ resulted in a single, strong $\%I/I_o$ peak, approximately 1.5% more blocking than K-*ras*-$G_{\omega 14}$ and again distinct from the OG signal; in the poly-dC background the Sp oxidation product produced a dispersed population of current blockage levels yielding multiple $\%I/I_o$ peaks with positions similar to C_{40}, $C_{39}G_{\omega 14}$, and $C_{39}OG_{\omega 14}$. The K-*ras*-$Gh_{\omega 14}$ sample produced the greatest change from its $C_{39}Gh_{\omega 14}$ analog; K-*ras*-$Gh_{\omega 14}$ has a single $\%I/I_o$ peak approximately 2% more blocking compared with K-*ras*-$G_{\omega 14}$. In the poly-dC background the Gh oxidation product yielded multiple $\%I/I_o$ peaks that are 0.5-2% less blocking than $C_{39}G_{\omega 14}$.

Although $\%I/I_o$ peak position, dispersion, and relative amplitude are sequence dependent, if the structural modification is large enough, the current blockade from the modification will dominate the influence from the surrounding sequence. The spermine adduct now proves to be such a modification as it consistently produced a more blocking $\%I/I_o$ peak shift of around 8% relative to the unmodified sequence in both the K-*ras* and poly-dC backgrounds. Overall, $\%I/I_o$ peaks appear sharper and less dispersed for oxidation products and adducts within the K-*ras* sequence than when present in the poly-dC background.

6.4 Conclusions

The immobilization studies presented above are preliminary experiments toward translocation studies; it will be necessary to examine the most blocking adducts for the ability to readily pass through the constriction of α-HL and translocate the pore. It was previously demonstrated by the Howorka laboratory that peptide tags can be used to change the current blockage amplitude and event duration of translocating DNA strands,[38,39] and by the same principle, manipulating the size, geometry, and electrical characteristics of the DNA damage site should lead to detection via nanopore translocation.

These initial studies have shown the power of ion channel recordings for the detection of DNA damage and highlighted the ability to detect a single lesion within both homo- and hetero-polymer DNA sequences. We have taken a first step toward damage detection through ion channel recording translocation experiments. In addition to being able to detect DNA damage, this work has introduced many options for being able to identify the damage as each adduct produced a unique current blockage level and/or population distribution and noise signature, with a general trend of larger adducts producing the most blocking current blockage levels.

6.5 References

(1) Cooke, M. S.; Olinski, R.; Evans, M. D. *Clinica Chimica Acta* **2006**, *365*, 30-49.

(2) Cadet, J.; Douki, T.; Ravanat, J.-L. *Free Radic. Biol. Med.* **2010**, *49*, 9-21.

(3) Delaney, J. C.; Essigmann, J. M. *Chem. Res. Toxicol.* **2008**, *21*, 232-252.

(4) Gedik, C. M.; Collins, A. *FASEB Journal* **2005**, *19*, 82-84.

(5) Mangal, D.; Vudathala, D.; Park, J.-H.; Lee, S. H.; Penning, T. M.; Blair, I. A. *Chem. Res. Toxicol.* **2009**, *22*, 788-797.

(6) Azqueta, A.; Shaposhnikov, S.; Collins, A. R. *Mutat. Res.* **2009**, *674*, 101-108.

(7) Cadet, J.; Poulsen, H. *Free Radic. Biol. Med.* **2010**, *48*, 1457-1459.

(8) Muller, J. G.; Duarte, V.; Hickerson, R. P.; Burrows, C. J. *Nucleic Acids Res.* **1998**, *26*, 2247-2249.

(9) Hada, M.; Sutherland, B. M. *Radiat. Res.* **2006**, *165*, 223-230.

(10) Branton, D.; Deamer, D. W.; Marziali, A.; Bayley, H.; Benner, S. A.; Butler, T.; Di Ventra, M.; Garaj, S.; Hibbs, A.; Huang, X.; Jovanovich, S. B.; Krstic, P. S.; Lindsay, S.; Ling, X. S.; Mastrangelo, C. H.; Meller, A.; Oliver, J. S.; Pershin, Y. V.; Ramsey, J. M.; Riehn, R.; Soni, G. V.; Tabard-Cossa, V.; Wanunu, M.; Wiggin, M.; Schloss, J. A. *Nat. Biotech.* **2008**, *26*, 1146-1153.

(11) Kasianowicz, J. J.; Brandin, E.; Branton, D.; Deamer, D. W. *Proc. Natl. Acad. Sci.* **1996**, *93*, 13770-13773.

(12) Akeson, M.; Branton, D.; Kasianowicz, J. J.; Brandin, E.; Deamer, D. *Biophys J.* **1999**, *77*, 3227-3233.

(13) Meller, A.; Nivon, L.; Brandin, E.; Golovchenko, J.; Branton, D. *Proc. Natl. Acad. Sci.* **2000**, *97*, 1079-1084.

(14) Deamer, D. W.; Branton, D. *Acc. Chem. Res.* **2002**, *35*, 817-825.

(15) Fologea, D.; Gershow, M.; Ledden, B.; McNabb, S. D.; Golovchenko, J. A.; Li, J. *Nano Lett.* **2005**, *5*, 1905-1909.

(16) Astier, Y.; Braha, O.; Bayley, H. *J. Am. Chem. Soc.* **2006**, *128*, 1705-1710.

(17) Clarke, J.; Wu, H.-C.; Jayasinghe, L.; Patel, A.; Reid, S.; Bayley, H. *Nature Nanotech.* **2009**, *4*, 265-270.

(18) Meller, A.; Nivon, L.; Branton, D. *Phys. Rev. Lett.* **2001**, *86*, 3435-3438.

(19) Nakane, J.; Wiggin, M.; Marziali, A. *Biophys. J.* **2004**, *87*, 615-621.

(20) Purnell, R. F.; Mehta, K. K.; Schmidt, J. J. *Nano Lett.* **2008**, *8*, 3029-3034.

(21) Stoddart, D.; Heron, A. J.; Mikhailova, E.; Maglia, G.; Bayley, H. *Proc. Natl. Acad. Sci.* **2009**, *106*, 7702-7707.

(22) Purnell, R. F.; Schmidt, J. J. *ACS Nano* **2009**, *9*, 2533-2538.

(23) Stoddart, D.; Maglia, G.; Mikhailova, E.; Heron, A. J.; Bayley, H. *Angew. Chem. Int. Ed.* **2009**, *48*, 1-5.

(24) Wallace, E. V. B.; Stoddart, D.; Heron, A. J.; Mikhailova, E.; Maglia, G.; Donohoe, T. J.; Bayley, H. Identification of Epigenetic DNA Modifications with a Protein Nanopore. *Chem. Commun.* [Online early access]. DOI:10.1039/c0cc02864a. Published Online: October 6, 2010.

http://pubs.rsc.org (accessed October 19, 2010)

(25) Steenken, S.; Jovanovic, S. V.; Bietti, M.; Bernhard, K. *J. Am. Chem. Soc.* **2000**, *122*, 2372-2374.

(26) Luo, W.; Muller, J. G.; Rachlin, E. M.; Burrows, C. J. *Org. Lett.* **2000**, *2*, 613-617.

(27) Kornyushyna, O.; Berges, A. M.; Muller, J. G.; Burrows, C. J. *Biochemistry* **2002**, *41*, 15304-15314.

(28) Hosford, M. E.; Muller, J. G.; Burrows, C. J. J*. Am. Chem. Soc.* **2004**, *126*, 9540-9541.

(29) Xu, X.; Muller, J. G.; Ye, Y.; Burrows, C. J. *J. Am. Chem. Soc.* **2008**, *130*, 703-709.

(30) Zhang, G.; Zhang, Y.; White, H. S. *Anal. Chem.* **2004**, *76*, 6229-6238.

(31) Zhang, B.; Galusha, J.; Shiozawa, P. G.; Wang, G.; Bergren, A. J.; Jones, R. M.; White, R. J.; Ervin, E. N.; Cauley, C. C.; White, H. S. *Anal. Chem.* **2007**, *79*, 4778-4787.

(32) White, R. J.; Ervin, E. N.; Yang, T.; Chen, X.; Daniel, S.; Cremer, P. S.; White, H. S. *J. Am. Chem. Soc.* **2007**, *129*, 11766-00775.

(33) Kornyushyna, O.; Berges, A. M.; Muller, J. G.; Burrows, C. J. In vitro nucleotide misinsertion opposite the oxidized guanosine lesions spiroiminodihydantoin and guanidinohydantoin and DNA synthesis past the lesions using Escherichia coli DNA polymerases I (Klenow Fragment). *Biochemistry* **2002,** 41, 15304-15314.

(34) Hosford, M. E.; Muller, J. G.; Burrows, C. J. Spermine participates in oxidative damage of guanosine and 8-oxoguanosine leading to deoxyribosylurea formation. *J. Am. Chem. Soc* **2004,** 126, 9540-9541.

(35) Xu, X.; Muller, J. G.; Ye, Y.; Burrows, C. J. DNA-protein cross-links between guanine and lysine depend on the mechanism of oxidation for formation of C5 vs C8 guanosine adducts. *J. Am. Chem. Soc* **2008,** 130, 703-709.

(36) Pfeifer, G. P.; Besaratinia, *Hum Genet* **2009**, *125*, 493-506.

(37) David, S. S.; O'Shea, V. L.; Kundu, S. *Nature* **2007**, *447*, 941-950.

(38) Mitchell, N.; Howorka, S. *Angew. Chem. Int. Ed*. **2008**, *47*, 5565-5568.

(39) Borsenberger, V.; Mitchell, N.; Howorka, S. *J. Am. Chem. Soc.* **2009**, *131*, 7530-7531.